学 位 論 文

Multipoint Molecular Recognition through

Non-Werner Type Coordination Bonding by Ag(I)-Macrocycles

(Ag(I)大環状化合物による非ウェルナー型配位結合を用いた多点分子認識)

平成 27 年 12 月博士 (理学) 申請

東京大学大学院理学系研究科
化学専攻

尾 本 賢 一 郎

Abstract

Macrocycles provide nano-spaces for molecular recognition and chemical reactions depending on the size, shape, and chemical property of their cyclic skeletons. To construct functional macrocycles, it is important to precisely arrange functional groups within their inner surfaces. Herein, a dinuclear Ag(I)-macrocycle and a mononuclear Ag(I)-half-macrocycle which have anthracene-based nano-spaces functionalized with coordinatively labile sites of Ag(I) ions have been newly synthesized, and their guest binding abilities were examined in detail focusing on *non*-Werner type coordination properties of Ag(I) ions (Figure 1).

A dinuclear Ag(I)-macrocycle $[Ag_2\mathbf{L1}X_2](SbF_6)_2$ (X = Et_2O or H_2O) and its $CF_3SO_3^-$ salt formed host-guest complexes with several kinds of aromatic molecules such as *p*-xylenes, anthracene, [2.2]paracyclophane (pCp), and ferrocene ($FeCp_2$) derivatives in solution and/or in the solid state through Ag–π interactions (Figure 1a,b). Notably, the affinities of $[Ag_2\mathbf{L1}X_2](SbF_6)_2$ to anthracene, pCp, and $FeCp_2$ were particularly high as the binding constants (K_a = [Guest⊂Host]/([Guest][Host]) M^{-1}) were estimated to be as large as $K_a = 10^4$–10^9 M^{-1} in $CDCl_3$ at 300 K. Single crystal X-ray analyses of the resulting complexes revealed that the structures of these aromatic guest molecules were well fitted to form Ag–π interactions at *both* sides of Ag(I) ions on the nano-space of $[Ag_2\mathbf{L1}X_2](SbF_6)_2$. These results suggest that multipoint Ag–π interactions at the inner surface of the dinuclear Ag(I)-macrocycles work as effective driving forces to bind aromatic molecules. Moreover, electrochemical measurements revealed that the redox reactivity of an included ferrocene within $[Ag_2\mathbf{L1}X_2](SbF_6)_2$ was markedly changed due to the cationic character of the neighboring Ag(I) ions.

A mononuclear Ag(I)-half-macrocycle $[Ag\mathbf{L2}(Et_2O)]SbF_6$ can effectively bind one molecule of ruthenocene ($RuCp_2$) in CD_2Cl_2 with a binding constant $K_a > 10^4$ M^{-1} at 300 K (Figure 1c). The single crystal X-ray analysis of the resulting complex revealed the formation of a Ru–Ag type metal-to-metal dative bonding between a Lewis basic metal center of $RuCp_2$ and a Lewis acidic Ag(I) ions on $[Ag\mathbf{L2}(Et_2O)]SbF_6$. These results suggest that a Ru–Ag type metal-to-metal dative bonding works as an effective driving force for host-guest binding.

The present results suggest that metallo-macrocycles and half-macrocycles equipped with *non*-Werner type coordination centers provide novel binding motifs for host-guest complexation utilizing *non*-Werner type coordination: metal–arene interactions and metal–metal interactions as driving forces. Such metallo-hosts would provide novel functions, such as guest separation and activation, taking advantage of specific coordination properties of well-arranged *non*-Werner type coordination centers.

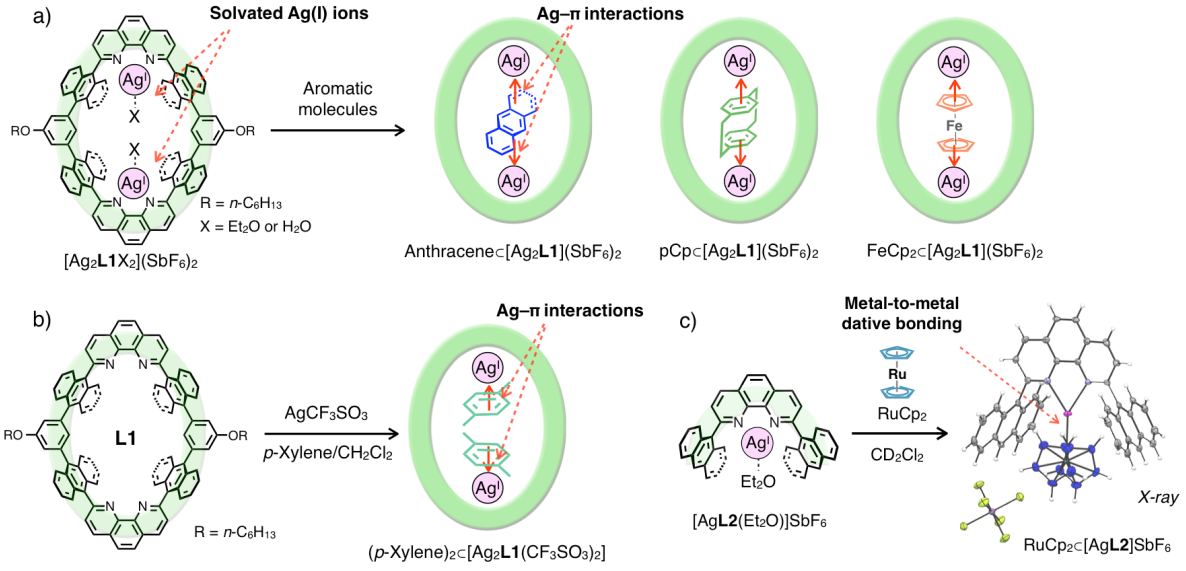

Figure 1. Host-guest complexation between a) a dinuclear Ag(I)-macrocycle $[Ag_2\mathbf{L1}X_2](SbF_6)_2$ or b) its $CF_3SO_3^-$ salt with aromatic molecules via Ag–π interactions. c) Host-guest complexation between a mononuclear Ag(I)-half-macrocycle $[Ag\mathbf{L2}(Et_2O)]SbF_6$ and ruthenocene via metal-to-metal dative bonding.

Abbreviations

A	adenine
ATP	adenosine triphosphate
ATR	attenuated total reflection
a.u.	arbitrary unit
bpy	2,2'-bipyridine
C	cytosine
Cp	cyclopentadienyl
COSY	correlation spectroscopy
DHAP	dihydroxyacetone phosphate
DMF	*N,N*-dimethylformamide
DMSO	dimethyl sulfoxide
DNA	deoxyribonucleic acid
ESI	electrospray ionization
Et_2O	diethyl ether
$FeCp_2$	ferrocene
$FeCp_2$'	hydroxymethyl ferrocene
G	guanine
GPC	gel permeation chromatography
HPLC	high performance liquid chromatography
HRMS	high resolution mass spectrometry
IR	infrared spectroscopy
J	coupling constant
M	molar
M.p.	melting point
NMR	nuclear magnetic resonance
Nu	nucleophile
ORTEP	Oak Ridge thermal-ellipsoid plot
ROE	rotating frame Overhauser effect
ROESY	rotating frame Overhauser effect spectroscopy
$RuCp_2$	ruthenocene
pCp	[2.2]paracyclophane
Sol.	solvent
T	thymine
TBA	*n*-tetrabutylammonium
THF	tetrahydrofuran
TMS	trimethylsilane
TOF	time of flight
UV-Vis	ultraviolet-visible
XRD	X-ray diffraction

Contents

Chapter 1.

General Introduction

1–1. Molecular Recognition within Biology

All of our living bodies are constructed as mixtures of various kinds of molecules. Almost all of physiological activities, such as replication, translation, transcription of genetic codes, metabolism, signalization, are conducted at the same time within highly complicated mixtures of molecules. In spite of such intricate conditions, most of chemical reactions in biological systems are conducted in highly organized manners without remarkable side reactions to establish highly sophisticated systems as lives. One of the most important mechanisms to organize such marvelous systems is *molecular recognition*[1] which means "the selective binding of a substrate by a molecular receptor to form a supramolecular species".[1b] Molecular recognition plays fundamental roles in managing our living activities such as hybridization of DNA, antibody-antigen bonding, and enzymatic reactions.[2] In these processes, receptor molecules (*hosts*) bind target substrates (*guests*) with high selectivity via multipoint and complementally intermolecular and intracomplex interactions such as coordination bonding, hydrogen bonding, hydrophobic effect, and van der Waals interaction (Figure 1–1).

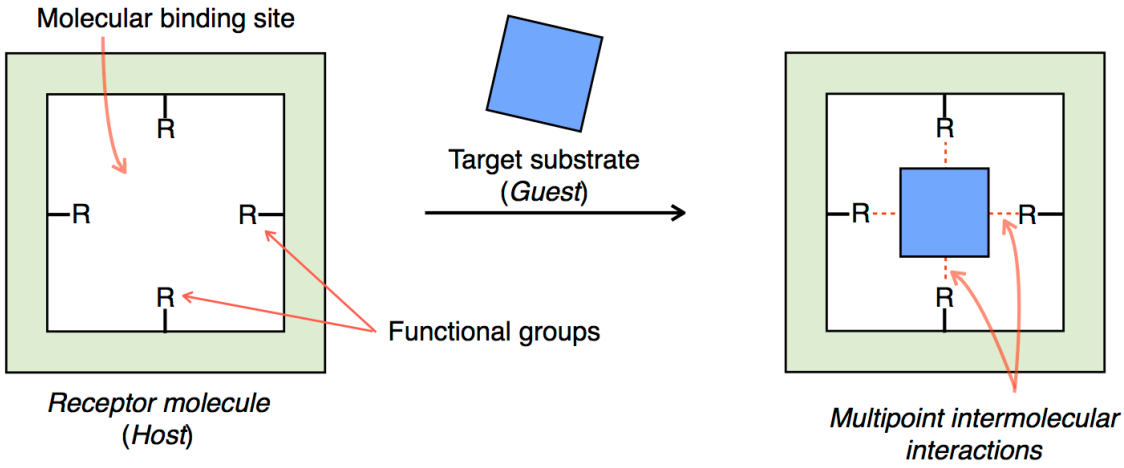

Figure 1–1. Schematic image of molecular recognition.

Molecular recognition of a target substrate usually takes place at specific positions of a receptor molecule: molecular binding sites (Figure 1–1 left).[1] In general, molecular binding sites have complement shapes and spaces to their target substrates. On the surfaces of molecular binding sites, multiple functional groups are precisely arranged in a molecular to atomic scale so as to create complementally and multipoint intermolecular interactions and contacts with target substrates. For example, in the hybridization of a DNA double helix, a DNA single strand binds its own complementally strand at its arrangement of nucleobases via multivalent intermolecular interactions such as hydrogen bonding, π–π interaction, and hydrophobic effect

(Figure 1–2a).[2] The selectivity of hybridization is precisely programmed by the sequence of nucleobases (A, C, G, and T) in a molecular to atomic scale, where A–T and C–G can create complementally hydrogen bonding, so called Watson-Crick base pairs. Vancomycin is a kind of glycopeptides which works as an antibiotic reagent (Figure 1–2b).[3] Vancomycin selectively binds to the D-alanine-D-alanine sequence of cell wall synthesis enzymes of eubacteria to inhibit its propagation. Well-defined multipoint hydrogen bonding and hydrophobic contacts between the surface of vancomycin and the D-alanine-D-alanine sequence works as a driving force for the enzyme selective binding.

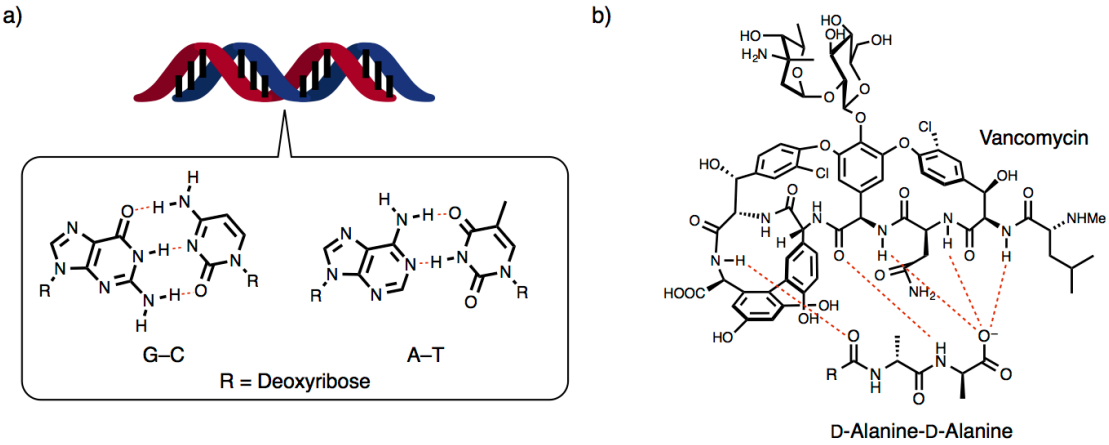

Figure 1–2. a) Hybridization of a DNA double strand and Watson-Crick base pairs, b) recognition of a D-alanine-D-alanine sequence by vancomycin.

Some receptor molecules provide confined *nano-spaces* of specific size and shape surrounded by their skeletons (Figure 1–3). Such nano-spaces often work as effective molecular binding sites, because their inner-surfaces are suitable to form multiple intermolecular interactions and contacts in *large areas* with their target substrates. Moreover, structural and chemical/physical properties of the inner surfaces can significantly affect conformations or properties of bound substrates to induce specific reactivities or properties. For instance, valinomicyn is a kind of macrocyclic transmembrane K^+ transporters, which provides a confined nano-space surrounded by a covalently linked dodecadepsipeptide skeleton with multi O-atoms (Figure 1–3a).[4] Valinomicyn can selectively include a K^+ ion within its nano-space via multipoint ion-dipole interactions at inward O-atoms. As another example, enzymes provide hydrophobic nano-pockets as active centers of catalytic reactions, which are constructed by folding of polypeptides. On their inner surfaces, multiple functional groups such as amino-acid residues and metal ions are precisely arranged.[2] Multipoint intermolecular interactions and contacts at the inner surfaces of their nano-spaces enable selective binding and activation of

target substrates. For instance, type-II aldolase, which catalyzes asymmetric aldol reactions between dihydroxyacetone phosphate (DHAP) and various aldehydes, possesses a nano-space arranged with various amino acid residues and a Zn(II) ion (Figure 1–3b).[5] In the proposed transition state, DHAP and aldehyde are bound in a specific configuration via hydrogen bonding and coordination bonding with amino acid residues and the Zn(II) ion. In this structure, Brønsted or Lewis acidic/basic characters of these functional groups activate bound substrates to enhance asymmetric aldol reactions under ambient conditions.

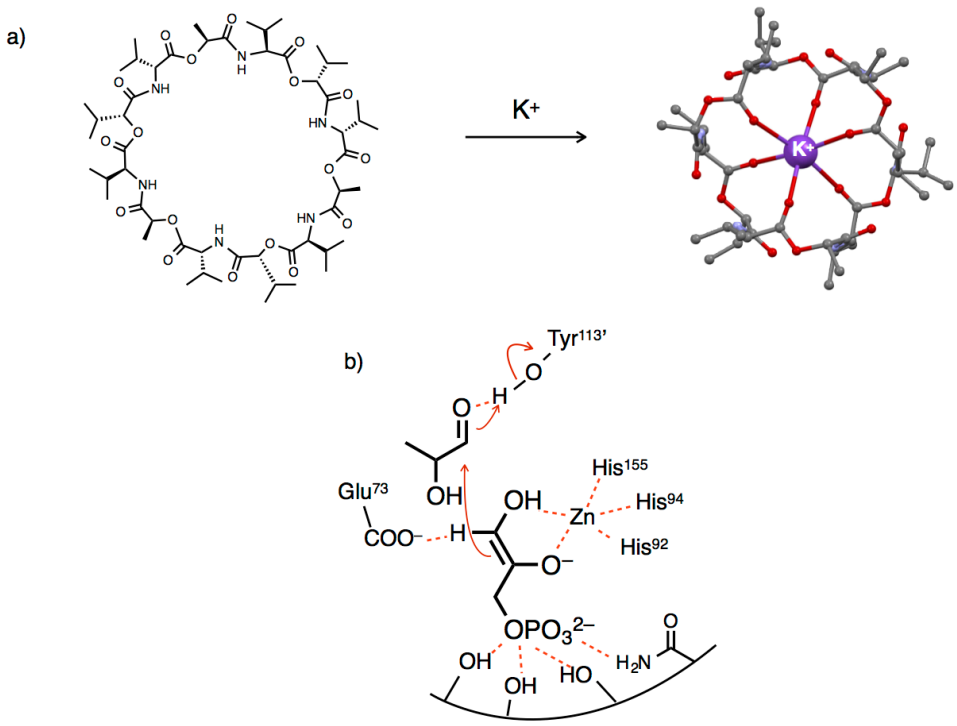

Figure 1–3. a) Recognition of K^+ by valinomycin, b) a schematic illustration of an active center of type-II aldolase.

In summary, chemical phenomena in biological systems are well organized by molecular recognition processes which utilize well designed intermolecular and intracomplex interactions and contacts between specific pairs of molecules. To realize sophisticated molecular recognition, it is important to design receptor molecules which have molecular binding sites with specific sizes, shapes and precise arrangements of multi functional groups.

1–2. Molecular Recognition by Macrocycles

As described in the previous section, to realize functional molecular recognition processes, it is very important to create host molecules with molecular binding sites which can produce multipoint intermolecular interactions with target guest molecules. In particular, host molecules possessing a confined nano-space show promise for multipoint intermolecular interactions in large areas with guest molecules.

Macrocycles such as crown ether,[6] cyclodextrin,[7] and cyclam[8] have a hollow nano-space surrounded by their covalently-linked cyclic skeleton (Figure 1–4). Within their nano-spaces, macrocycles can effectively encapsulate guest molecules of specific size and shape through multipoint intermolecular interactions and contacts at their inner surface.[1d]

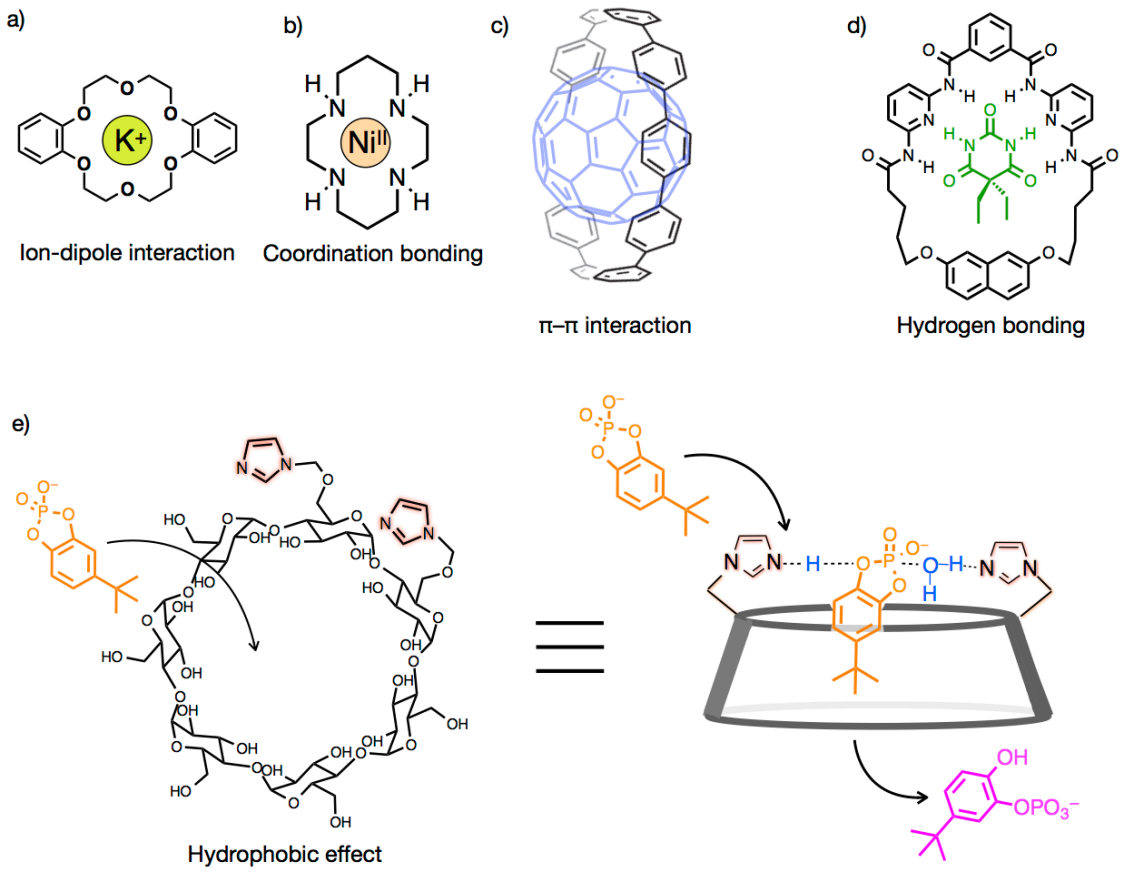

Figure 1–4. Representative examples for host-guest complexes of macrocycles and guest molecules. a) Inclusion of K^+ within dibenzo-18-crown-6 through ion-dipole interaction,[6] b) inclusion of Ni(II) within cyclam through coordination bonding,[8a] c) inclusion of C_{60} by [10]cycloparaphenylene through π–π interaction,[10] d) inclusion of barbiturate through hydrogen bonding,[11] and e) activation of hydrolysis of a cyclic phosphoester within the a hydrophobic nano-cavity of a *β*-cyclodextrin functionalized with two imidazole moieties.[12]

A variety of noncovalent interactions have been utilized as driving forces for guest binding

within macrocycles, which is an important factor to determine the type of guest molecules. *Ion-dipole interaction* and *coordination bonding* are often utilized as powerful driving forces to encapsulate metal ion(s) within a macrocycle.[9] Crown ethers are one of earlier examples of synthetic macrocycles investigated by Pedersen and co-workers (Figure 1–4a).[6] Within their cyclic poly-ether frameworks, alkali or alkaline earth metal ions such as Na^+, K^+, or Ca^{2+} can be selectively encapsulated depending on the cavity sizes of the cyclic structures through multipoint ion-dipole interactions arising from radially-inwardly projecting C–O bonds. Similarly, macrocyclic polyamines, like cyclam, can bind various kinds of transition metals within their nano-cavity normally using three to six coordination bonds between metals and N-atoms (Figure 1–4b).[8a] For the inclusion of aromatic molecules, *π–π interaction* is often used as a central driving force. [10]Cycloparaphenylene is a kind of macrocycles composed of covalently linked ten *p*-phenylene moieties (Figure 1–4c).[10] Within its nano-space surrounded by aromatic π-planes, this macrocycle accommodates a C_{60} molecule in CD_2Cl_2 by multipoint interactions with aromatic π-planes.

As an important advantage of macrocycles, they have robust and covalently-linked skeletons. Therefore, we can precisely arrange functional groups pre- or post-synthetically on their skeletons so as to control guest binding abilities and functionality. Hamilton and co-workers prepared a macrocycle shown on Figure 1–4d.[11] This macrocycle has an alternate arrangement of multiple NH and N moieties as hydrogen bonding donors and acceptors. This macrocycle can strongly bind to one molecule of barbiturate within its nano-cavity through multipoint and complementally *hydrogen bonding* with its well designed inner surface (Figure 1–4d). Cyclodextrins are kinds of macrocycles which can encapsulate many kinds of organic molecules in aqueous media due to *hydrophobic effect*.[7] To the skeleton of *β*-cyclodextrin, Breslow and co-workers post-synthetically added two imidazole moieties (Figure 1–4e).[12] Using an arranged imidazole pair as a concerted acid base catalyst center, this macrocycle catalyzed site-selective hydrolysis of a cyclic phosphoester bound within its nano-space.

In summary, macrocycles provide a confined nano-space for guest binding and activation using multiple intermolecular interactions and contacts between their inner surface and guest molecules. Furthermore, by arranging functional groups on their covalently-linked skeletons, we can design their guest binding ability and functions.

1–3. Metallo-macrocycles

As discussed in the previous section, macrocycles provide excellent nano-spaces for molecular recognition and guest activation depending on the shape, size, and chemical/physical property of their inner surfaces. To construct functional nano-spaces, it is important to precisely design arrangement styles of functional groups on their covalently-linked skeletons.

Metal ions or complexes exhibit specific properties that cannot be achieved by ordinary organic molecules, for instance, coordinating property, redox reactivity, magnetism, Lewis acidity, and electrostatic natures. Focusing on such specific properties of metal ions, various kinds of *metallo-macrocycles* which contain metal ions on their cyclic skeletons as function-centers have been investigated. In such macrocycles, guests and metal ions can interact with each other to exhibit unique guest binding behaviors or metal dependent functions as follows.

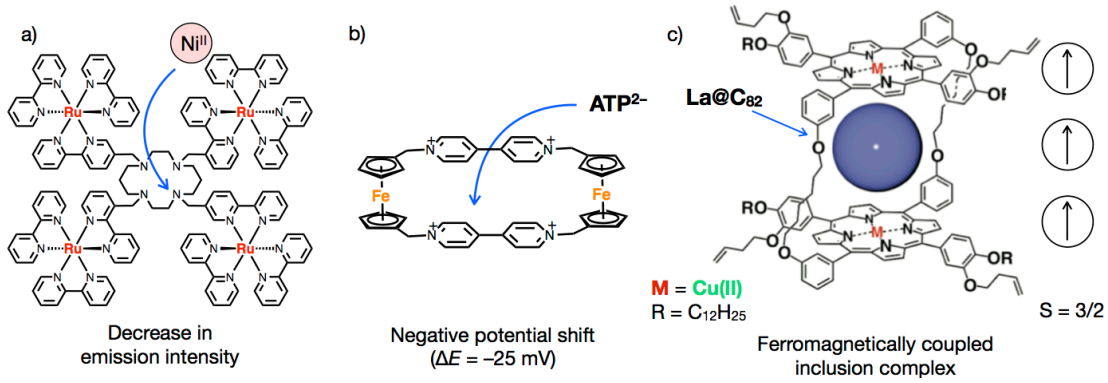

Figure 1–5. Representative examples of metallo-macrocycles which can work as sensors to detect guest molecules. a) A cyclam derivative possessing four $Ru(bpy)_3^{2+}$,[13a] b) a ferrocene-viologen based macrocycle,[14b] and c) a metallo-macrocycle with two Cu(II) porphyrin complexes.[15] Figure 1–5c is reproduced with permission from *J. Am. Chem. Soc.* **2011**, *133*, 9290–9292,[15] Copyright 2011 American Chemical Society.

Metal complexes with unique emission,[13] redox,[14] or magnetic properties[15] are often incorporated into cyclic frameworks of macrocycles (Figure 1–5). Upon host-guest complexation, properties of metal ions can be significantly affected by the neighboring guest molecules to give off modified chemical/physical properties as responses. Therefore, such macrocycles can work as sensors to detect specific guest molecules. For instance, a cyclam derivative possessing four $Ru(bpy)_3^{2+}$ chromophore centers can work as an emission sensor for metal ions (Figure 1–5a).[13a] Upon Ni(II) binding with its cyclam unit, the emission of $Ru(bpy)_3^{2+}$ centers was greatly reduced due to the heavy atom effect arising from bound metal ions. A ferrocene-viologen based macrocycle shown in Figure 1–5b works as a redox reactive

receptor for ATP^{2-}.[14b] The binding behavior of ATP^{2-} to this macrocycle can be detected from a negative shift of the ferrocene-centered redox potential because of an anionic character of the included guest. Aida and co-workers recently prepared a metallo-macrocycle with two Cu(II) porphyrin complexes on its framework, which can bind one molecule of paramagnetic La@C_{82} (Figure 1–5c).[15] The resulting host-guest complex shows a specific ferromagnetic character derived from a spin-spin coupling among two Cu(II) centers and the included guest molecule.

Metallo-macrocycles which have coordinatively labile sites of transition metal centers directing toward the inwards of their nano-spaces exhibit guest binding behaviors through direct coordination bonding between guests and metals as driving forces (Figure 1–6).[16] Such metallo-macrocycles potentially have several advantages based on specific properties of metal coordination.[17] Firstly, coordination bonding is generally stronger and has higher directionality than other non-covalent interactions. Therefore, strong host-guest interactions can be achieved using such metallo-macrocycles. Notably, the modes of metal arrangement significantly affect the affinity and binding pattern of included guests. Secondly, metal coordination can modify electronic properties of bound guests due to their cationic and Lewis acidic characters of metal centers, which have great potential to induce specific chemical reactions. Furthermore, coordination structures and metal-ligand affinity highly depend on the type and oxidation states of metal ions. Thus, the guest selectivity is possibly modified from many aspects.

Followings are excellent examples of metallo-macrocycles which utilize coordination bonding as driving forces for guest binding and/or activation (Figure 1–6). Sanders and co-workers reported a series of metallo-macrocycles which possess tetra- or trinuclear Zn(II)-porphylin scaffolds (Figure 1–6a,b).[16a,18] A tetranuclear Zn(II)-macrocycle strongly encapsulates one molecule of *meso*-tetra(pyridyl)porphyrin through multipoint coordination bonding between Zn(II) and pyridyl N-atoms as driving forces (Figure 1–6a).[16a] Furthermore, they also found that a trinuclear Zn(II)-macrocycle can accelerate a stereochemically selective Diels-Alder reaction between a pyridine-substituted diene and a dienophile (Figure 1–6b).[18] Such a specific reactivity is based on a condensation effect and controlled conformations of the substrates bound within the macrocycle through coordination bonding. Valtancoli and co-workers reported that a Zn(II)-macrocycle catalyzed ATP hydrolysis (Figure 1–6c).[19a] In this reaction, ATP is supposed to be activated by a Lewis acidic character of Zn(II) ions. Sauvage and co-workers reported that a polypyridyl-based metallo-macrocycle with a Cu(I)/(II) center can bind a 2,2'-bipyridine-based axle molecule via coordination bonding to create a pseudo-rotaxane (Figure 1–6d).[20] This pseudo-rotaxane exhibits pirouetting motions upon oxidation/reduction of the Cu(I)/(II) center based on valence-dependent coordination structures of the Cu(I)/(II) center. In 2007, Aida and co-workers reported that a metallo-macrocycles with

two Ir-porphyrins can effectively bind a C_{60} molecule in organic solvents (Figure 1–6e).[16d] The crystal structure of the resulting complex suggests C_{60} was included via multipoint η^2-type Ir–π interactions. This is one of a few examples of metallo-macrocycles which utilize *non*-Werner type coordination[21c] as a driving force for guest binding.

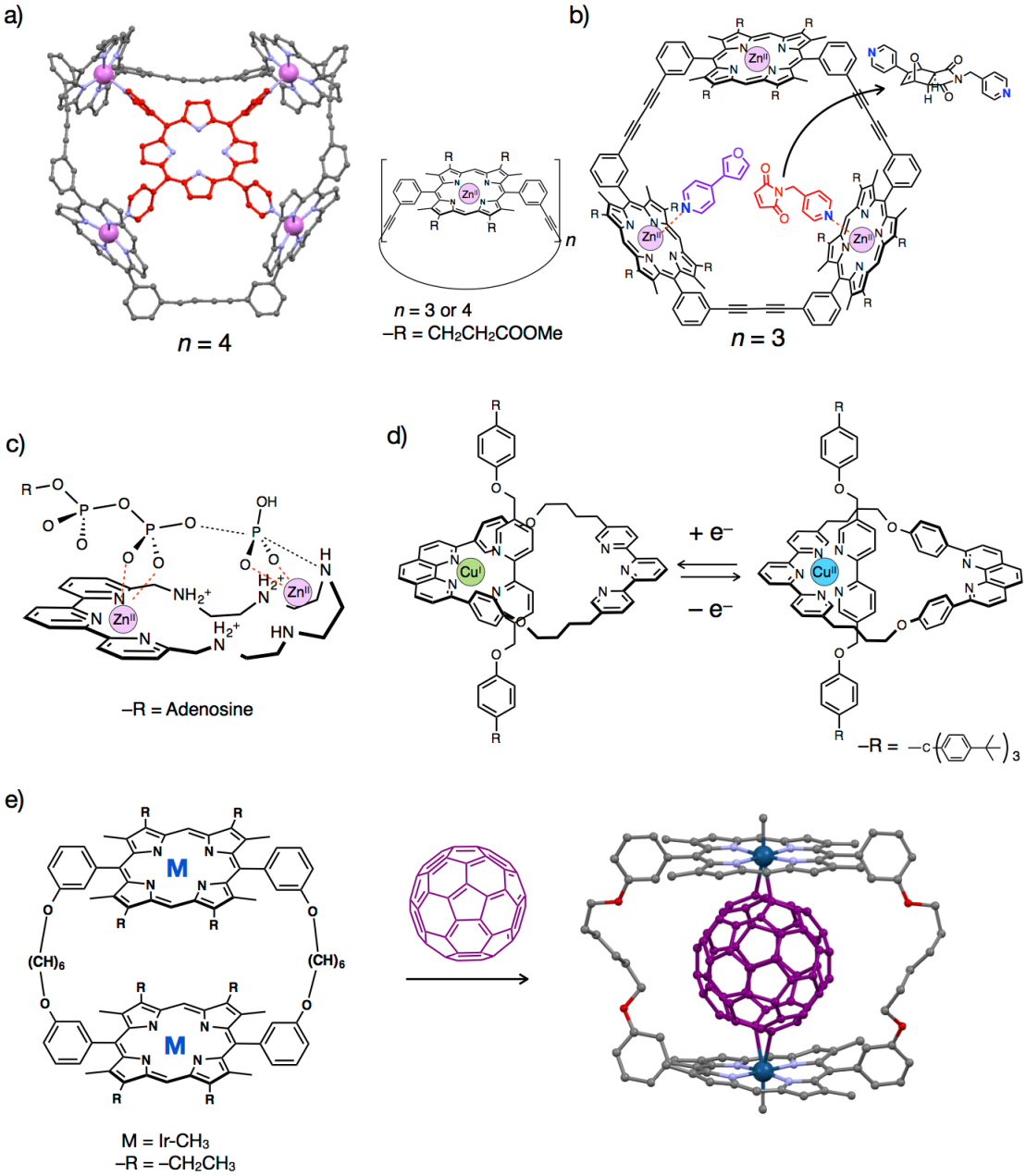

Figure 1–6. Representative examples of metallo-macrocycles which have coordinatively labile sites of metal ions on their frameworks. a) Crystal structure of the host-guest complex of *meso*-tetra(pyridyl)porphyrin and a tetranuclear Zn(II)-macrocycle,[16a] b) activation of a stereoselective Diels-Alder reaction within a trinuclear Zn(II)-macrocycle,[18] c) activation of ATP hydrolysis using a Zn(II)-macrocycle,[19a] d) pirouetting motions of a pseudo-rotaxane possessing a mononuclear Cu(I)/(II)-macrocycle,[20] and e) inclusion of C_{60} within a dinuclear Ir-porphyrin macrocycle via multipoint η^2-type Ir–π interactions.[16d]

1–4. Molecular Architectures using *Non*-Werner Type Coordination

Coordination bonding (and complexes) are generally categorized into the following two types: *Werner type coordination (complexes)* and *non-Werner type coordination (complexes)*.[21] Although there is no clear boundary between them, coordination bonding generated between metals and coordinating hetero atoms with lone-pair electrons (such as N-, O-, and halogen atoms) are usually categorized as *Werner type coordination* which is named after Alfred Werner who developed the basis of coordination chemistry (Figure 1–7a).[21d] Whereas other types of coordination bonding, such as metal–arene bonds, metal–CO bonds, or metal–metal bonds, are often categorized as *non-Werner type coordination* (Figure 1–7b).[21] As exemplified in the previous sections, Werner type coordination has been widely utilized as building blocks of metallo-supramolecular complexes or host-guest complexes, because the sites and directions of bonds are predictable.[22] Whereas *non*-Werner type coordination, in particular metal–arene interaction[23] and metal–metal interaction,[24] are also attractive, because their coordination geometry and reactivity are quite distinct from Werner type coordination. Such unique coordination properties of *non*-Werner type coordination often provide efficient methods to create novel molecular architectures.

This section describes several representative examples of molecular architectures which utilize metal–arene interactions and metal-to-metal dative bonding: 'metal-only Lewis pairs with transition metal Lewis bases'[24h] as *non*-Werner type coordination.

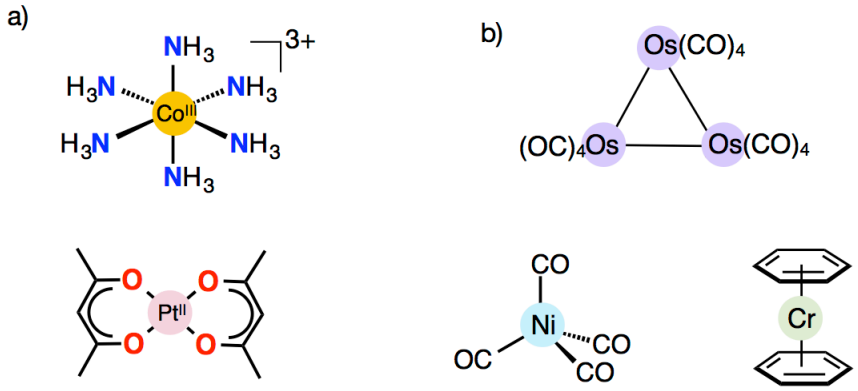

Figure 1–7. Representative examples of a) Werner type complexes and b) *non*-Werner type complexes.

1–4–1. Metal–arene interaction

Metal ions can vertically bind to the aromatic π-plane to create metal–arene complexes.[23] Some of metal–arene complexes play fundamental roles in organometallic chemistry, because they can induce specific chemical reactions to the bound aromatic rings.[23c] For instance, (arene)tricarbonylchromium derivatives, which are prepared by the reaction between aromatic

rings and $Cr(CO)_6$, represent η^6-type Cr–arene interactions (Figure 1–8a). In these complexes, electron withdrawing effects of $Cr(CO)_3$ units facilitate nucleophilic substitution reactions of the bound aromatic rings.[25]

Notably, the thermodynamic stabilities and binding modes (hapticities) of metal–arene interactions vary with the type of metals and aromatic molecules. Such diverse coordination structures make it possible to create unique molecular architectures. Murahashi and co-workers succeeded in preparing a series of multinuclear Pd-complexes taking advantages of vast π-surfaces of polycyclic aromatic hydrocarbons as templates (Figure 1–8b).[26] Metal–arene interactions are sometimes utilized to create specific supramolecular structures. Ag(I) ions are well known to weakly bind to the peripheries of neutral aromatic hydrocarbons via Ag–π interactions in usually η^1 to η^2 manners.[27] Taking advantage of Ag–π interactions as linkers, various kinds of coordination polymers have been reported by Amma and Munakata, some of which possess specific multilayer structures (Figure 1–8c).[27a,c] Notably, Ag–π interaction is a weak interaction,[27e] therefore studies in solution have been mainly limited to the systems which utilize Ag–π interactions in multipoint manners.[28] For instance, [2.2.2]paracyclophane which possess a macrocyclic structure with three aromatic rings can strongly bind Ag(I) ions in chloroform through multipoint Ag–π interactions (Figure 1–8d).[28a]

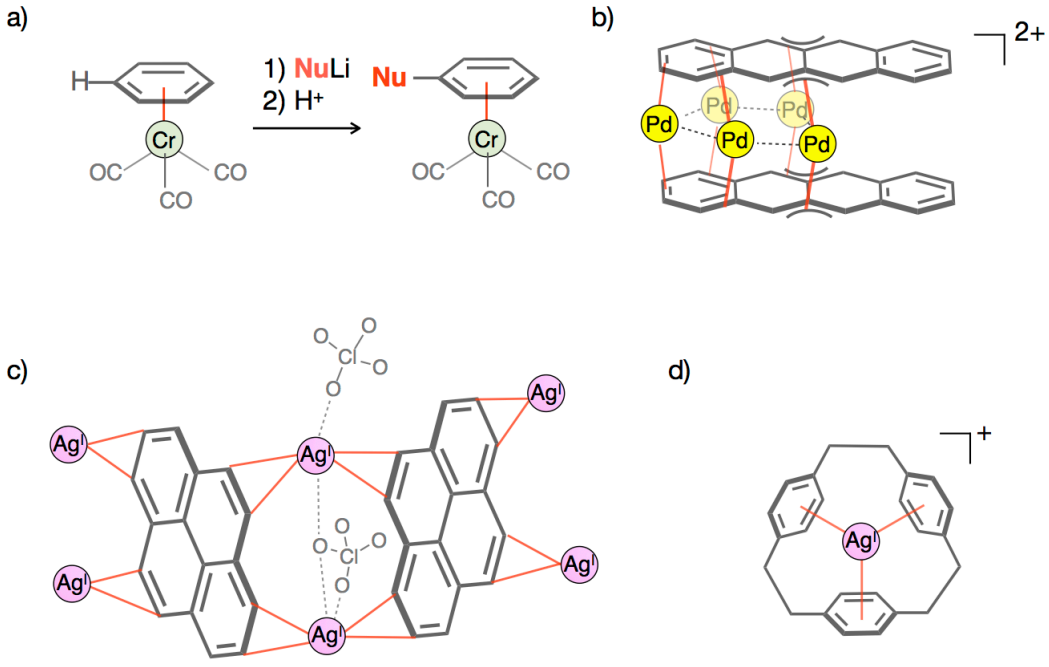

Figure 1–8. Representative examples of metal–arene complexes. a) A nucleophilic substitution reaction of a (arene)tricarbonylchromium derivative (Nu: nucleophile),[23c,25] b) a multinuclear Pd-complex using tetracenes as templates,[26] c) a multilayer coordination polymer composed of Ag(I) ions and pyrenes through Ag–π interactions,[27c] and d) a Ag(I)-complex of [2.2.2]paracyclophane.[28a]

1–4–2. Metal-to-metal dative bonding

Metal–metal bonding is an attractive interaction which enables to create electronically-coupled supramolecules with specific structural characteristics.[24] In particular, metal assembled complexes composed of closed-shell group 11 metals (Cu(I), Ag(I), and Au(I)) and planar Pt(II) complexes have been widely investigated because of their specific emission and absorption properties.[24a-f,i,j] In these cases, each metal ion shares electrons more or less equally to form metal–metal bonding, which is often called covalent bonding or non-dative bonding.[24c,h] While there is another category of metal–metal interactions: metal-to-metal dative bonding, in which one metal ions work as Lewis base to provide electrons to the other Lewis acidic metal center.[24c,g,h] The distinction between these two categories of metal–metal bonding is not always clear-cut and often considered empirically. However, in the cases of latter, proper choices of Lewis acidic and basic metals possibly provide strategies to design metal assembled architectures with alternative arrangements of hetero metals.[24c,g,h] For instance, an electron rich Pt(II) center containing a cyclo-metalated ligand can work as an electron donor to create Pt(II)→Ag(I) dative bonding.[24g,h] Taking its advantage, Ito and co-workers succeeded to prepare a metal assembled complex with an alternative linear arrangement of multinuclear Pt(II) and Ag(I) ions in the crystalline state (Figure 1–9a).[29] Also, transition metal centers of group 8 metallocenes are known to act as Lewis bases due to the donation property of occupied e_{2g} orbital.[30,31] Based on such Lewis basic characteristics of these metal centers, ruthenocene, osmocene, and ferroceneophane derivatives which have sterically accessible metal centers can bind to Lewis acidic metal ions such as Hg(II) and Sn(IV) via metal-to-metal dative bonding to create multinuclear metal complexes (Figure 1–9b).[31] Moreover, some of metal-to-metal bonded complexes show unique reactivity based on cooperative effects of multi metal centers.[32] For instance, hetero dinuclear M→M' complexes (M = Fe(0), Ru(0); M' = Cu(I), Ag(I)) activate the cleavage of H_2 molecule to catalyze semi-hydrogenation of alkynes (Figure 1–9c,d).[32c]

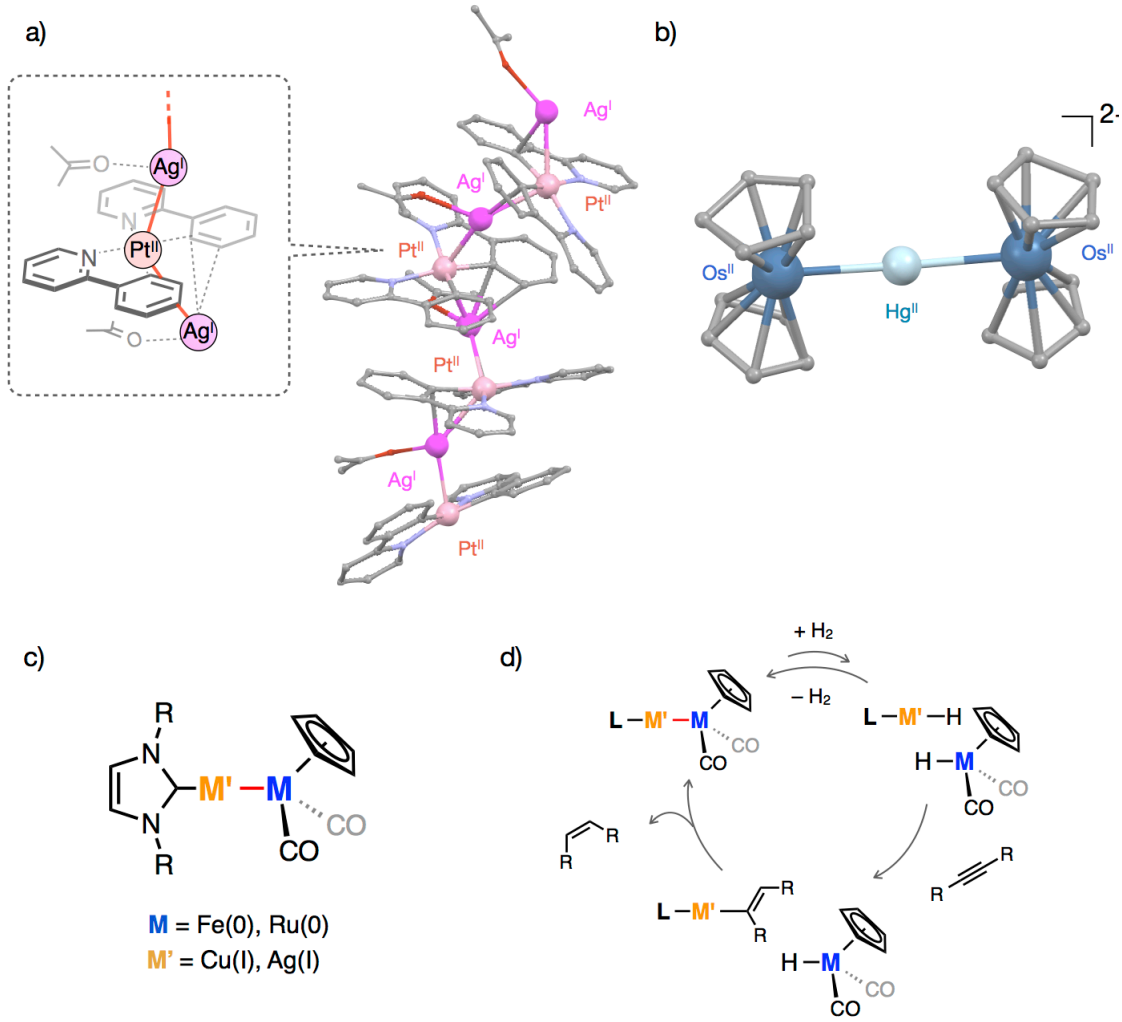

Figure 1–9. Representative examples of heteronuclear complexes through metal-to-metal dative bonding. a) A crystal structure of a metal assembled complex with an alternative linear arrangement of Pt(II) and Ag(I) ions,[29] b) a crystal structure of a reported Hg(II)-complex of osmocene,[31a] c) molecular structures of hetero dinuclear M→M' complexes (M = Fe(0), Ru(0); M' = Cu(I), Ag(I)) which catalyze semi-hydrogenation of alkynes, and d) hypothetical mechanism for the catalytic reactions.[32c]

1–5. The Aim of This Research

As shown in sections 1–2 and 1–3, nano-spaces of macrocycles exhibit special functionalities for guest binding and activation. In order to control guests binding and activation abilities, it is significantly important to design functional groups in terms of shape, size, and mode of arrangement on the inner surface of macrocycles. Metal coordination is one of the powerful tools to bind guest molecules and develop further functionalities. However, in the cases of conventional metallo-macrocycles, utilization of metal coordination is limited to Werner type coordination. Metallo-macrocycles, which utilize *non*-Werner type coordination, such as matal–arene and metal–metal interactions for space-functions, have not been extensively investigated so far, except a few examples,[16d] in spite of their attractive coordination structures and reactivities quite distinct from classical Werner type coordination.

In this research, I aim to develop metallo-macrocycles possessing a *non*-Werner type coordination center as a functional platform with a view to developing host-guest systems based on *non*-Werner type coordination (Figure 1–10). Nano-spaces arranged with coordinatively labile sites of *non*-Werner type coordination centers provide novel platforms for host-guest complexiation with unique structures, selectivity, and properties. For instance, binding and activation of guest molecules without coordinating hetero-atoms would be achieved. Furthermore, specific chemical properties of *non*-Werner type coordination centers would affect structures, reactivities, and properties of guest molecules included within nano-spaces.

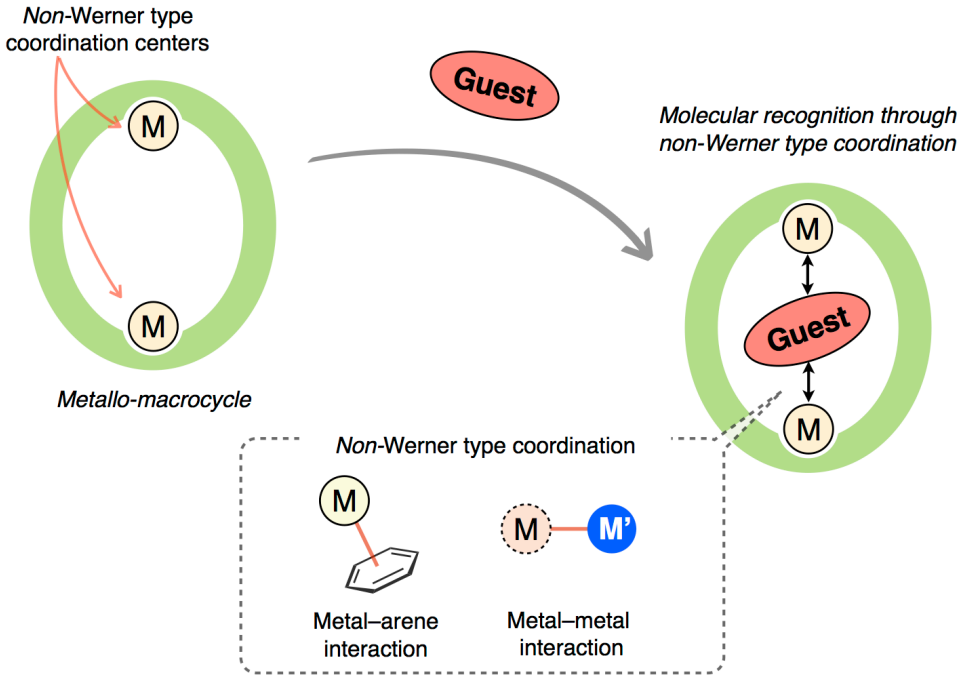

Figure 1–10. The concept of this study: molecular recognition through *non*-Werner type coordination within a nano-space of a metallo-macrocycle.

In this work, a dinuclear Ag(I)-macrocycle $[Ag_2\mathbf{L1}X_2](SbF_6)_2$ (X = Et_2O or H_2O) and a mono-nuclear Ag(I)-half-macrocycle $[Ag\mathbf{L2}(Et_2O)]SbF_6$ were designed and synthesized, which have anthracene-based nano-spaces arranged with coordinatively labile sites of Ag(I) ions as *non*-Werner type coordination centers (Figure 1–11). Moreover, their guest binding ability was examined in detail focusing on the *non*-Werner type coordination behaviors of Ag(I) ions: Ag–π interaction and metal-to-metal dative bonding.

Chapter 2 describes host-guest complexation behaviors between a dinuclear Ag(I)-macrocycles and pristine aromatic molecules using multipoint Ag–π interactions as driving forces. Chapter 3 describes host-guest complexation behaviors between a mononuclear Ag(I)-half-macrocycle and ruthenocene as a pristine organometallic molecule using Ru–Ag type metal-to-metal dative bonding.

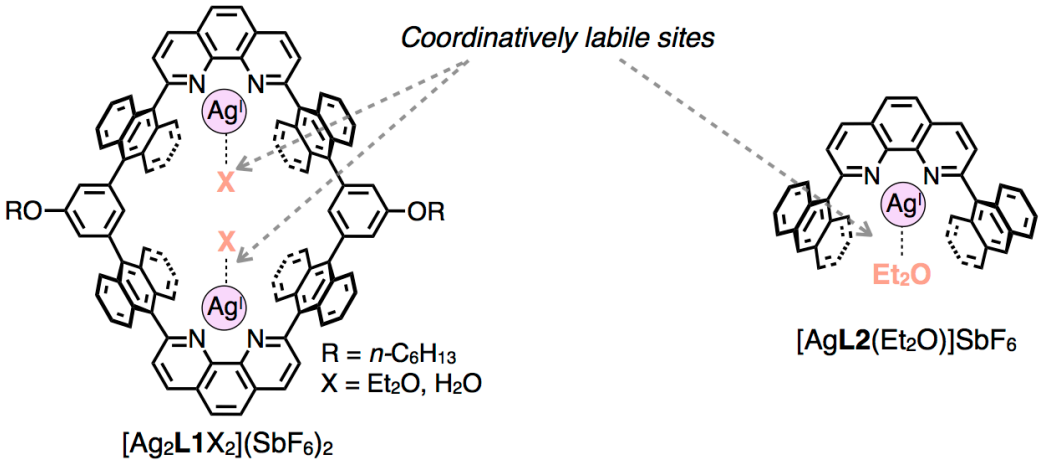

Figure 1–11. Molecular structures of a dinuclear Ag(I)-macrocycle and a mono-nuclear Ag(I)-half-macrocycle.

1–6. References

[1] a) Lehn, J.-M. *Angew. Chem. Int. Ed. Engl.* **1988**, *27*, 89–112. b) Lehn, J.-M. *Angew. Chem. Int. Ed. Engl.* **1990**, *29*, 1304–1319. c) Ariga, K.; Ito, H.; Hill, J. P.; Tsukube, H. *Chem. Soc. Rev.* **2012**, *41*, 5800–5835. d) *Supramolecular Chemistry, 2nd Edition*; Steed, J. W., Atwood, J. L., Eds.; WILEY, 2009.

[2] 入間達郎; 岡山博人; 清水高尾 訳, 「ストライヤー生化学　第５版」 東京化学同人, 2004.

[3] Knox. J.; Pratt, R. F. *Anti. Agents. Chem.* **1990**, *34*, 1343–1347.

[4] Neupert-Laves, K.; Dobler, M. *Helv. Chim. Acta* **1975**, *58*, 432–442.

[5] Machajewski, T. D.; Wong, C.-H. *Angew. Chem. Int. Ed.* **2000**, *39*, 1352–1374.

[6] Pedersen, C. J. *Angew. Chem. Int. Ed. Engl.* **1988**, *27*, 1021–1027.

[7] Breslow, R.; Dong, S. D. *Chem. Rev.* **1998**, *98*, 1997–2011.

[8] a) Barefield, E. K.; Mocella, M. T. *J. Am. Chem. Soc.* **1975**, *97*, 4238–4246. b) Kimura, E. *Tetrahedron* **1992**, *48*, 6175–6217. c) Wainwright, K. P. *Coord. Chem. Rev.* **1997**, *166*, 35–90.

[9] Christensen, J. J.; Eatough, D. J.; Izatt, R. *Chem. Rev.* **1974**, *74*, 351–384.

[10] Iwamoto, T.; Watanabe, Y.; Sadagiro, T.; Haino, T.; Yamago, S. *Angew. Chem. Int. Ed.* **2011**, *50*, 8342–8344.

[11] Chang, S.-K.; Engen, D. V.; Fan, E.; Hamilton, A. D. *J. Am. Chem. Soc.* **1991**, *113*, 7640–7645.

[12] Breslow, R. *Acc. Chem. Res.* **1995**, *28*, 146–153.

[13] a) Josceanu, A. M.; Moore, P.; Rawle, S. C.; Sheldon, P.; Smith, S. M. *Inorg. Chim. Acta* **1995**, *240*, 159–168. b) Keefe, M. H.; Benkstein, K. D.; Hupp, J. T. *Coord. Chem. Rev.* **2000**, *205*, 201–228.

[14] a) Beer, P. D.; Gale, P. A.; Chen, G. Z. *J. Chem. Soc., Dalton Trans.* **1999**, 1897–1909. b) Reynes, O.; Bucher, C.; Moutet, J.-C.; Royal, G.; Saint-Aman, E. *Chem. Commun.* **2004**, *40*, 428–429.

[15] Hajjaj, F.; Tashiro, K.; Nikawa, H.; Mizorogi, N.; Akasaka, T.; Nagase, S.; Furukawa, K.; Kato, T.; Aida, T. *J. Am. Chem. Soc.* **2011**, *133*, 9290–9292.

[16] a) Anderson, S.; Anderson, H. L.; Bashall, A.; McPartlin, M.; Sanders, J. K. M. *Angew. Chem. Int. Ed*. **1995**, *34*, 1096–1099. b) Amendola, V.; Fabbrizzi, L.; Mangano, C.; Pallavicini, P.; Poggi, A.; Taglietti, A. *Coord. Chem. Rev*. **2001**, *219–221*, 821–837. c) Fabbrizzi, L.; Foti, F.; Patroni, S.; Pallavicini, P.; Taglietti, A. *Angew. Chem. Int. Ed.* **2004**, *43*, 5073–5077. d) Yanagisawa, M.; Tashiro, K.; Yamasaki, M.; Aida, T. *J. Am. Chem. Soc.* **2007**, *129*, 11912–11913. e) Devoille, A. M. J.; Richardson, P.; Bill, N. L.; Sessler, J. L.; Love, J. B. *Inorg. Chem.* **2011**, *50*, 3116–3126.

[17] 藤田誠; 塩谷光彦 編, 「超分子金属錯体」三共出版株式会社, 2009.

[18] Clyde-Watson, Z.; Vidal–Ferran, A.; Twyman, L. J.; Walter, C. J.; McCallien, D. W. J.; Fanni, S.; Bampos, N.; Wylie, R. S.; Sanders, J. K. M. *New J. Chem.* **1998**, *22*, 493–502.

[19] a) Bazzicalupi, C.; Bencini, A.; Bianchi, A.; Danesi, A.; Giorgi, C.; Lodeiro, C.; Pina, F.; Santarelli, S.; Valtancoli, B. *Chem. Commun.* **2005**, 2630–2632. b) Bencini, A.; Lippolis, V.; Valtancoli, B. *Inorg.*

Chim. Acta **2014**, *417*, 38–58.

[20] Poleschak, I.; Kern, J.-M.; Sauvage, J.-P. *Chem. Commun.* **2004**, 474–476.

[21] a) 山本明夫 著, 「有機金属化学－基礎と応用－」裳華房, 1982. b) 渡部正利; 矢野重信; 碇谷隆雄 著, 「錯体化学の基礎－ウェルナー錯体と有機金属錯体－」講談社, 1995. c) 基礎錯体工学研究会 編, 「新版 錯体化学 基礎と最新の展開」講談社, 2006. d) Werner, H. *Angew. Chem. Int. Ed.* **2013**, *52*, 6146–6153.

[22] a) Chakrabarty, R.; Mukherjoo, P. S.; Stang, P. J. *Chem. Rev.* **2011**, *111*, 6810–6918. b) Nakamura, T.; Ube, H.; Shionoya, M. *Chem. Lett.* **2013**, *42*, 328–334.

[23] a) Muetterties, E. L.; Bleeke, J. R.; Wucherer, E. J. *Chem. Rev.* **1982**, *82*, 499–525. b) Fagan, P. J.; Ward, M. D.; Calabrese, J. C. *J. Am. Chem. Soc.* **1989**, *111*, 1698–1719. c) *Modern Arene Chemistry*; Astruc, D., Eds.; WILEY-VCH Verlag GmbH & Co. KGaA: Weinheim, 2002.

[24] a) Krogmann, K. *Angew. Chem. Int. Ed.* **1969**, *8*, 35–42. b) Pyykkö, P. *Chem. Rev.* **1997**, *97*, 597–636. c) Ito, T.; Kajiwara, T.; in *Metal Assembled Complexes*; Okawa, H.; Ito T. Eds.; Kagaku Dojin, Kyoto, **2003**, p.3–10 (Japanese). d) 佐々木陽一; 石谷治 編, 「金属錯体の光化学」三共出版株式会社, 2007. e) Katz, M. J.; Sakai, K.; Leznoff, D. B. *Chem. Soc. Rev.* **2008**, *37*, 1884–1895. f) Sculfort, S.; Braunstein, P. *Chem. Soc. Rev.* **2011**, *40*, 2741–2760. g) Díez, Á.; Lalinde, E.; Moreno, M. T. *Coord. Chem. Rev.* **2011**, *255*, 2426–2447. h) Bauer, J.; Braunschweig, H.; Dewhurst, R. D. *Chem. Rev.* **2012**, *112*, 4329–4346. i) Krogman, J. P.; Thomas, C. M. *Chem. Commun*. **2014**, *50*, 5115–5127. j) Schmidbaur, H.; Schier, A. *Angew. Chem. Int. Ed.* **2015**, *54*, 746–784.

[25] Brown, D. A.; Raju, J. R. *J. Chem. Soc. A* **1966**, 40–43.

[26] Murahashi, T.; Fujimoto, M.; Oka, M.; Hashimoto, Y.; Umemura, T.; Tatsumi, Y.; Nakao, Y.; Ikeda, A.; Sasaki, S. Kurosawa, H. *Science* **2006**, *313*, 1104–1107.

[27] a) Griffith, E. A. H.; Amma, E. L. *J. Am. Chem. Soc.* **1974**, *96*, 5407–5413. b) Dias, H. V. R.; Wang, Z.; Jin, W. *Inorg. Chem.* **1997**, *36*, 6205–6215. c) Munakata, M.; Wu, L. P.; Ning, G. L. *Coord. Chem. Rev.* **2000**, *198*, 171–203. d) Lindeman, S. V.; Rathore, R.; Kochi, J. K. *Inorg. Chem.* **2000**, *39*, 5707–5716. e) Maier, J. M.; Jungwun Hwang, P. L.; Smith, M. D.; Shimizu, K. D. *J. Am. Chem. Soc.* **2015**, *137*, 8014–8017.

[28] a) Pierre, J.-L.; Baret, P.; Chautemps, P.; Armand, M. *J. Am. Chem. Soc.* **1981**, *103*, 2986–1988. b) Ikeda, M.; Takeuchi, M.; Shinkai, S. Tani, F.; Naruta, Y.; Sakamoto, S.; Yamaguchi, K. *Chem. Eur. J.* **2002**, *8*, 5542–5550.

[29] Yamaguchi, T.; Yamazaki, F.; Ito, T. *J. Am. Chem. Soc.* **2001**, *123*, 743–744.

[30] Green, J. C. *Chem. Soc. Rev.* **1998**, *27*, 263–271.

[31] a) Watanabe, M.; Sano, H. *Bull. Chem. Soc. Jpn.* **1990**, *63*, 1455–1461. b) Watanabe, M.; Nagasawa, A.; Sato, M.; Motoyama, I.; Takayama, T. *Bull. Chem. Soc. Jpn.* **1998**, *71*, 1071–1079. c) Enders, M.; Kohl, G.; Pritzkow, H. *Organometallics* **2002**, *21*, 1111–1117. d) Gramigna, K. M.; Oria, J. V.; Mandell,

C. L.; Tiedemann, M. A.; Dougherty, W. G.; Piro, N. A.; Kassel, W. S.; Chan, B. C.; Diaconescu, P. L.; Nataro, C. *Organometallics* **2013**, *32*, 5966−5979.

[32] a) Jayarathne, U.; Mazzacano, T. J.; Bagherzadeh. S.; Mankad, N. P. *Organimetallics* **2013**, *32*, 3986–3992. b) Mazzacano, T. J.; Mankad, N. P. *J. Am. Chem. Soc.* **2013**, *135*, 17258–17261. c) Karunananda, M. K.; Mankad, N. P. *J. Am. Chem. Soc.* **2015**, *137*, 14598–14601.

Chapter 2.

Inclusion of Aromatic Guest Molecules within a Dinuclear Ag(I)-Macrocycle via Multipoint Ag–π Interactions

2–1. Introduction

Aromatic molecules have attracted attention from many researchers because of their simple but rigid planar structures, electronic properties, reactivity, and supramolecular behaviors.[1] They are also considered as attractive host molecules in the field of host-guest chemistry, because host molecules provide nano-spaces to recognize, isolate, and control chemical or physical properties of included aromatic molecules.[2] As the stabilities and properties of the resulting host-guest complexes are significantly affected by close and multipoint interactions or contacts between host and aromatic guest molecules, investigation of binding modes and motifs of aromatic molecules is one of the most important issues particularly in the field of supramolecular chemistry. For the inclusion of aromatic molecules, hydrophobic effect is often used in aqueous media. For instance, Gibb and Ramamurthy reported that extended cavitand can include two molecules of aromatic hydrocarbon at the same time in water (Figure 2–1a).[2a,b] In these cases, included aromatic guests exhibit specific excimer emission or a stereo-selective photo-dimerization reaction due to the condensation effect and pre-organization of the aromatic molecules within the nano-space. π–π interaction or electrostatic interaction are also utilized as driving forces to include aromatic molecules. Wrüthner recently reported that a perylene bisimide cyclophane possessing a nano-space with electron deficient π-planes can effectively bind various kinds of aromatic hydrocarbons in organic solvent using multiple π–π interactions (Figure 2–1b).[2d] In this case, the stability constants of the complexation tend to increase as the face-to-face π–π overlaps between host and guest become larger. Moreover, this cyclophane works as a fluorescent probe to detect aromatic guest molecules based on specific emission properties depending on the electron transfer between guests and electron deficient π-planes of the host. A cationic macrocycle by Stoddart can also bind to various kinds of polycyclic aromatic hydrocarbons using π–π interaction and electrostatic interaction, which has a potential to extract polycyclic aromatic hydrocarbons from crude oil from Saudi Arabia (Figure 2–1c).[2c]

As an important category of host molecules, metallo-macrocycles have been widely studied to create functional host-guest complexes due to specific chemical and physical properties of metal ions which depend on the type, number and mode of arrangement of metal ions on their skeletons.[3] In particular, metallo-macrocycles that possess coordinatively labile sites of metal ions on their inner surfaces can utilize coordination bonding as powerful driving forces for guest binding and activation. As mentioned in the previous chapter, several metal ions can bind to the aromatic π-planes through metal–arene interactions, which has developed specific molecular architectures or chemical reactions involving aromatic molecules.[4,5] Herein, I envisioned that metallo-macrocycles with proper arrangement of coordinaively labile sites of multiple metal

ions would provide novel and effective binding motifs to recognize and activate aromatic guest molecules of suitable sizes and shapes utilizing multiple metal–arene interactions as driving forces (Figure 2–2). Such host-guest complexes mediated by multipoint metal–arene interactions are expected to exhibit specific physical or chemical properties to included aromatic guest molecules based on metal coordination.

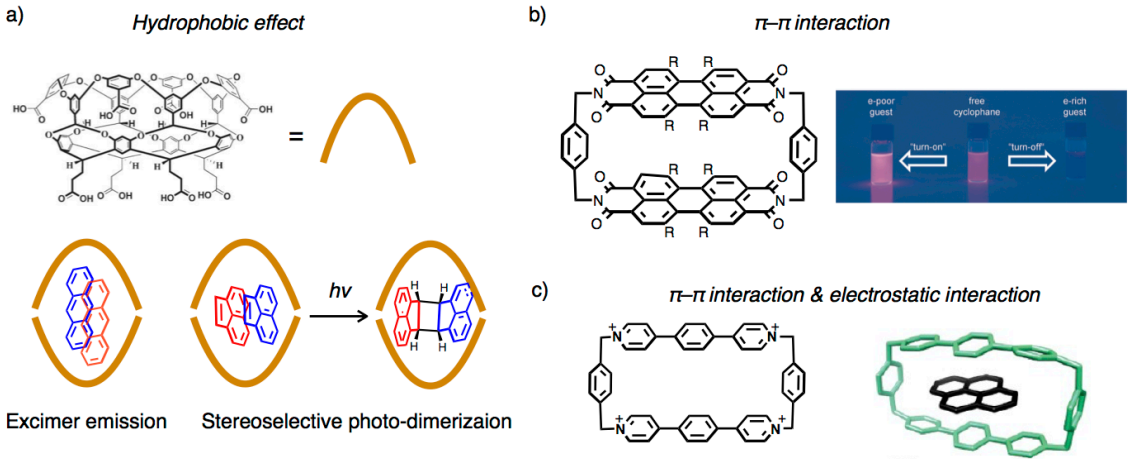

Figure 2–1. Representative examples of the inclusion complexes of aromatic guest molecules. a) Inclusion of two anthracenes and acenaphthylenes within an extended cavitand and their specific photo-chemical properties.[2a,b] b) The molecular structure of a perylene bisimide cyclophane and its specific emission properties upon guest binding.[2d] c) The molecular structure of a cationic macrocycle and its inclusion complex of pyrene.[2c] Figures 2–1a–c are reproduced with permission from *Chem. Commun.* **2007**, 1062–1064,[2b] Copyright 2007 The Royal Society of Chemistry, *Angew. Chem. Int. Ed.* **2015**, *54*, 10165–10168,[2d] Copyright 2015 Wiely-VCH Verlag GmbH, Weinheim, and from *J. Am. Chem. Soc.* **2013**, *135*, 183–192,[2c] Copyright 2013 American Chemical Society, respectively.

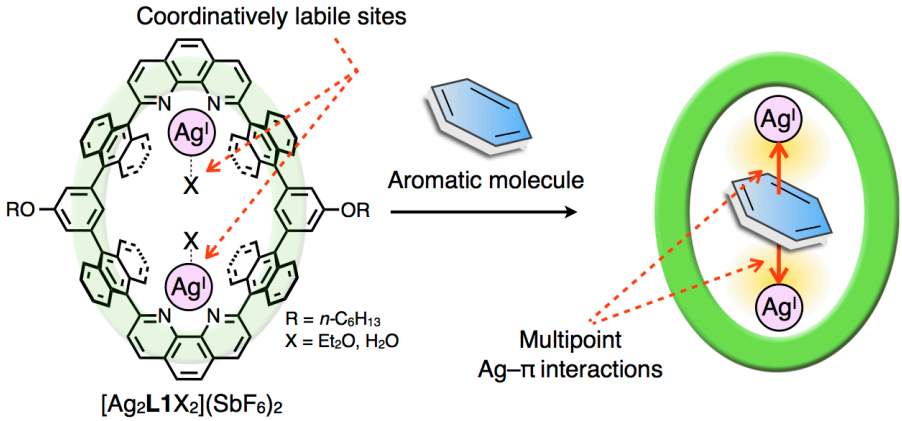

Figure 2–2. A schematic drawing of the inclusion of aromatic molecules via multipoint Ag–π interactions within a nano-space of a dinuclear Ag(I)-macrocycle $[Ag_2\mathbf{L1}X_2](SbF_6)_2$.

In this chapter, I describe the synthesis and guest binding behaviors of a dinuclear Ag(I)-macrocycle $[Ag_2\mathbf{L1}X_2](SbF_6)_2$ (X = Et_2O or H_2O) (Figure 2–2). This complex possesses a well-defined nano-space equipped with coordinatively labile sites of two Ag(I) ions on its inner

surface. Herein, I revealed that $[Ag_2\mathbf{L1}X_2](SbF_6)_2$ provides a novel and effective motif to bind aromatic guest molecules utilizing multipoint Ag–π interactions as driving force.[5] Furthermore, I found that the cationic character of Ag(I) ions can modify the redox potentials of included aromatic molecules.

2–2. Design and Synthesis of a Dinuclear Ag(I)-Macrocycle

A cyclophane-type macrocyclic ligand **L1** was newly designed as a platform of a metallo-macrocycle with a rigid and well-defined aromatic framework (Figure 2–3). Two phenanthrolines, placed in about 1 Å apart from each other, can work as bidentate metal binding sites to immobilize two metal ions on the inner surface of the nano-space in a certain distance.[6] Four anthracenes placed as main building brocks are supposed to stand orthogonal to the cyclic framework of **L1** due to the steric repulsion among H-atoms of the neighboring aromatic skeletons to provide a three dimensional thick cavity.[7]

Ag(I) ion was selected here, because Ag(I) ion is well known to bind to the periphery of various types of aromatic π-planes through Ag–π interactions.[5] Besides, the coordinatively labile character of Ag(I) ion would provide an effective platform as a guest binding site to create thermodynamically stable host-guest assemblies.[8]

Due to the above-mentioned characteristics, **L1** can provide a well defined three dimensional nano-space with a precise arrangement of coordinatively labile sites of Ag(I) ions upon metal complexation. This would work as an effective binding site for aromatic molecules through multipoint Ag–π interactions.

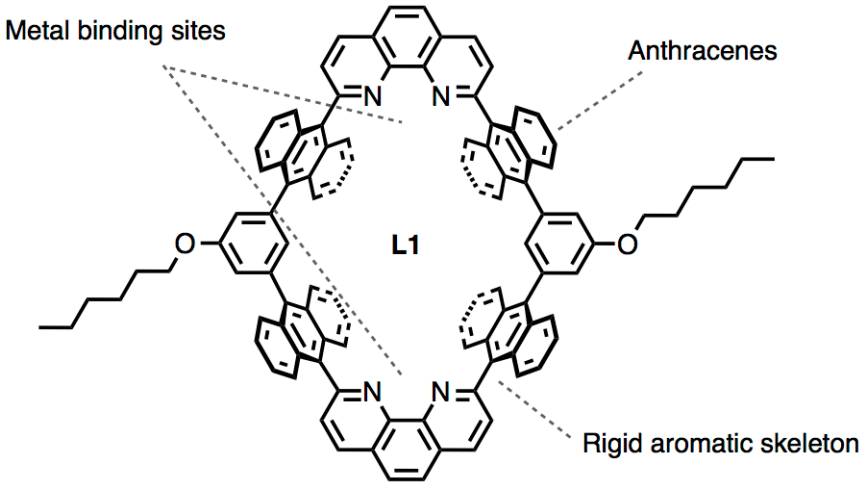

Figure 2–3. Molecular design of macrocyclic ligand **L1**.

The macrocyclic ligand **L1** was prepared by sequentially connecting aromatic fragments by Pd-catalyzed coupling reactions (Scheme 2–1). 9,10-Bis(4,4,5,5-tetramethyl-1,3,2-dioxaborolan-2-yl)anthracene (**3**), 2,9-dichrolo-1,10-phenanthroline (**4**), and 1,3-dibromo-5-(hexyloxy)benzene (**5**) were connected to afford V-shaped precursors **6** and **7**. The final cyclization reaction between **6** and **7** afforded **L1** in 5% yield. Although, **L1** was hardly soluble in common organic solvents (acetone,

n-hexane, benzene etc), it can be dissolved in $CHCl_3$ at a concentration about 100 μM. **L1** was characterized by NMR (^1H, COSY, and ROESY), HRMS (ESI), and the following crystal structures of its derivatives (Figure 2–4–5, 2–7–8). The UV-Vis spectrum of **L1** in $CHCl_3$ showed an absorption band around 350–450 nm, which is typical to π-π* transition of anthracene moieties (Figure 2–6).[7b] Emission spectrum of **L1** showed broad band around 470 nm in $CHCl_3$.

Scheme 2–1. Synthesis of macrocyclic ligand **L1**.

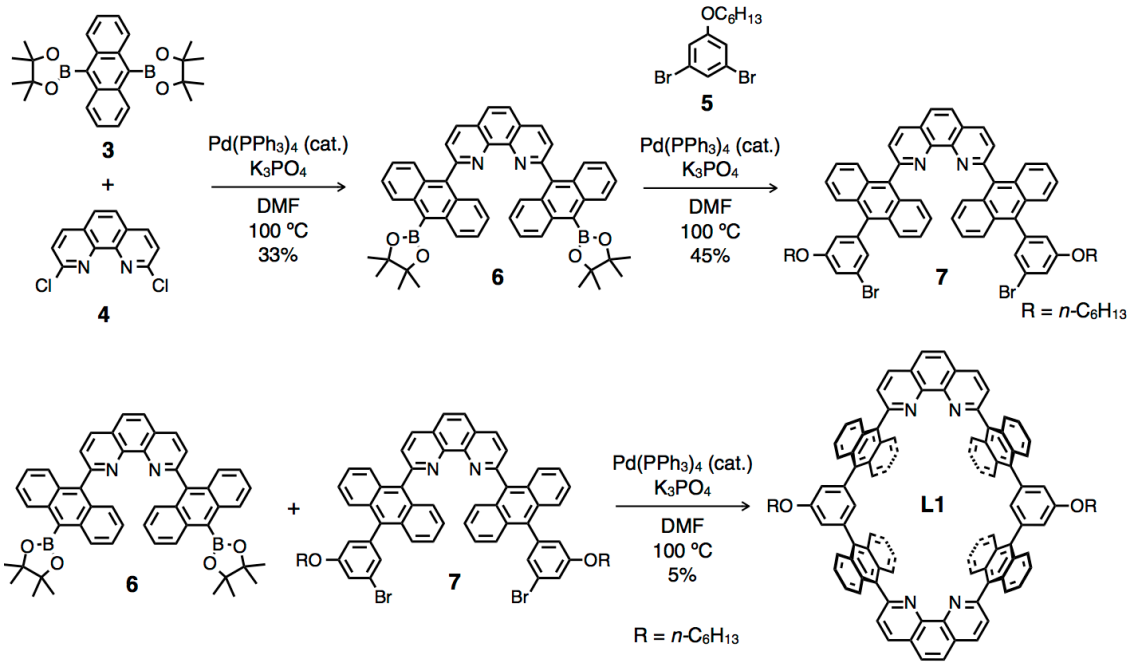

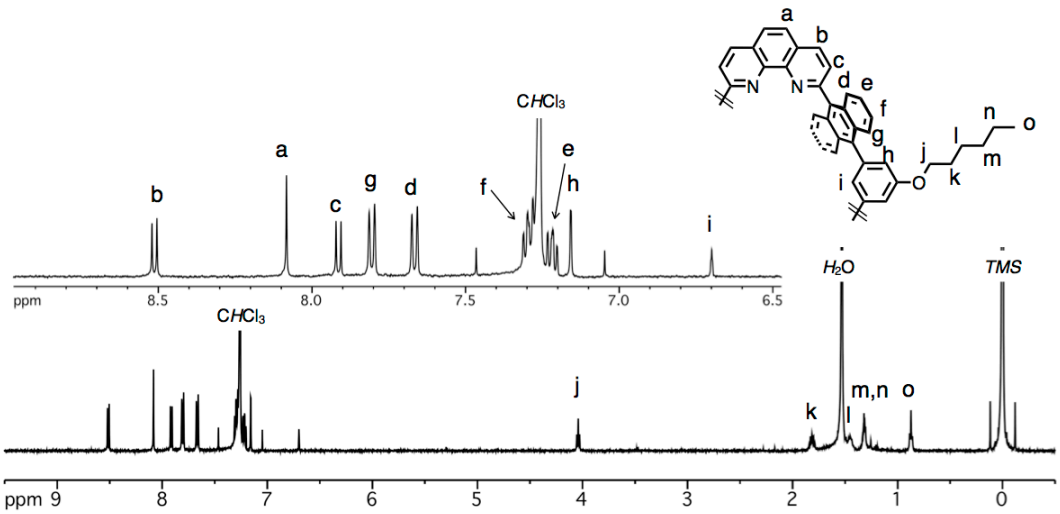

Figure 2–4. ^1H NMR spectra of **L1** (500 MHz, $CDCl_3$, 300 K).

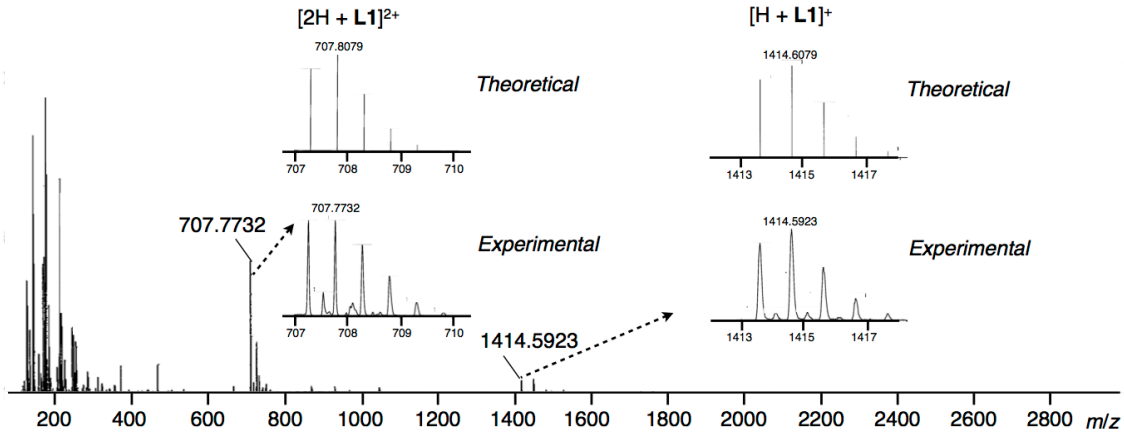

Figure 2–5. ESI-TOF mass spectrum of **L1** in $CHCl_3/CH_3CN$.

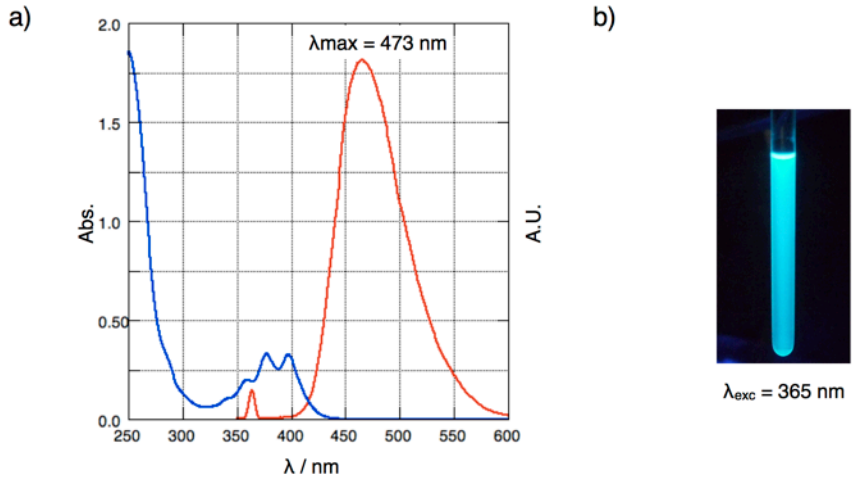

Figure 2–6. a) UV-Vis (blue line, 5 μM, *l* = 1.0 cm, 293 K in $CHCl_3$) and fluorescence (red line, 5 μM, 293 K, λ_{ex} = 365 nm in $CHCl_3$) spectra of **L1** and b) a photo of the emissive **L1** in $CDCl_3$ under UV irradiation (room temperature, λ_{ex} = 365 nm).

A dinuclear Ag(I)-macrocycle $[Ag_2\mathbf{L1}X_2](SbF_6)_2$ (X = Et_2O or H_2O) was prepared by the complexation between **L1** and Ag(I) salt (Scheme 2–2). As an Ag(I) source, $AgSbF_6$ was selected because of the weak Lewis basic character of SbF_6^-, which would not inhibit interaction between guest and Ag(I) centers as a competing coordinative species. Upon reaction between **L1** and 4.0 eq of $AgSbF_6$ in $CHCl_3/(CH_3)_2CO$ followed by crystallization by Et_2O vapor diffusion in the dark, the dinuclear Ag(I)-macrocycle $[Ag_2\mathbf{L1}X_2](SbF_6)_2$ was isolated in 63% yield as yellow crystals. The $[Ag_2\mathbf{L1}X_2](SbF_6)_2$ complex was fully characterized by NMR, ESI-TOF mass, and single crystal X-ray analyses (Figure 2–7–10).

Scheme 2–2. Synthesis of $[Ag_2\mathbf{L1}X_2](SbF_6)_2$.

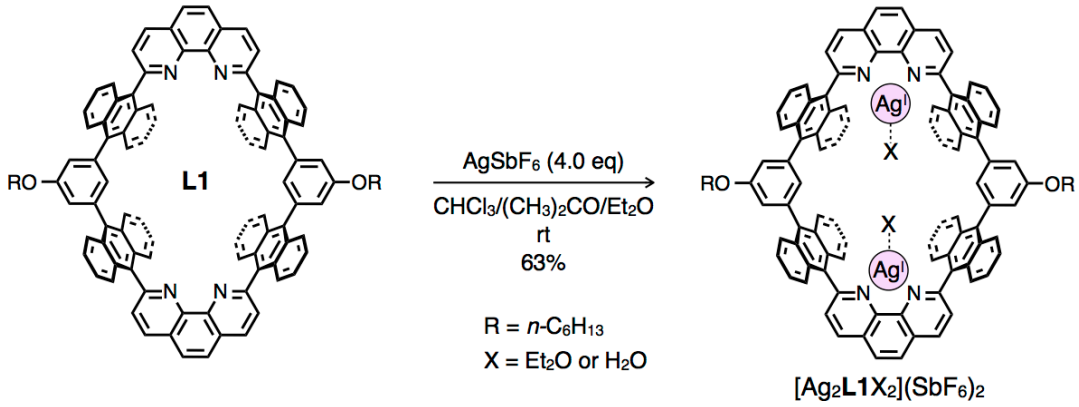

In the resulting crystal structure, the dinuclear Ag(I)-macrocycle exists as a 1:1 co-crystal of $[Ag_2\mathbf{L1}(Et_2O)_2](SbF_6)_2$ and $[Ag_2\mathbf{L1}(H_2O)_2](SbF_6)_2$ (Figure 2–7–8). In each complex, two Ag(I) ions are bound by two phenanthroline ligands in 9.433(1) Å and 9.181(1) Å apart from each other, respectively. In addition to two N-atoms of phenanthrolines, each Ag(I) ion is coordinated by one O-atom of Et_2O or H_2O as a coordinating solvent, respectively, in a trigonal planar coordination geometry. As expected, the dihedral angles among four anthracenes and adjacent aromatic rings were estimated to be around 80–90°. Thus, three dimensional nano-spaces arranged with a face to face arrangement of solvated Ag(I) ions have been created (Figure 2–8).

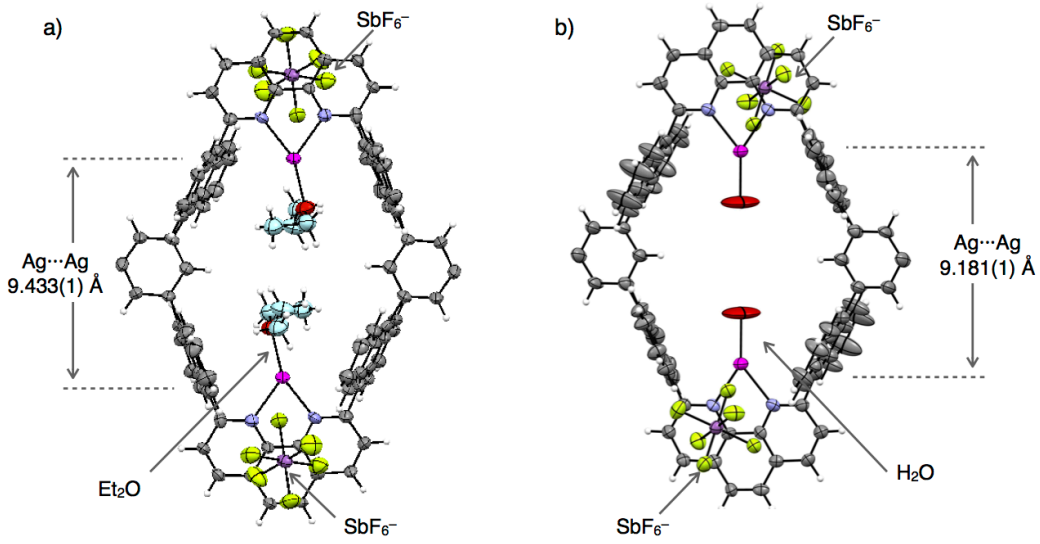

Figure 2–7. ORTEP views (50% probability level) of a) $[Ag_2\mathbf{L1}(Et_2O)_2](SbF_6)_2$ and b) $[Ag_2\mathbf{L1}(H_2O)_2](SbF_6)_2$. Side alkyl-chains are omitted for clarity. (Ag: magenta, C: grey, C of Et_2O: light blue, F: yellow, N: blue, O: red, Sb: pink)

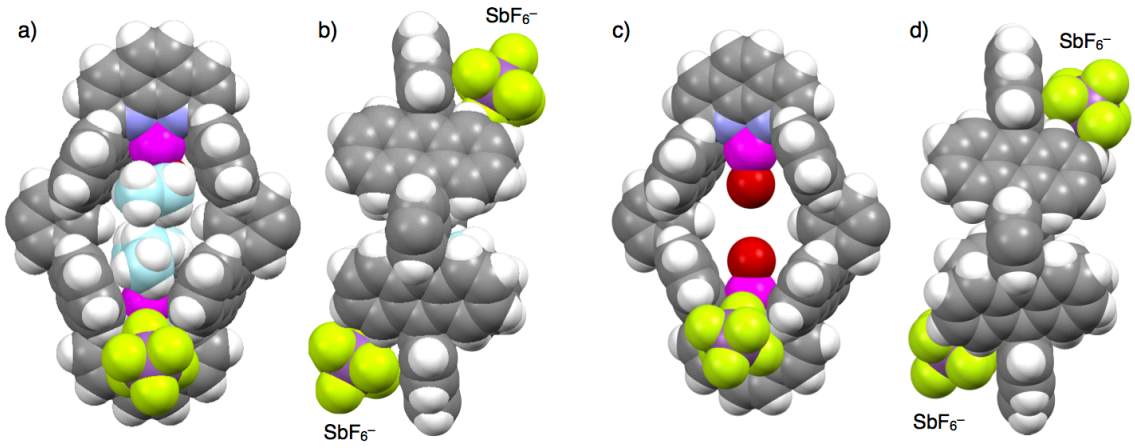

Figure 2–8. Space filling models of a–b) $[Ag_2\mathbf{L1}(Et_2O)_2](SbF_6)_2$ and c–d) $[Ag_2\mathbf{L1}(H_2O)_2](SbF_6)_2$. Side alkyl-chains are omitted for clarity. (Ag: magenta, C: grey, C of Et_2O: light blue, F: yellow, H: white, N: blue, O: red, Sb: pink)

The ^{1}H NMR spectrum of the resulting complex $[Ag_2\mathbf{L1}X_2](SbF_6)_2$ (X = Et_2O or H_2O) in $CDCl_3$ at 300 K showed phenanthroline's signals ($H_{a–c}$) which were approximately 0.2 ppm downfield shifted from those of the original macrocyclic ligand **L1** due to the effect of the coordination with Ag(I) ions (Figure 2–9).[6] Observation of only one single set of phenanthroline's signals suggests that the exchange reaction of bound and free coordinating solvents (Et_2O or H_2O) is faster than the timescale of ^{1}H NMR measurement at 300 K due to the labile nature of the coordination bond between Ag(I) ions and solvent molecules.

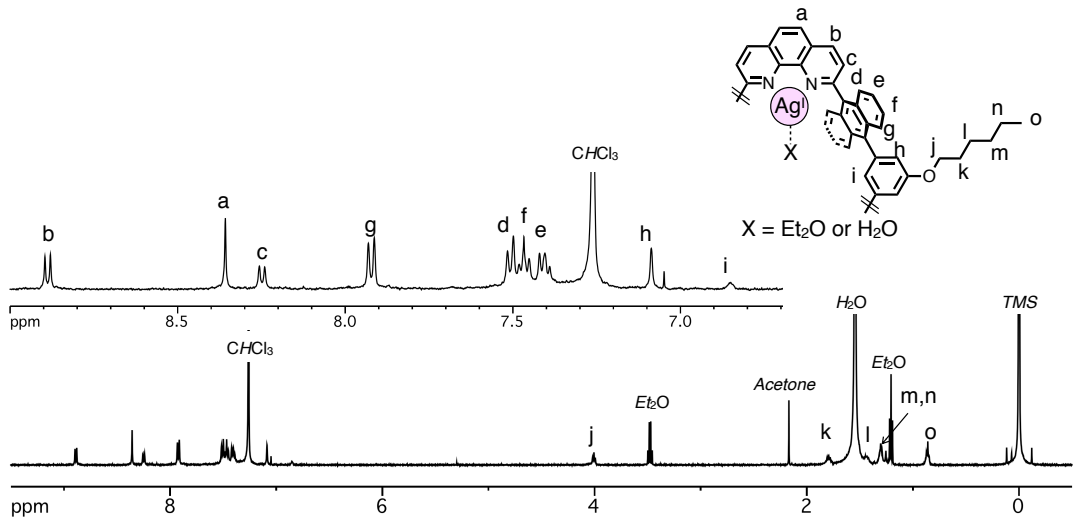

Figure 2–9. ^{1}H NMR spectra of $[Ag_2\mathbf{L1}X_2](SbF_6)_2$ (500 MHz, $CDCl_3$, 300 K). Acetone was included during the processes of crystallization.

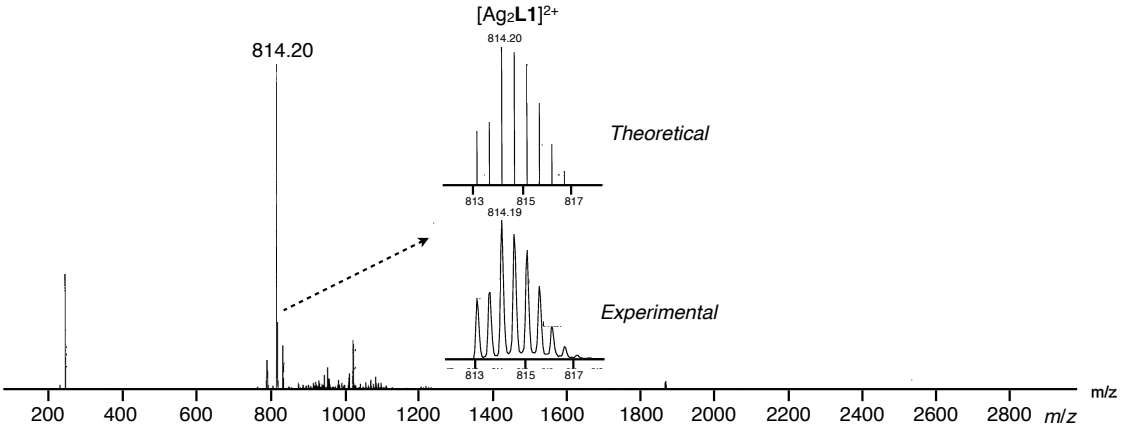

Figure 2–10. ESI-TOF mass spectrum of $[Ag_2\mathbf{L1}X_2](SbF_6)_2$ in $CHCl_3$.

To estimate the stability of the coordination bond between Ag(I) ions and two phenanthrolines, ^{1}H NMR study of a mixtures of isolated $[Ag_2\mathbf{L1}X_2](SbF_6)_2$ and different amounts of **L1** were performed (Figure 2–11). With an increase in the net equivalence of Ag(I) ion, signals of D_{2h}-symmetrical *metal-free* macrocyclic ligand **L1** were firstly replaced by more complicated signals corresponding to C_{2v}-symmetrical *mononuclear* Ag(I)-macrocycle $[Ag\mathbf{L1}X]SbF_6$ (Figure 2–11d,e). Then, the signals were changed into simple D_{2h}-symmetrical signal patterns ascribable to the *dinuclear* Ag(I)-macrocycle $[Ag_2\mathbf{L1}X_2](SbF_6)_2$ (Figure 2–11a–c). These results suggest that the signals of **L1**, $[Ag\mathbf{L1}X]SbF_6$, and $[Ag_2\mathbf{L1}X_2](SbF_6)_2$ were observed separately in $CDCl_3$ at 300 K. Notably, ^{1}H NMR spectrum of isolated $[Ag_2\mathbf{L1}X_2](SbF_6)_2$ showed only one set of signals in highly diluted solution (30 μM) in $CDCl_3$ (Figure 2–11a), indicating that coordination bonding between Ag(I) ion and phenanthroline was stable and the dissociation of Ag(I) ions from $[Ag_2\mathbf{L1}X_2](SbF_6)_2$ was ignorable even in such a low concentration condition.

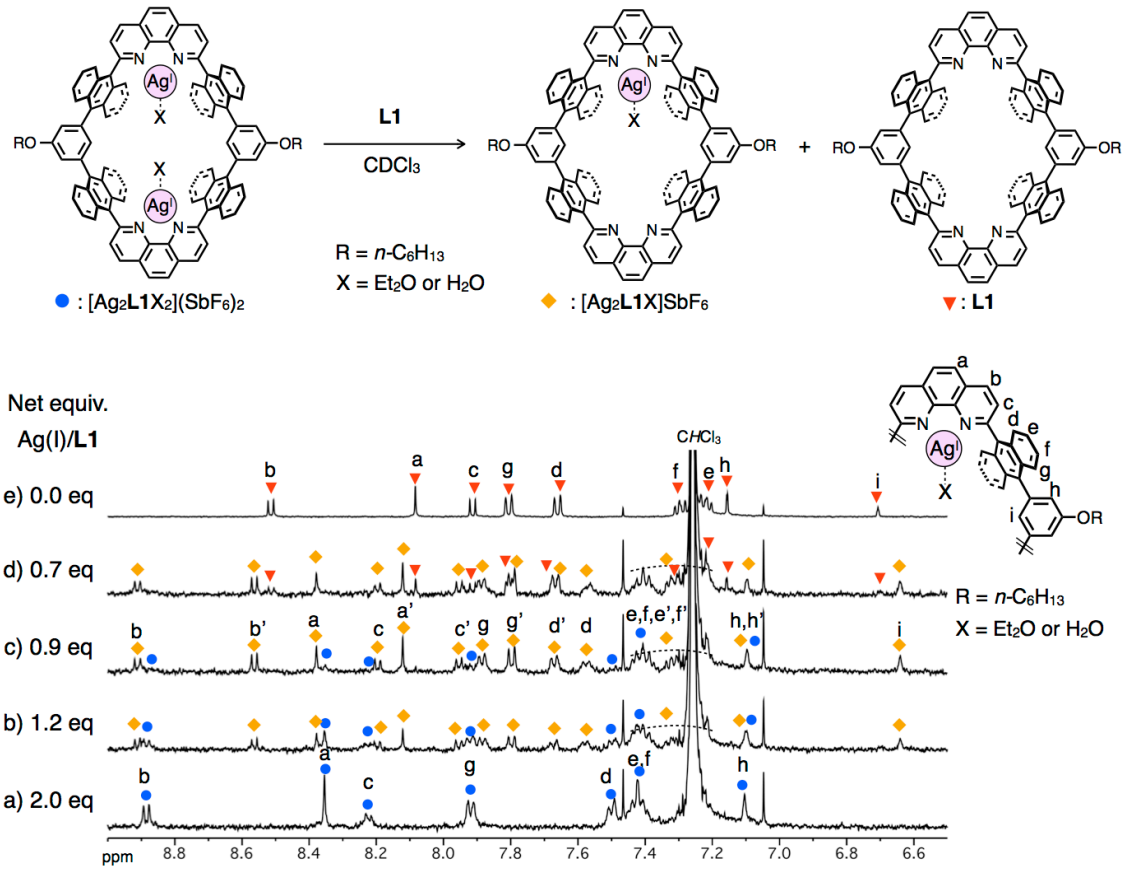

Figure 2–11. Partial ^{1}H NMR spectra of the mixtures of $[Ag_2\mathbf{L1}X_2](SbF_6)_2$ and different amounts of **L1** (500 MHz, $CDCl_3$, 300 K). a) $[[Ag_2\mathbf{L1}X_2](SbF_6)_2]_0$ = 30 μM, $[\mathbf{L1}]_0$ = 0 μM, b) $[[Ag_2\mathbf{L1}X_2](SbF_6)_2]_0$ = 25 μM, $[\mathbf{L1}]_0$ = 17 μM, c) $[[Ag_2\mathbf{L1}X_2](SbF_6)_2]_0$ = 20 μM, $[\mathbf{L1}]_0$ = 27 μM, d) $[[Ag_2\mathbf{L1}X_2](SbF_6)_2]_0$ = 17 μM, $[\mathbf{L1}]_0$ = 35 μM, and e) $[[Ag_2\mathbf{L1}X_2](SbF_6)_2]_0$ = 0 μM, $[\mathbf{L1}]_0$ = 80 μM. $[\mathbf{L1}]_0$ and $[[Ag_2\mathbf{L1}X_2](SbF_6)_2]_0$ indicate the initial concentrations of **L1** and $[Ag_2\mathbf{L1}X_2](SbF_6)_2$, respectively. The net equivalence Ag(I)/**L1** was calculated as follows:

Ag(I)/**L1** = 2 × $[[Ag_2\mathbf{L1}X_2](SbF_6)_2]_0$/($[[Ag_2\mathbf{L1}X_2](SbF_6)_2]_0$ + $[\mathbf{L1}]_0$).

2–3. Host-Guest Interactions between a Dinuclear Ag(I)-Macrocycle and Aromatic Guest Molecules via Ag–π Interactions

As the dinuclear Ag(I)-macrocycle $[Ag_2\mathbf{L1}X_2](SbF_6)_2$ possesses a nano-space equipped with solvated two Ag(I) ions, the cavity would provide a suitable space to include guest molecule(s) through coordination bonding. In this section, guest binding behaviors of $[Ag_2\mathbf{L1}X_2](SbF_6)_2$ were investigated in terms of guest selectivity and stability of inclusion complexes. I found that $[Ag_2\mathbf{L1}X_2](SbF_6)_2$ can bind several kinds of pristine aromatic molecules using Ag–π interaction, by the ligand exchange reaction with coordinating solvents as characterized by NMR, ESI-TOF mass, and single crystal X-ray analyses. Notably, aromatic hydrocarbons, which can form Ag–π interactions with *both* of the two Ag(I) ions of $[Ag_2\mathbf{L1}X_2](SbF_6)_2$, have relatively high affinity to the dinuclear Ag(I)-macrocycle .

2–3–1. Binding of pristine aromatic hydrocarbons

Binding of *p*-xylene, naphthalene, and anthracene as simple pristine aromatic hydrocarbons to $[Ag_2\mathbf{L1}X_2](SbF_6)_2$ was investigated. From ^{1}H NMR titration experiments, these molecules exhibit a different affinity to $[Ag_2\mathbf{L1}X_2](SbF_6)_2$ in $CDCl_3$. Specifically, $[Ag_2\mathbf{L1}X_2](SbF_6)_2$ showed a significantly higher affinity to anthracene than *p*-xylene and naphthalene. The difference in the affinities can be explained by the multiplicity of the Ag–π interaction between the host and guests as suggested from crystal structures of the resulting complexes. This suggests size dependency for the host-guest complexation.

Firstly, the binding behavior of anthracene to $[Ag_2\mathbf{L1}X_2](SbF_6)_2$ was investigated by ^{1}H NMR titration experiment (Figure 2–12). Upon addition of anthracene to a solution of $[Ag_2\mathbf{L1}X_2](SbF_6)_2$ (107 μM) in $CDCl_3$, the host's signals were sequentially shifted due to the host-guest interactions. As the host-guest binding was reversible and the intermolecular exchange reaction of bound and free anthracene was faster than the timescale of ^{1}H NMR, the signals of added anthracene were broadened and could not be observed clearly under this condition at 300 K. Then, to further characterize the details of this host-guest interaction, ^{1}H NMR titration experiment at lower temperature (220 K) was performed (Figure 2–13). At 220 K, the signals of $[Ag_2\mathbf{L1}X_2](SbF_6)_2$ were gradually replaced by a new set of signals as the equivalence of anthracene was increased (Figure 2–13a–c). In the presence of more than 1.0 eq of anthracene, the signals of $[Ag_2\mathbf{L1}X_2](SbF_6)_2$ were almost completely replaced by a new set of signals, and the signals of free anthracene appeared, which suggests the formation of 1:1 host-guest complex, Anthracene⊂$[Ag_2\mathbf{L1}](SbF_6)_2$ (Figure 2–13c–e). At this temperature, the resulting complex showed broadened signals probably due to the fluxional movement of

anthracene bound within the nano-space. Although the broadening of the signals hampered precise assignment of the new signals observed around 6.0–6.5 ppm (**B** on Figure 2–13), some of them should be derived from to those of included anthracene which showed significant upfield shift due to the strong shielding effect from the anthracene walls of $[Ag_2\mathbf{L1}]^{2+}$. The formation of a 1:1 host-guest complex was also supported by ESI-TOF mass measurement (*m*/*z* = 903.72 as Anthracene⊂$[Ag_2\mathbf{L1}]^{2+}$, Figure 2–15). The binding constant between anthracene and Ag(I)-macrocycle (K_a(Anthracene) = [Anthracene⊂$[Ag_2\mathbf{L1}]^{2+}$]/([$Ag_2\mathbf{L1}X_2]^{2+}$[Anthracene])) was determined to be $(3.0 \pm 0.4) \times 10^4$ M^{-1} in $CDCl_3$ at 300 K based on the curve fitting of the ^{1}H NMR data from the titration experiment (Figure 2–14).

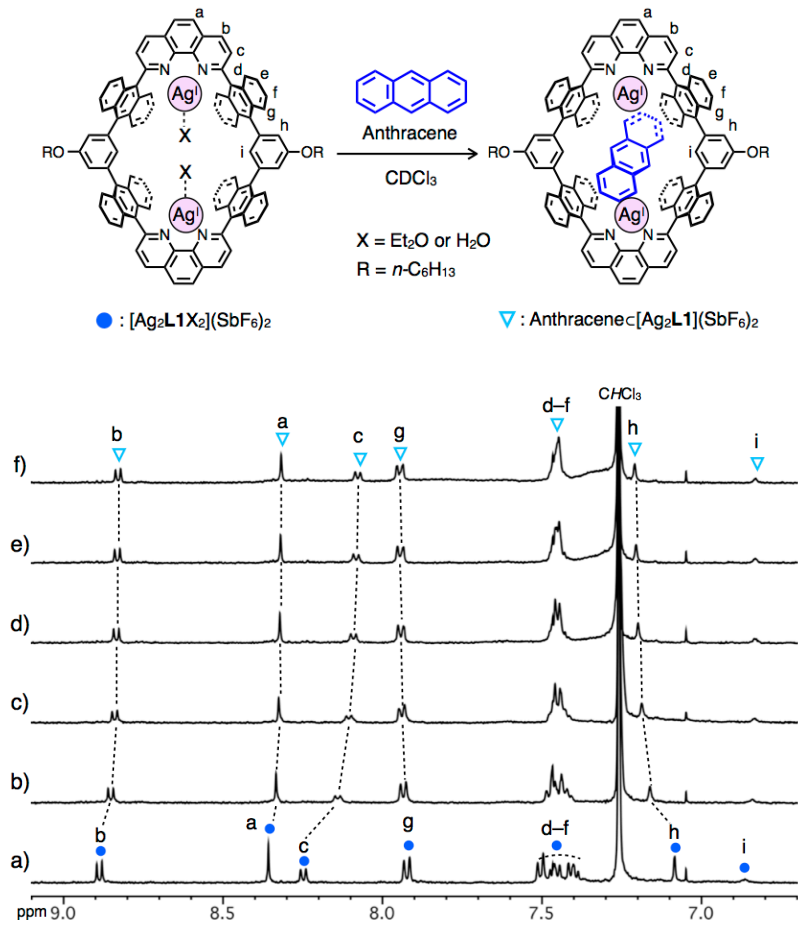

Figure 2–12. Partial ^{1}H NMR spectra of $[Ag_2\mathbf{L1}X_2](SbF_6)_2$ (107 μM) in the presence of a) 0.0, b) 1.0, c) 2.0 d) 3.0, e) 4.0, and f) 5.0 eq of anthracene (500 MHz, $CDCl_3$, 300 K).

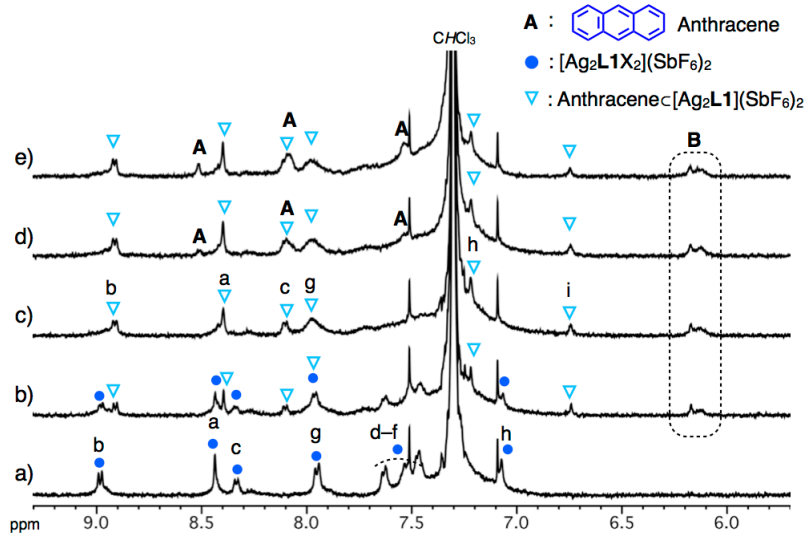

Figure 2–13. Partial ^{1}H NMR spectra of $[Ag_2\mathbf{L1}X_2](SbF_6)_2$ (65 μM) in the presence of a) 0.0, b) 0.5 , c) 1.0 d) 1.5, and e) 2.0 eq of anthracene (500 MHz, $CDCl_3$, 220 K). **A** represent the signals of free anthracene.

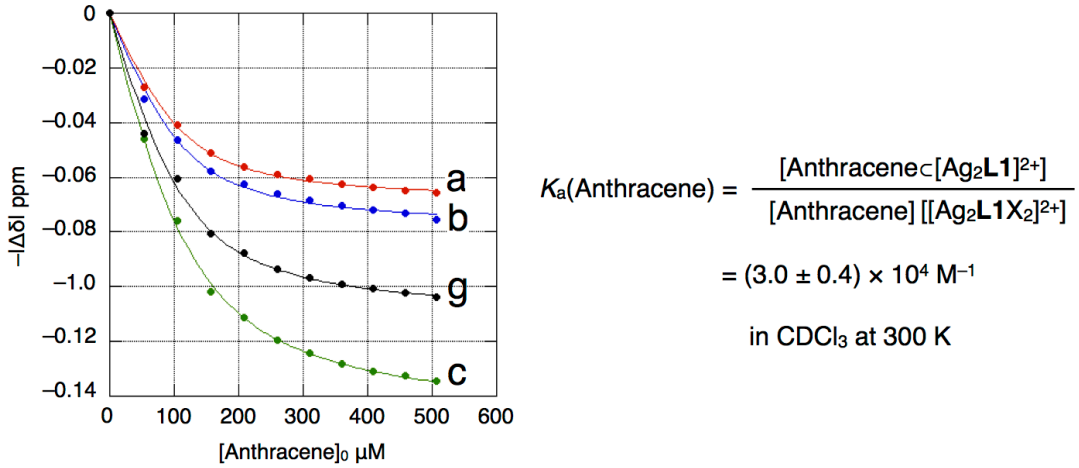

Figure 2–14. Stability constant analysis by the least square fitting to the shift of NMR signals ($H_{a–c, g}$) in the titration experiment described in Figure 2–12 (solid circles: observed, lines: calculated). $[Anthracene]_0$ indicates the initial concentration of anthracene.

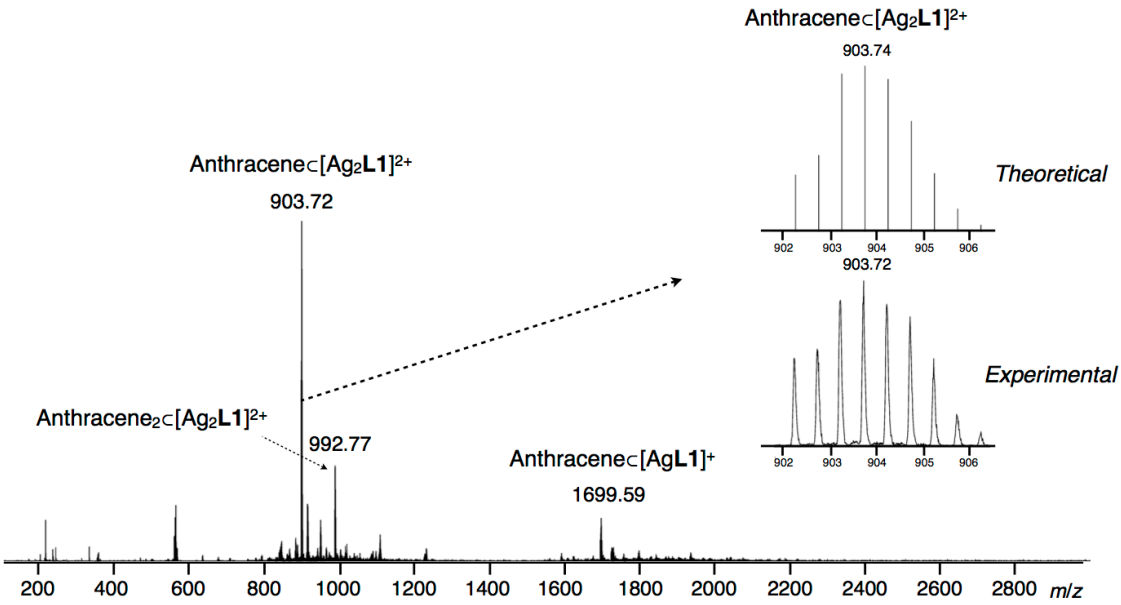

Figure 2–15. ESI-TOF mass spectrum of a mixture of $[Ag_2\mathbf{L1}X_2](SbF_6)_2$ and 5.0 eq of anthracene.

The structure and the binding mode of the resulting complex were determined by single crystal X-ray analysis (Figure 2–16). By *n*-pentane vapor diffusion into a mixture of **L1**, $AgSbF_6$ (4.0 eq), and anthracene (10 eq) in CH_2Cl_2 in the dark at room temperature, yellow brock crystals suitable for single crystal X-ray analysis were obtained. In the resulting crystal structure, one molecule of anthracene was included in the cavity of $[Ag_2\mathbf{L1}]^{2+}$ via η^2-type Ag–π bonding at both terminal edges of the elongated π-surface (Figure 2–16a). The distance between two crystallographically equivalent Ag(I) centers is 8.922(1) Å, which is slightly shorter but approximately identical to those of the original dinuclear Ag(I)-macrocycle (Ag–Ag distances of $[Ag_2\mathbf{L1}X_2](SbF_6)_2$: 9.433(1)–9.181(1) Å). Those Ag(I) ions were in a five-coordinate

distorted square pyramidal coordination geometry with two N-atoms of phenanthroline, two C-atoms of included anthracene, and one Cl-atom of coordinating solvent: CH_2Cl_2 (Ag–N1 2.346(5) Å; Ag–N2 2.284(6) Å; Ag–C67 2.466(8) Å; Ag–C68 2.445(8) Å; Ag–Cl 2.985(2) Å, Figure 2–16c). Multipoint CH–π interactions between H-atoms of included anthracene and π-surface of anthracene walls of the host may stabilize the resulting complex (C–π distances: ca. 3.5 Å, Figure 2–16a,b).

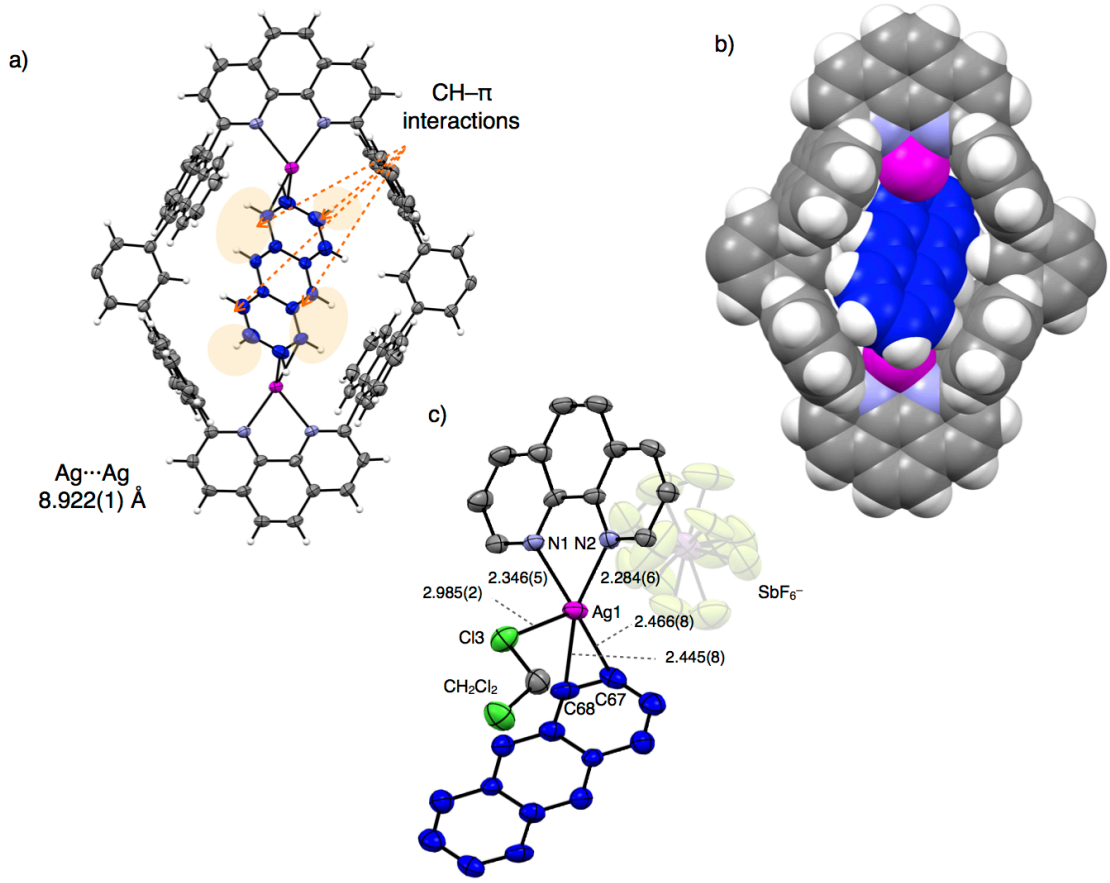

Figure 2–16. Crystal structure of Anthracene⊂$[Ag_2$**L1**$(CH_2Cl_2)_2](SbF_6)_2$. a) ORTEP view (50% probability level), b) space filling model, and c) ORTEP view of a partial structure (some part of solvent, side-alkyl chains, counter anions and H-atoms are omitted for clarity). (Ag: magenta, C: grey, C of anthracene: blue, Cl: pale green F: yellow, H: white, N: blue, O: red, Sb: pink)

In contrast to the case of anthracene, smaller aromatic hydrocarbons such as *p*-xylene and naphthalene showed lower affinities to $[Ag_2$**L1**$X_2](SbF_6)_2$. Upon addition of *p*-xylene or naphthalene to a solutions of $[Ag_2$**L1**$X_2](SbF_6)_2$ (107 μM) in $CDCl_3$, signals of $[Ag_2$**L1**$X_2](SbF_6)_2$ at the aromatic region slightly shifted, but did not converge even when more than 5.0 eq of guests were added (Figure 2–17–19). Such almost stationary ^{1}H NMR spectra during titration experiments suggest weak host-guest interactions. It should be noted that, in the

case of the titration experiment using anthracene as a guest, the shift of the signals was almost converged under the same condition (Figure 2–14).

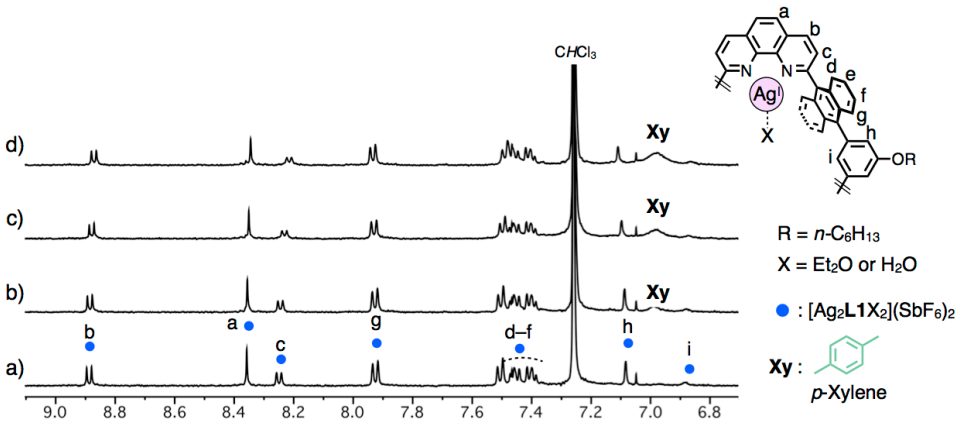

Figure 2–17. Partial ^{1}H NMR spectra of $[Ag_2\mathbf{L1}X_2](SbF_6)_2$ (107 μM) in the presence of a) 0.0, b) 1.0 , c) 3.0, and d) 5.0 eq of *p*-xylene (500 MHz, $CDCl_3$, 300 K).

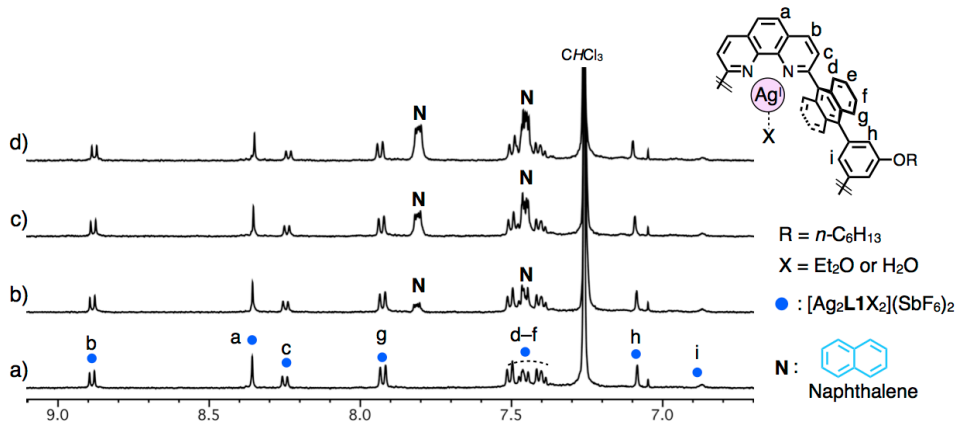

Figure 2–18. Partial ^{1}H NMR spectra of $[Ag_2\mathbf{L1}X_2](SbF_6)_2$ (107 μM) in the presence of a) 0.0, b) 1.0 , c) 3.0, and d) 5.0 eq of naphthalene (500 MHz, $CDCl_3$, 300 K).

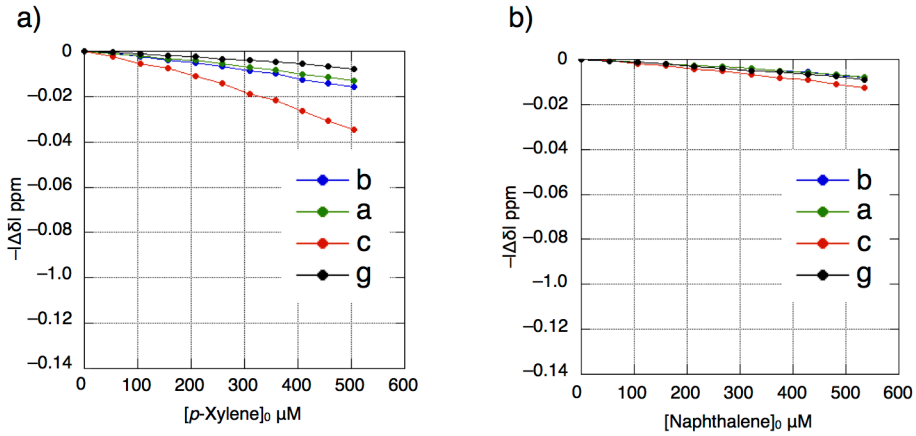

Figure 2–19. Plots of the amounts of shift change of the ^{1}H NMR signals ($H_{a–c,g}$) against the concentrations of a) *p*-xylene and b) naphthalene. The spectra are shown in Figure 2–17,18. $[p\text{-Xylene}]_0$ and $[\text{Naphthalene}]_0$ indicate the initial concentrations of *p*-xylene and naphthalene, respectively.

In spite of such a weak host-guest interaction between $[Ag_2\mathbf{L1}X_2]^{2+}$ and *p*-xylene in solution, single crystals of a *p*-xylene inclusion complex were isolated from CH_2Cl_2/*p*-xylene = 4/1, in which two *p*-xylene are simultaneously accommodated within the nano-space (Figure 2–20). Upon mixing **L1** and 20 eq of $AgCF_3SO_3$ in *p*-xylene/CH_2Cl_2 = 1/4 in the dark for a week at room temperature, yellow single crystals of (*p*-Xylene)$_2$⊂$[Ag_2\mathbf{L1}(CF_3SO_3)_2]$ were obtained in 75% yield. Single crystal X-ray analysis of the resulting complex revealed the formation of host-guest complex, (*p*-Xylene)$_2$⊂$[Ag_2\mathbf{L1}(CF_3SO_3)_2]$ (Figure 2–20). In the resulting structure two stacked *p*-xylene molecules are bound simultaneously to the Ag(I) centers of the macrocycle forming an η^1-or η^2-type Ag–π interactions with an average bond distance of Ag–C = 2.53 Å (Figure 2–20b,c,e,f). The distance between two Ag(I) ions within the nano-space was 8.89(0) Å, which is slightly shorter but approximately identical to those of the original dinuclear Ag(I)-macrocycle (Ag–Ag distances of $[Ag_2\mathbf{L1}X_2](SbF_6)_2$: 9.433(1)–9.181(1) Å). Each Ag(I) ion forms a four- to five-coordinate structure with two N-atoms of phenanthrolines, C-atoms of *p*-xylene and one O-atoms of disordering $CF_3SO_3^-$ (Ag–N 2.31(1)–2.33(1) Å; Ag–C 2.40(3)–2.70(3) Å; Ag–O 2.47(3)–2.65(1) Å, Figure 2–20b,c,e,f). The staked *p*-xylene molecules existed in a substitutionary disordering manner (occupancy: 53% and 47%) with π–π distances of ca. 3.5 Å (Figure 2–20a,d). Besides Ag–π interactions, there are multipoint CH–π interactions between anthracene walls and included *p*-xylenes (Figure 2–20a,d).

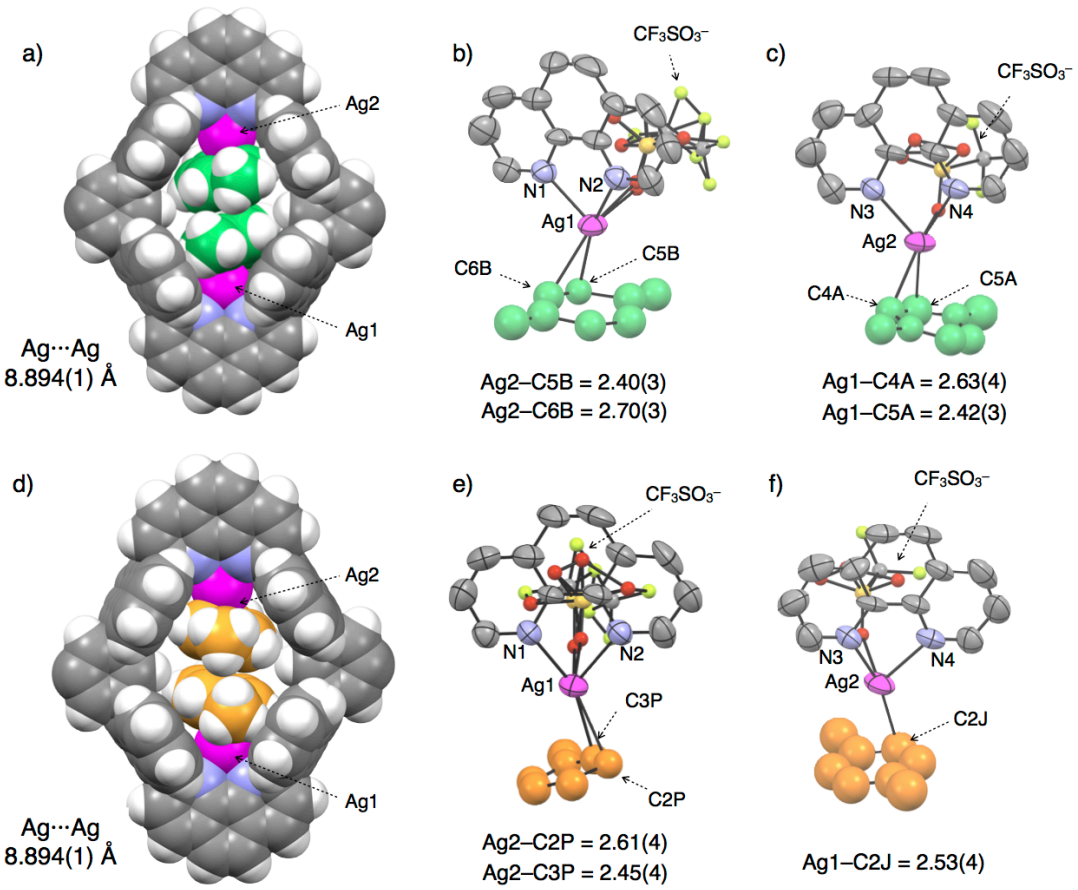

Figure 2–20. Crystal structure of (p-Xylene)$_2$⊂[Ag_2**L1**$(CF_3SO_3)_2$]. a,d) Space filling models, and b,c,e,f) ORTEP views (50% probability level) of a partial structure (some parts of solvent, side-alkyl chains, counter anions, and H-atoms are omitted for clarity). (Ag: magenta, C: grey, C of p-xylene: light green and deep orange, F: yellow, H: white, N: blue, O: red, S: orange). p-Xylene molecules are colored based on the disordering pattern. (Occupancies: a–c) 53% (light green), d–f) 47% (orange)).

Considering from the distinct contrast between crystal structures of Anthracene⊂[Ag_2**L1**](SbF_6)$_2$ and (p-Xylene)$_2$⊂[Ag_2**L1**(CF_3SO_3)$_2$], the difference in the host-guest affinities between [Ag_2**L1**X_2](SbF_6)$_2$ and anthracene, naphthalene, and p-xylene can be explained by the relationship between the size of guests and the mode of arrangement of Ag(I) ions within the nano-space as described on Figure 2–21. In the case of Anthracene⊂[Ag_2**L1**](SbF_6)$_2$, the guest molecule is large (C2–C7 = 7.3 Å) enough to form Ag–π interactions with both of the two Ag(I) ions within the nano-space with the Ag–C distances of ca. 2.45 Å (Figure 2–21). On the other hand, in the cases of p-xylene (C1–C4 = 2.8 Å) and naphthalene (C2–C7 = 4.8 Å), the sizes of the guests were not suitable to simultaneously bind to *both* of the Ag(I) centers within the nano-space of [Ag_2**L1**X_2](SbF_6)$_2$ (Figure 2–21).

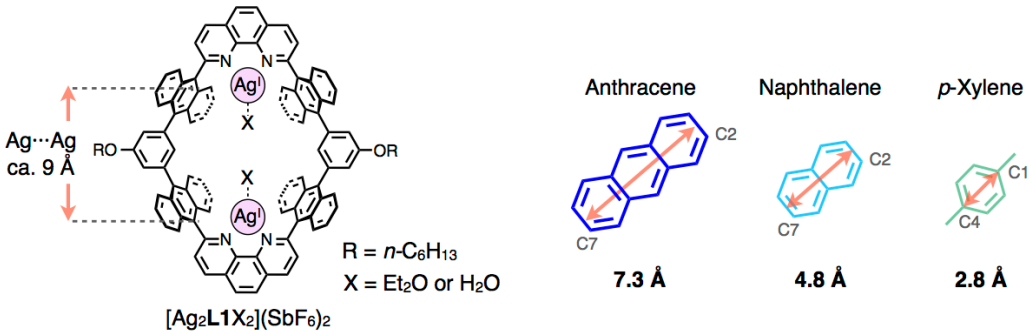

Figure 2–21. Comparisons of the Ag–Ag distance of [Ag_2**L1**X_2](SbF_6)$_2$ and the sizes of pristine aromatic molecules.

The above results indicate that *multiple* Ag–π interactions within [Ag_2**L1**X_2](SbF_6)$_2$ work as an effective driving force to bind pristine aromatic molecules like anthracene which can reach both of the Ag(I) ions within the nano-space. Moreover, the mode of arrangement of Ag(I) ions seemed to control the selectivity of aromatic guest molecules.

2–3–2. Binding of a sandwich-shaped aromatic molecule

From the experimental results described in the previous section, multipoint Ag–π interactions between $[Ag_2\mathbf{L1}X_2](SbF_6)_2$ and π-surfaces of aromatic rings work as an effective driving force to bind pristine aromatic molecules. The above-mentioned crystal structure of *p*-xylene inclusion complex (*p*-Xylene)$_2$⊂$[Ag_2\mathbf{L1}(CF_3SO_3)_2]$ (Figure 2–20) encouraged me to incorporate [2.2]paracyclophane (pCp) as a sandwich shaped aromatic molecule, which has two stacked *p*-phenylene rings covalently connected by two alkyl chains in a π–π distance of 3.1 Å. I then found that $[Ag_2\mathbf{L1}X_2](SbF_6)_2$ can effectively bind to one pCp molecule with a significantly high binding constant ($K_a > 10^9$ M^{-1} in $CDCl_3$ at 300 K), as revealed by NMR, ESI-TOF mass and single crystal X-ray analyses. Control experiments using host molecules which have similar structures to $[Ag_2\mathbf{L1}X_2](SbF_6)_2$ revealed that multipoint Ag–π interactions between pCp and Ag(I) centers of $[Ag_2\mathbf{L1}X_2](SbF_6)_2$ works as a major driving force for pCp binding.

The binding behavior of pCp to Ag(I)-macrocycle was studied by ^{1}H NMR titration experiment (Figure 2–22). Upon adding pCp to a solution of dinuclear Ag(I)-macrocycle $[Ag_2\mathbf{L1}X_2](SbF_6)_2$ (107 μM) in $CDCl_3$, the signal intensity of the original $[Ag_2\mathbf{L1}X_2](SbF_6)_2$ gradually decreased, which were replaced by a new set of signals assignable to the D_{2h}-symmetrical macrocyclic structure (Figure 2–22b). The signals of $[Ag_2\mathbf{L1}X_2](SbF_6)_2$ were completely replaced by the new signals in the presence of 1.0 eq of pCp (Figure 2–22c). This result suggests the formation of a 1:1 inclusion complex pCp⊂$[Ag_2\mathbf{L1}](SbF_6)_2$. Considering from the integral ratios of the NMR signals, the new singlet peaks appeared at 3.82 ppm and 1.17 ppm (A_{in} and B_{in}, respectively, in Figure 2–22c) can be assigned as those of the protons of included pCp. These signals were significantly upfield shifted due to the strong shielding effect from the anthracene walls ($\Delta\delta$ = –2.6 and –1.9 ppm for A_{in} and B_{in}, respectively). This assignment was strongly supported by the distinct rotating frame Overhauser effect (ROE) correlation between A_{in} and the protons (H_i) inside the cavity of $[Ag_2\mathbf{L1}X_2](SbF_6)_2$ (Figure 2–23). Although the host-guest binding was reversible, the intermolecular exchange reaction between bound and free pCp molecules was slower than the timescale of ^{1}H NMR at 300 K in $CDCl_3$, because the signals of $[Ag_2\mathbf{L1}X_2](SbF_6)_2$ and pCp⊂$[Ag_2\mathbf{L1}](SbF_6)_2$ were observed separately each other in the presence of less than 1.0 eq of pCp (Figure 2–22b). The formation of pCp⊂$[Ag_2\mathbf{L1}](SbF_6)_2$ was also supported by ESI-TOF mass spectrometry (*m*/*z* = 918.80 for pCp⊂$[Ag_2\mathbf{L1}]^{2+}$, Figure 2–24).

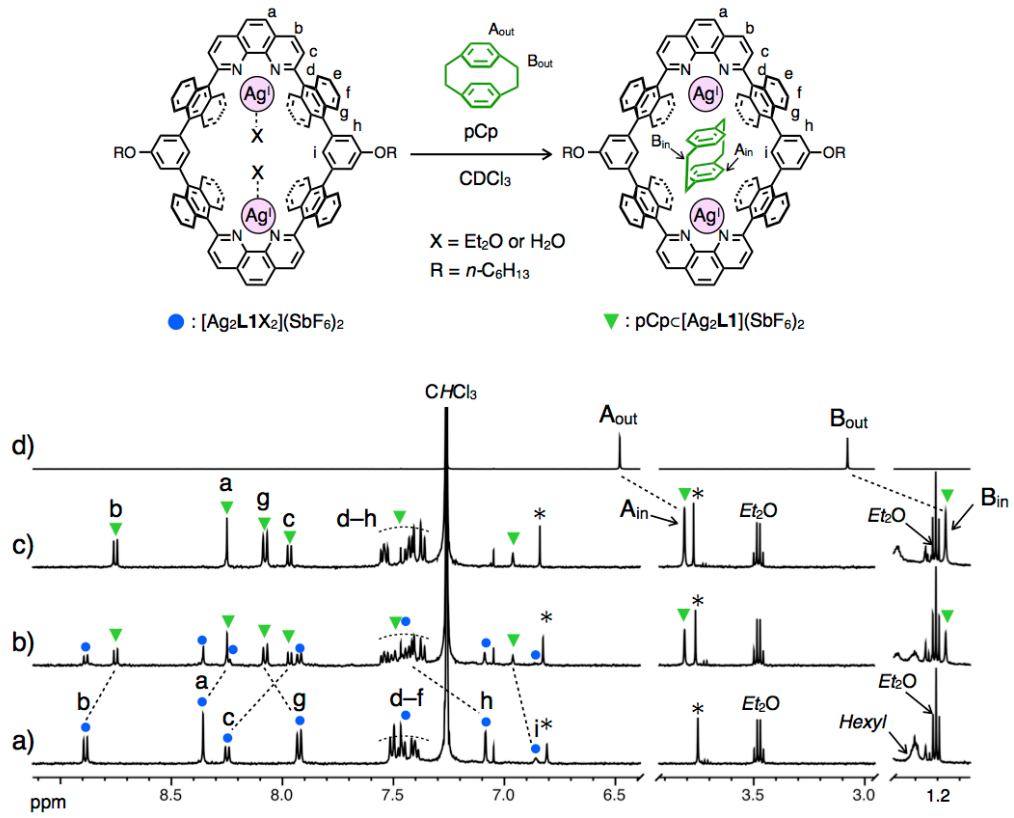

Figure 2–22. Partial ^{1}H NMR spectra of $[Ag_2\mathbf{L1}X_2](SbF_6)_2$ (107 μM) in the presence of a) 0.0, b) 0.5, and c) 1.0 eq of pCp, and d) pCp only (500 MHz, $CDCl_3$, 300 K). Asterisks represent the signals of *p*-dimethoxybenzene used as the internal standard.

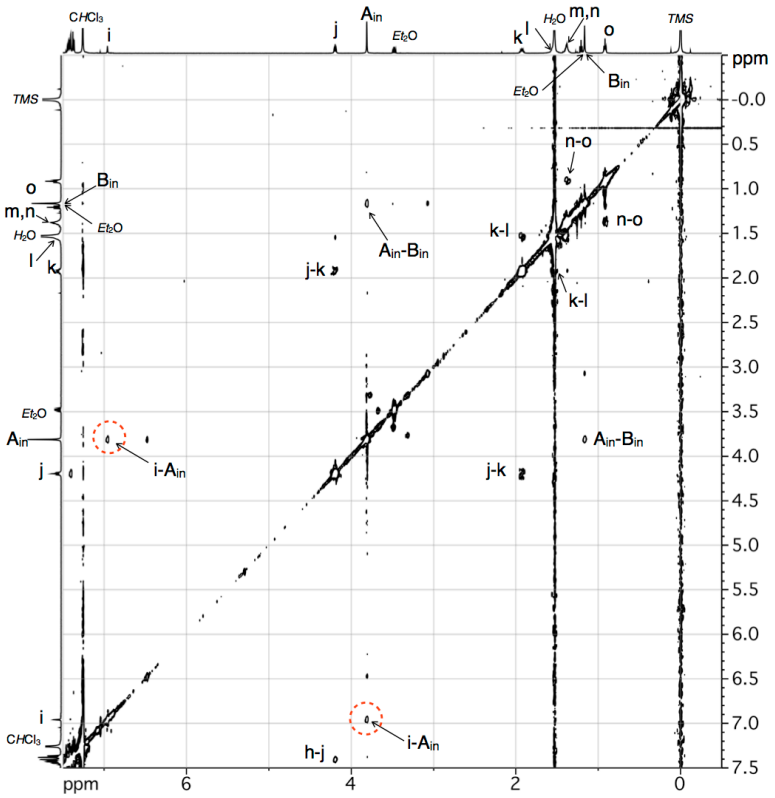

Figure 2–23. Partial ^{1}H-^{1}H ROESY spectrum of pCp⊂$[Ag_2\mathbf{L1}](SbF_6)_2$ (500 MHz, $CDCl_3$, 300 K).

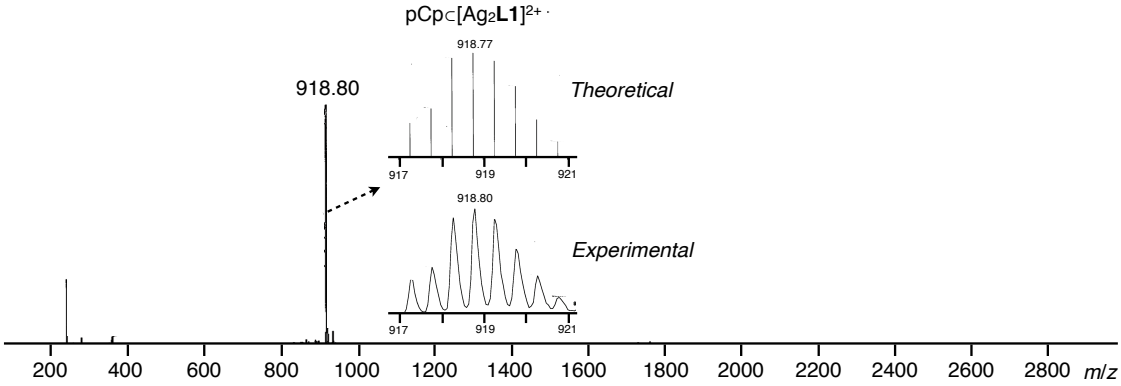

Figure 2–24. ESI-TOF mass spectrum of a mixture of **L1**, $AgSbF_6$ (4.0 eq), and pCp (2.3 eq) in $CDCl_3$.

The structure and the binding mode of this host-guest complex were determined by single crystal X-ray analysis. Ether vapor diffusion into a mixture of $AgSbF_6$ (4.0 eq), **L1** and pCp (1.0 eq) in $CHCl_3/(CH_3)_2CO$ in the dark yielded yellow plate crystals in 71% yield, which were suitable for single crystal X-ray analysis. In the resulting crystal structure, one molecule of pCp is included within the nano-space of the dinuclear Ag(I)-macrocycle in two substitutionary disordering manners (occupancies: 56% and 44%) (Figure 2–25). The distance between two crystallographically equivalent Ag(I) centers is 8.514(1) Å, which is slightly shorter but approximately identical to those of the original dinuclear Ag(I)-macrocycle (Ag–Ag distances of $[Ag_2\mathbf{L1}X_2](SbF_6)_2$: 9.433(1)–9.181(1) Å). Two Ag(I) ions form a distorted tetrahedral coordination geometry with two N-atoms of phenanthrolines and two C-atoms of pCp without coordinating solvents or anions (Ag–N1 2.342(6) Å; Ag–N2 2.327(5) Å; Ag–C 2.39(1)–2.56(1) Å, Figure 2–25b,d). Notably, the π-planes of pCp form η^2-type Ag–π interactions with both of the Ag(I) ions within the nano-space. Although, the direction of these Ag–π bonding are inclined about 30° from the vertical direction of the π-plane of pCp, the resulting Ag–π–π–Ag structure is quite similar to the case of the $(p\text{-Xylene})_2\subset[Ag_2\mathbf{L1}(CF_3SO_3)_2]$ as described in the previous section (Figure 2–20). Besides Ag–π interactions, pCp within the nano-space forms multipoint CH–π interactions with anthracene walls (C–π distances: ca. 3.4 Å), which may stabilize this host-guest complex as well (Figure 2–25a,c).

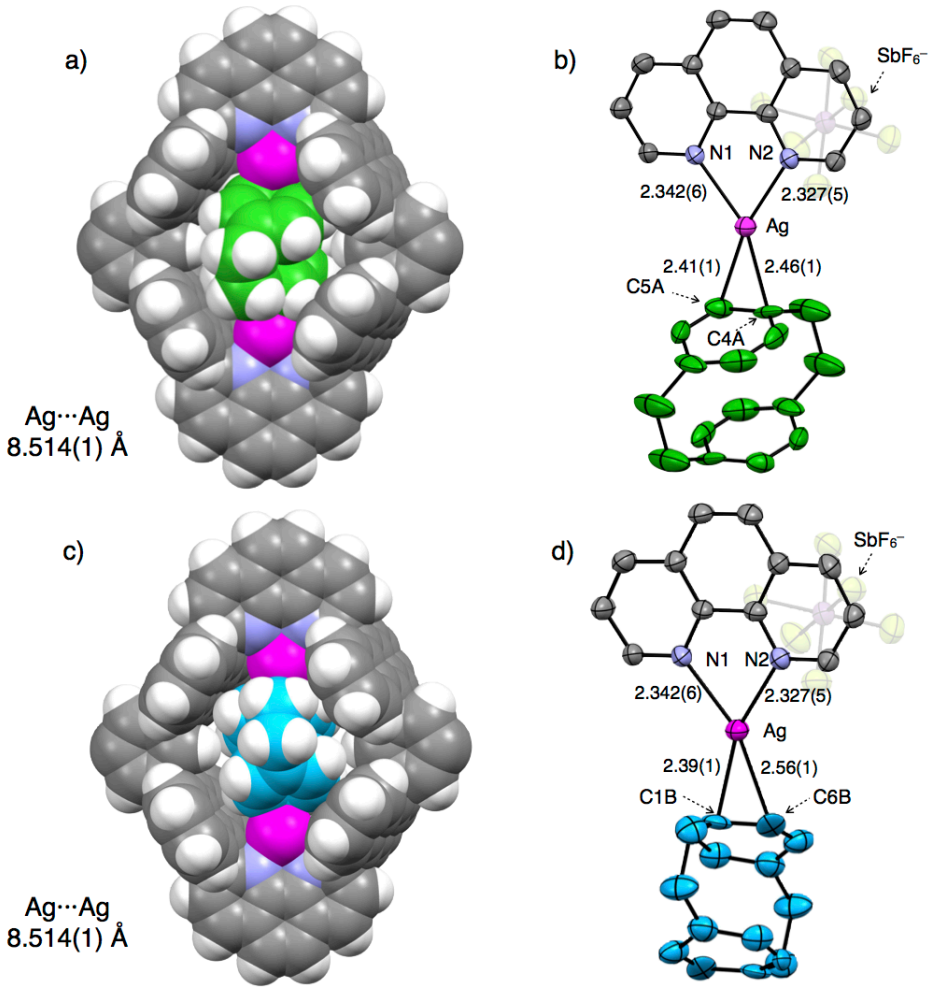

Figure 2–25. Crystal structure of pCp⊂[Ag_2**L1**]$(SbF_6)_2$. a,c) Space filling models, and b,d,) ORTEP views (50% probability level) of a partial structure (some parts of solvent, side-alkyl chains, counter anions, and H-atoms are omitted for clarity). (Ag: magenta, C: grey, C of pCp : green and pale blue, F: yellow, H: white, N: blue, O: red, Sb: pink). pCp is colored based on the disordering patterns (a–b) 56% (green), c–d) 44% (pale blue)).

The ^{1}H NMR spectrum of the isolated single crystal in $CDCl_3$ showed identical signal patterns as that of aforementioned titration experiments (Figure 2–26a). This indicates the composition of the host-guest complex in solution was the same as that in the crystalline state. Notably, in the crystal, pCp within the nano-space is inclined and showed a C_i symmetrical structure because of the desymmetrization by an η^2-type Ag–π bonding (Figure 2–25), whereas ^{1}H NMR signals of the included pCp shows only two singlets (A_{in} and B_{in}) corresponding to a D_{2h}-symmetrical structure (Figure 2–22c). This suggests pCp exhibits fast and fluxional oscillation or a precession movement within the nano-space of Ag(I)-macrocycle via haptotropic shifts of Ag(I) ions in the time scale of ^{1}H NMR in $CDCl_3$ at 300 K, whereas any rotational movements of pCp in the nano-space were likely to be sterically inhibited.

The binding constant between pCp and [Ag_2**L1**X_2]$(SbF_6)_2$ (K_a(pCp) =

[pCp⊂[Ag_2**L1**]$^{2+}$]/([pCp][[Ag_2**L1**]$^{2+}$]) M^{-1}) was estimated by ^{1}H NMR titration experiments in $CDCl_3$ at 300 K. Notably, K_a(pCp) was too large to directly determine from ^{1}H NMR titration experiments at the concentration of about 10^2 μM, a guest competition experiment in the presence of ferrocene ($FeCp_2$) as a competing guest was conducted, where, K_a($FeCp_2$) = [$FeCp_2$⊂[Ag_2**L1**]$^{2+}$]/([$FeCp_2$][[Ag_2**L1**]$^{2+}$]) = 6.2 ± 0.9 × 10^4 M^{-1} in $CDCl_3$ at 300 K (the binding behavior of $FeCp_2$ is described on the section 2–3–3) (Figure 2–26). However, upon addition of an excess amount (25 eq) of $FeCp_2$ to a solution of pCp⊂[Ag_2**L1**]$(SbF_6)_2$ in $CDCl_3$ at 300 K, no guest exchanges were observed in ^{1}H NMR study (Figure 2–26b). This result suggests K_a(pCp) > 10^9 M^{-1} in $CDCl_3$ at 300 K.

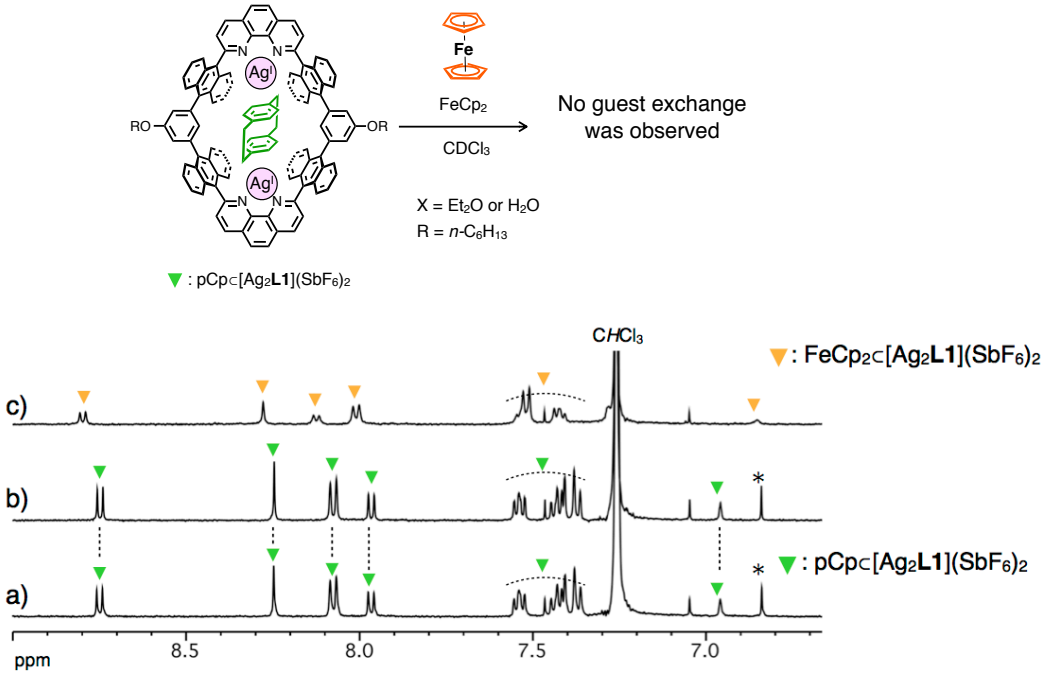

Figure 2–26. ^{1}H NMR spectra of pCp⊂[Ag_2**L1**]$(SbF_6)_2$ (115 μM) in the presence of a) 0.0 and b) 25 eq of $FeCp_2$. c) ^{1}H NMR spectra of a mixture of [Ag_2**L1**X_2]$(SbF_6)_2$ (105 μM) and $FeCp_2$ (5.0 eq) (500 MHz, $CDCl_3$, 300 K). An asterisk represents the signal of *p*-dimethoxybenzene used as the internal standard.

Strong host-guest interaction between $[Ag_2\mathbf{L1}X_2](SbF_6)_2$ and pCp was also supported by titration experiments using UV-Vis spectroscopy (Figure 2–27). Upon adding pCp to the solution of $[Ag_2\mathbf{L1}X_2](SbF_6)_2$ (50 μM) in $CHCl_3$, the spectrum of $[Ag_2\mathbf{L1}X_2](SbF_6)_2$ slightly changed. The absorption change converged in the presence of 1.0 eq of pCp (Figure 2–27b), which suggests quantitative formation of the host-guest complex pCp⊂$[Ag_2\mathbf{L1}X_2](SbF_6)_2$ in such a highly diluted condition (50 μM) due to strong host-guest interaction. It should be noted that the slight change in the absorption of $[Ag_2\mathbf{L1}X_2](SbF_6)_2$ suggests existence of no remarkable charge transfer interaction between Ag(I) centers and pCp (Figure 2–27a).

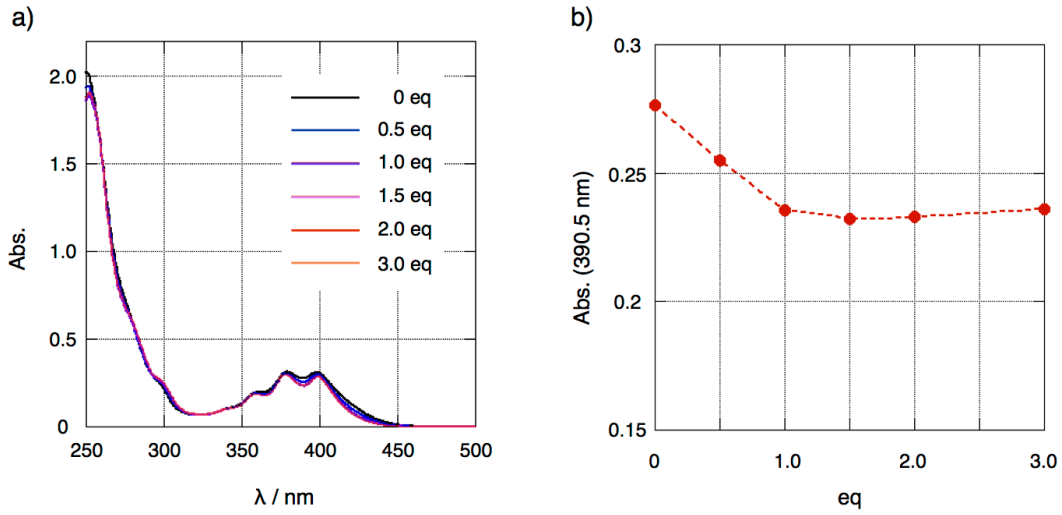

Figure 2–27. a) UV-Vis spectra of the mixtures of $[Ag_2\mathbf{L1}X_2](SbF_6)_2$ and different amounts of pCp ([$[Ag_2\mathbf{L1}X_2](SbF_6)_2$] = 50 μM, l = 0.1 cm, 293 K in $CHCl_3$), b) absorption change at 390.5 nm vs equivalence of pCp to $[Ag_2\mathbf{L1}X_2](SbF_6)_2$.

Such an extremely strong host-guest interaction is attributed to the multipoint Ag–π interactions within nano-space of $[Ag_2\mathbf{L1}X_2](SbF_6)_2$ as qualitatively evaluated by the following control experiments.

Firstly, to evaluate the contribution of Ag–π interaction to the stability of the inclusion complex pCp⊂$[Ag_2\mathbf{L1}](SbF_6)_2$, control experiments using **L1** or $[M_2\mathbf{L1}X_m]^{n+}$ (M = Hg(II), Cu(I), and Zn(II); X = solvent or anion) in $CDCl_3/(CD_3)_2CO$ (= 75/1–75/0) at 300 K were performed (Figure 2–28–29). Even when an excess amount of pCp was added to a solution of each host, the spectral patterns of the host and guest showed almost no changes, suggesting weak host-guest interactions. It should be noted that the existence of counter anions ($CF_3SO_3^-$ or BF_4^-) or $(CD_3)_2CO$ did not have large effects on the results of these control experiments. Indeed, the dinuclear Ag(I) complex of **L1** with SbF_6^-, $CF_3SO_3^-$, or BF_4^- as counter anions showed high affinities to pCp in $CDCl_3/(CD_3)_2CO$ (= 75/1) as investigated by ^{1}H NMR titration experiments

(Figure 2–30). Above-mentioned results suggest Ag–π interactions work as a major driving force to include pCp into $[Ag_2\mathbf{L1}X_2](SbF_6)_2$.

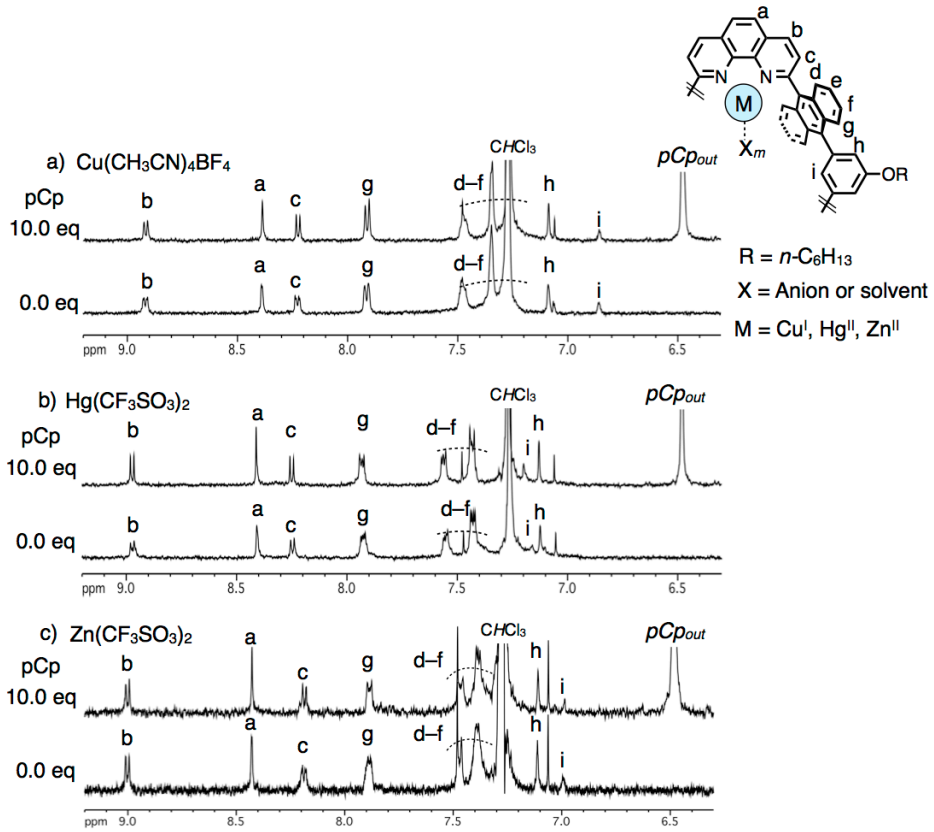

Figure 2–28. Partial ^{1}H NMR spectra of mixtures of **L1** (70 μM), metal sources (3.8 eq), and 0.0–10 eq of pCp (500 MHz, $CDCl_3/(CD_3)_2CO$ = 75/1, 300 K). Metal sources: a) $Cu(CH_3CN)_4BF_4$, b) $Hg(CF_3SO_3)_2$, and c) $Zn(CF_3SO_3)_2$.

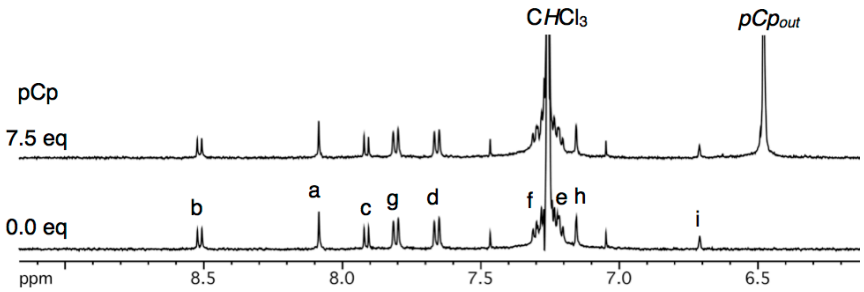

Figure 2–29. Partial ^{1}H NMR spectra of mixtures of **L1** (125 μM) and 0.0–7.5 eq of pCp (500 MHz, $CDCl_3$, 300 K).

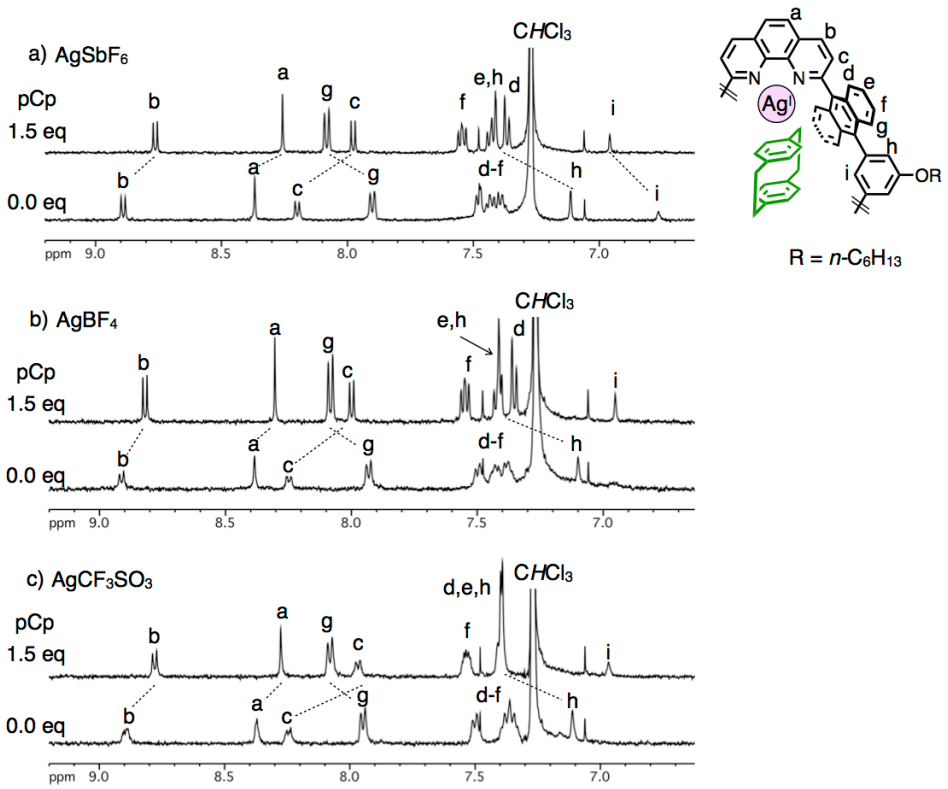

Figure 2–30. Partial ^{1}H NMR spectra of mixtures of **L1** (70 μM), Ag(I) sources (3.8 eq), and 0.0–1.5eq of pCp (500 MHz, $CDCl_3/(CD_3)_2CO$ = 75/1, 300 K). Ag(I) sources: a) $AgSbF_6$, b) $AgBF_4$, and c) $AgCF_3SO_3$.

Next, to examine the effect of the mode of arrangement of Ag(I) ions within the cyclic framework of **L1**, control experiment using a *half*-macrocycle [Ag**L2**(Et_2O)]SbF_6, which has a partial structure of $[Ag_2\mathbf{L1}X_2](SbF_6)_2$, as a host was performed in $CDCl_3/(CD_3)_2CO$ at 300 K (Figure 2–31–32) (preparation and characterization of [Ag**L2**(Et_2O)]SbF_6 are described in Chapter 3). Upon adding pCp to a solution of [Ag**L2**(Et_2O)]SbF_6, gradual shifting of the signals of [Ag**L2**(Et_2O)]SbF_6 was observed, suggesting significant host-guest interactions (Figure 2–31). Distinct from the case of the dinuclear Ag(I)-macrocycle, the intermolecular exchange reaction of pCp was faster than the timescale of ^{1}H NMR, because the signals gradually shifted as the amount of pCp increased. The formation of a 1:1 complex pCp⊂[Ag**L2**]$^+$ in solution was suggested from ESI-TOF mass measurement (*m*/*z* = 847.15 for pCp⊂[Ag**L2**]$^+$) (Figure 2–33). Moreover, binding of pCp by the half-macrocycle via Ag–π interactions was suggested by single crystal X-ray analysis (Figure 2–34). Upon slow evaporation of a mixture of **L2**, $AgSbF_6$ (1.5 eq), and pCp (2.0 eq) in $CDCl_3$, yellow block crystals were obtained. In the resulting crystal structure, one molecule of pCp is bound by two [Ag**L2**]$^+$ from top and bottom via η^2-type Ag–π interactions (Ag–C41 2.371(14) Å; Ag–C42 2.434(14) Å, Figure 2–34). Based on these results,

the binding constants for 1:1 complexation (K'_{a1}(pCp) = [pCp⊂[Ag**L2**]$^+$]/([pCp][[Ag**L2**(Et$_2$O)]$^+$]) M^{-1}) and 1:2 complexation (K'_{a2}(pCp) = [pCp⊂[Ag**L2**]$_2^{2+}$]/([pCp⊂[Ag**L2**]$^+$][[Ag**L2**(Et$_2$O)]$^+$]) M^{-1}) between pCp and [Ag**L2**(Et$_2$O)]SbF$_6$ were estimated to be K'_{a1}(pCp) = (1.9 ± 0.5) × 10^4 M^{-1} and K'_{a2}(pCp) = (1.0 ± 0.1) × 10^3 M^{-1}, respectively, in CDCl$_3$/(CD$_3$)$_2$CO at 300 K from the curve fitting of the ^{1}H NMR data of titration experiments (Figure 2–32). These values are quite smaller than that of the dinuclear Ag(I)-macrocycle [Ag$_2$**L1**X$_2$](SbF$_6$)$_2$ (K_a(pCp) > 10^9 M^{-1}).

In summary, above-mentioned results indicate the nano-space of the dinuclear Ag(I)-macrocycle [Ag$_2$**L1**X$_2$](SbF$_6$)$_2$, which is arranged with coordinatively labile sites of two Ag ions placed in about 9 Å apart from each other, can work as an effective binding site for ditopic aromatic hydrocarbons using multipoint Ag–π interactions. The high electron donation property of the π-plane of pCp should also have significant contribution to the stabilization of the resulting complex.[9]

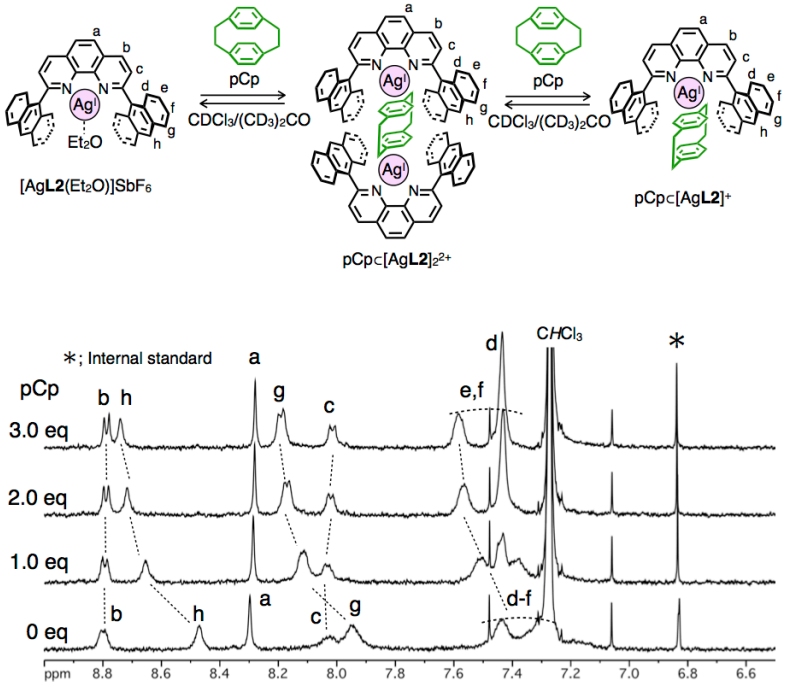

Figure 2–31. Partial ^{1}H NMR spectra of mixtures of [Ag**L2**(Et$_2$O)]SbF$_6$ (185 μM) and different amounts of pCp (500 MHz, CDCl$_3$/(CD$_3$)$_2$CO = 80/1, 300 K). An asterisk represents the signal of *p*-dimethoxybenzene used as the internal standard.

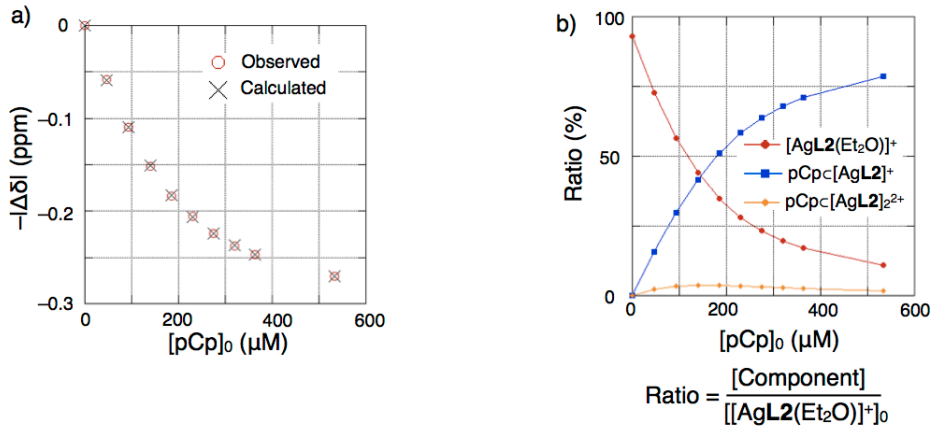

$$[\mathbf{AgL2}(Et_2O)]^+ + pCp \underset{}{\overset{K'_{a1}(pCp)}{\rightleftharpoons}} pCp\subset[\mathbf{AgL2}]^+$$

$$[\mathbf{AgL2}(Et_2O)]^+ + pCp\subset[\mathbf{AgL2}]^+ \overset{K'_{a2}(pCp)}{\rightleftharpoons} pCp\subset[\mathbf{AgL2}]_2^{2+}$$

$$K'_{a1}(pCp) = \frac{[pCp\subset[\mathbf{AgL2}]^+]}{[pCp][[\mathbf{AgL2}(Et_2O)]^+]} = (1.9 \pm 0.5) \times 10^4\ M^{-1}$$

$$K'_{a2}(pCp) = \frac{[pCp\subset[\mathbf{AgL2}]_2^{2+}]}{[pCp\subset[\mathbf{AgL2}]^+][[\mathbf{AgL2}(Et_2O)]^+]} = (1.0 \pm 0.1) \times 10^3\ M^{-1}$$

Figure 2–32. The stability constant analysis by a least square fitting to the ^{1}H NMR shift in Figure 2–31. a) Plots of the amounts of shift change of the ^{1}H NMR signals (H_h) against the concentrations of pCp (hollow circle: observed, cross marks: calculated), and b) the calculated component distribution of $[Ag\mathbf{L2}(Et_2O)]^+$, $pCp\subset[Ag\mathbf{L2}]^+$, and $pCp\subset[Ag\mathbf{L2}]_2^{2+}$. $[[Ag\mathbf{L2}(Et_2O)]^+]_0$ and $[pCp]_0$ indicate the initial concentration of $[Ag\mathbf{L2}(Et_2O)]^+$ and pCp.

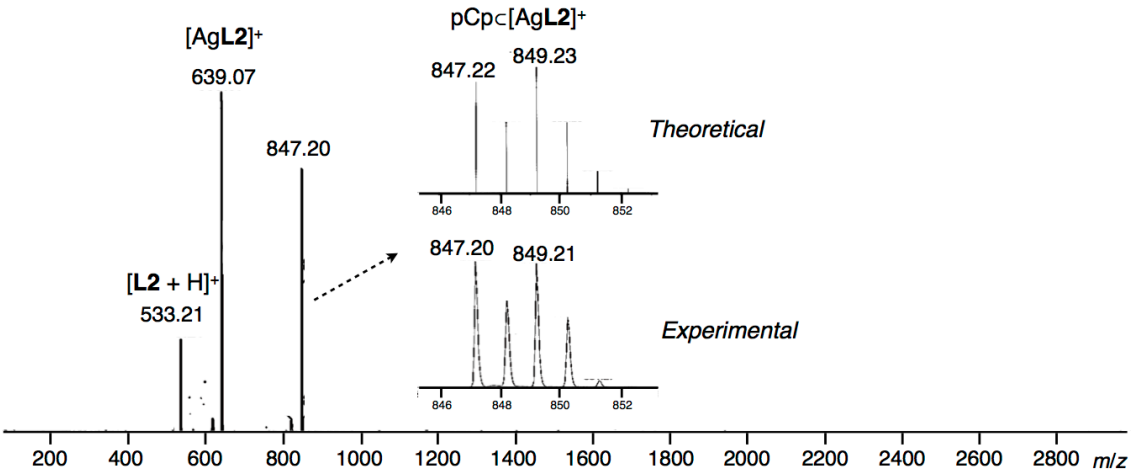

Figure 2–33. ESI-TOF mass spectrum of a mixture of $[Ag\mathbf{L2}(Et_2O)]SbF_6$ and pCp (1.0 eq) in $CHCl_3/(CH_3)_2CO$ = 80/1.

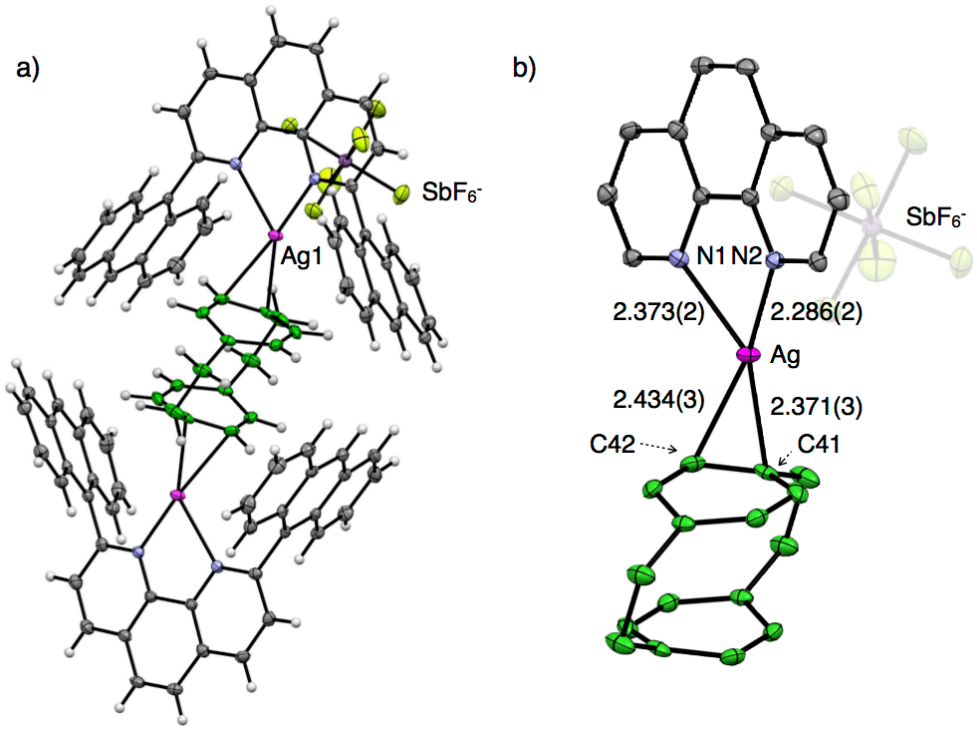

Figure 2–34. Crystal structures (ORTEP views (50% probability level)) of a) pCp⊂[Ag**L2**]$_2$(SbF_6)$_2$ and b) a partial structure (some parts of counter anions and H-atoms are omitted for clarity). (Ag: magenta, C: grey, C of pCp: green, F: yellow, H: white, N: blue, Sb: pink).

2–3–3. Binding of redox active organometallic molecules

Guest molecules included within a nano-space of host molecules can form or exhibit specific molecular structures or properties based on the chemical and physical characteristics of the inner surface of hosts. Particularly in the cases of metallo-macrocycles, included guest molecules can be greatly affected by the coordination characteristics of metal ions, which can be utilized for guest accommodation and activation leading to metal-based functions. In this section, I describe the incorporation ferrocene ($FeCp_2$) and its derivative into the nano-space of a dinuclear Ag(I)-macrocycle $[Ag_2\mathbf{L1}X_2](SbF_6)_2$ using Ag–π interactions. In the nano-space, a $FeCp_2$ molecule was expected to form a Ag–π–Fe–π–Ag arrangement which is significantly stabilized by the confined space of the macrocyclic framework. Furthermore, the cationic nature of Ag–π complexation seems to affect the redox reactivity of included $FeCp_2$ in the nano-cavity.

Binding of ferrocene within Ag(I)-macrocycle

Binding behaviors of ferrocene ($FeCp_2$) within the nano-space of Ag(I)-macrocycle were investigated by ^{1}H NMR titration experiment (Figure 2–35,37). Upon adding $FeCp_2$ to a solution of $[Ag_2\mathbf{L1}X_2](SbF_6)_2$ in $CDCl_3$ (107 μM) at 300 K, the host's signals were gradually shifted suggesting host-guest interaction. As the host-guest binding was reversible and the intermolecular exchange reaction of $FeCp_2$ was faster than the ^{1}H NMR timescale, titration experiment was reinvestigated at lower temperature (220 K) so as to further characterize the host-guest interaction in detail (Figure 2–36). At 220 K, the signal of $[Ag_2\mathbf{L1}X_2](SbF_6)_2$ was gradually replaced by a new set of signals with an increase in the amount of $FeCp_2$ (Figure 2–36b). The signals were almost completely replaced by the new set of signals in the presence of more than 1.0 eq of $FeCp_2$, which suggests the formation of a 1:1 host-guest complex, $FeCp_2\subset[Ag_2\mathbf{L1}](SbF_6)_2$ (Figure 2–36c). A new singlet signal (A_{in} in Figure 2–36c) appeared around 1.8 ppm can be assigned as that of each Cp ring of included $FeCp_2$. This exhibited a strong ROE correlation with the proton signals inside the nano-space (H_i) (Figure 2–38). This signal was highly upfield shifted due to the strong shielding effect from anthracene walls ($\Delta\delta$ = –2.4 ppm). ESI-TOF mass measurement supported the formation of a 1:1 inclusion complex (m/z = 907.08 as $FeCp_2\subset[Ag_2\mathbf{L1}]^{2+}$) (Figure 2–39). From the curve fitting of the amount of shifts of the ^{1}H NMR signals on Figure 2–35, the binding constant of the host-guest complexation ($K_a(FeCp_2)$ = $[FeCp_2\subset[Ag_2\mathbf{L1}]^{2+}]/([FeCp_2][[Ag_2\mathbf{L1}]^{2+}])$ M^{-1}) at 300 K in $CDCl_3$ was determined to be $K_a(FeCp_2) = (6.2 \pm 0.9) \times 10^4$ M^{-1} in $CDCl_3$ at 300 K (Figure 2–37).

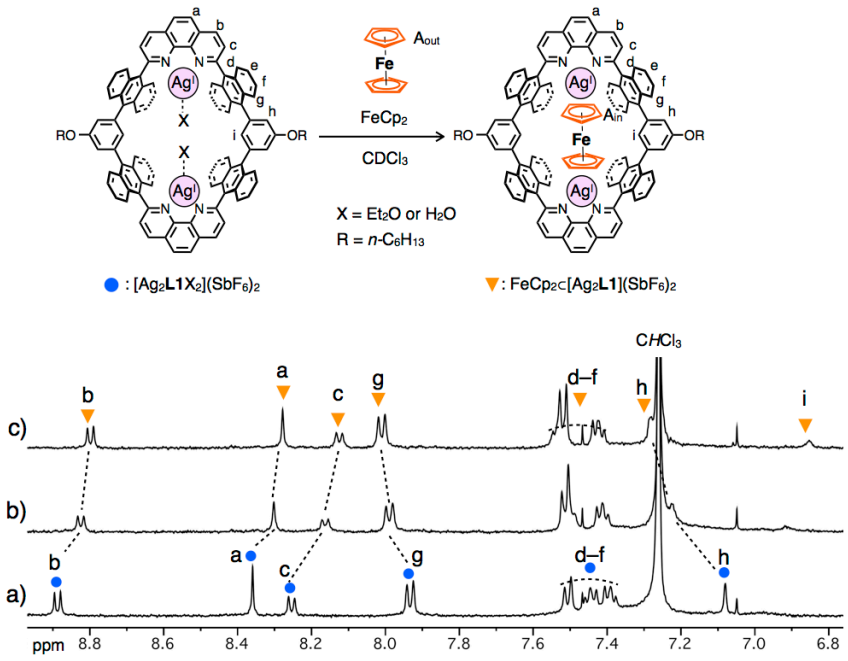

Figure 2–35. Partial ^{1}H NMR spectra of mixtures of $[Ag_2\mathbf{L1}X_2](SbF_6)_2$ (107 μM) in the presence of a) 0.0, b) 1.0, and c) 5.0 eq of $FeCp_2$ (500 MHz, $CDCl_3$, 300 K).

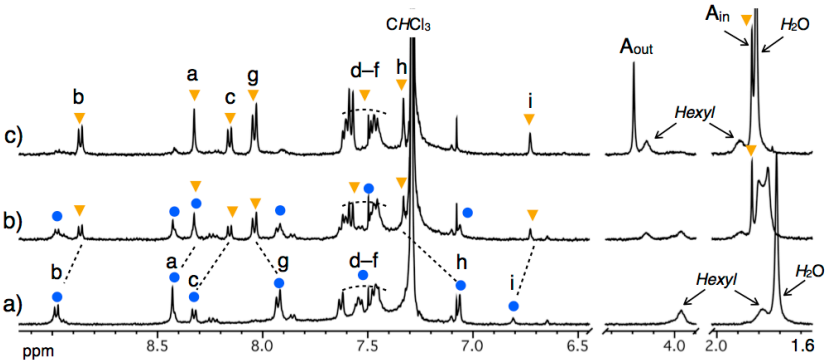

Figure 2–36. Partial ^{1}H NMR spectra of mixtures of $[Ag_2\mathbf{L1}X_2](SbF_6)_2$ (80 μM) in the presence of a) 0.0, b) 0.5, and c) 1.5 eq of $FeCp_2$ (500 MHz, $CDCl_3$, 220 K).

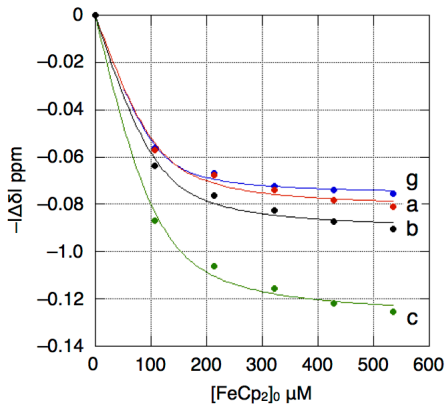

$$K_a(FeCp_2) = \frac{[FeCp_2\subset[Ag_2\mathbf{L1}]^{2+}]}{[FeCp_2]\,[[Ag_2\mathbf{L1}X_2]^{2+}]}$$

$$= (6.2 \pm 0.9) \times 10^4\ M^{-1}$$

in $CDCl_3$ at 300 K

Figure 2–37. Stability constant analysis by the least square fitting to the shifts of NMR signals ($H_{a–c,g}$) in the titration experiment described in Figure 2–35 (solid circles: observed, lines: calculated). $[FeCp_2]_0$ indicates the initial concentration of $FeCp_2$.

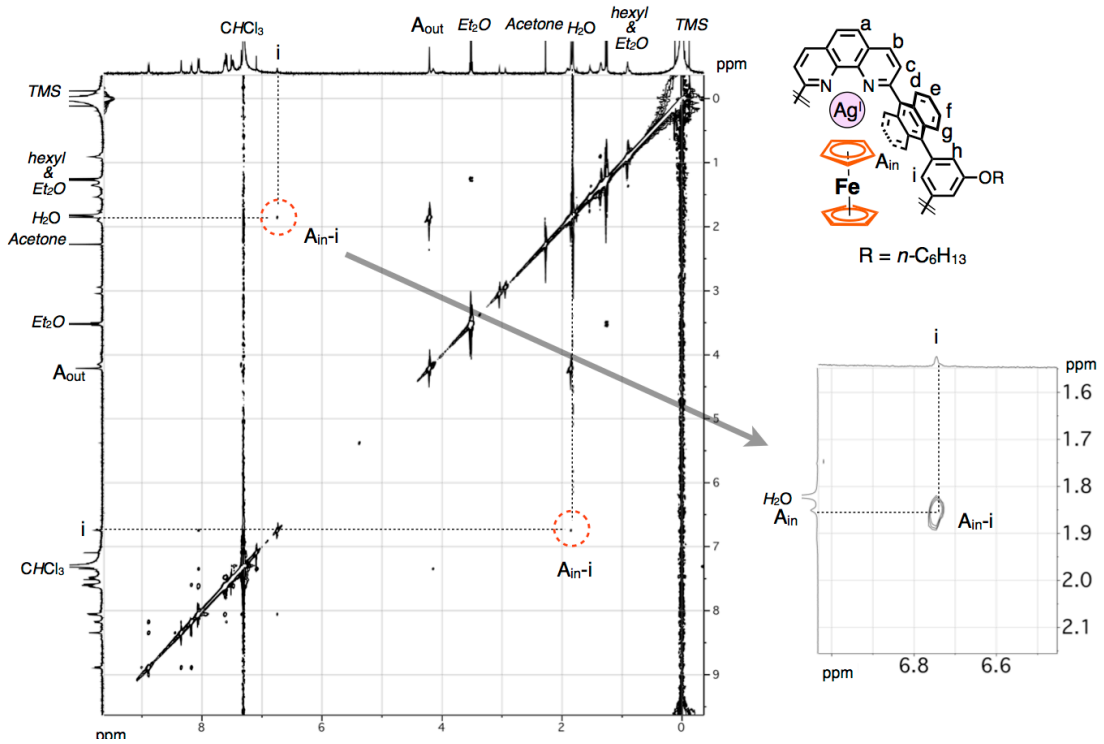

Figure 2–38. ^{1}H-^{1}H ROESY spectrum of a mixture of $[Ag_2\mathbf{L1}X_2](SbF_6)_2$ (80 μM) and $FeCp_2$ (1.5 eq) (500 MHz, $CDCl_3$, 220 K).

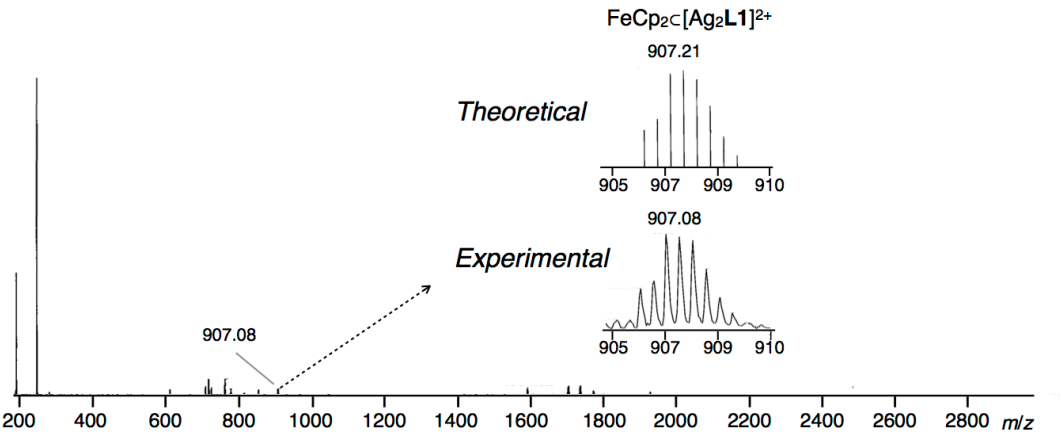

Figure 2–39. ESI-TOF mass spectrum of a mixture of $[Ag_2\mathbf{L1}X_2](SbF_6)_2$ and $FeCp_2$ (5.0 eq) in $CDCl_3$.

As in the case of $FeCp_2$, host-guest interactions between hydroxymethyl ferrocene ($FeCp_2$') and $[Ag_2\mathbf{L1}X_2](SbF_6)_2$ were suggested from the shifts of the ^{1}H NMR signals and ESI-TOF mass spectrometry (m/z = 922.26 as $FeCp_2$'$\subset[Ag_2\mathbf{L1}]^{2+}$) (Figure 2–40–41). Even in the presence of C_s-symmetrical guest within its nano-space, the signals' pattern of the resulting complex was the same as that of the original D_{2h}-symmetrical Ag(I)-macrocycle, which may be due to the fast intermolecular guest exchange or fluxional oscillation motion of the guest within the nano-space.

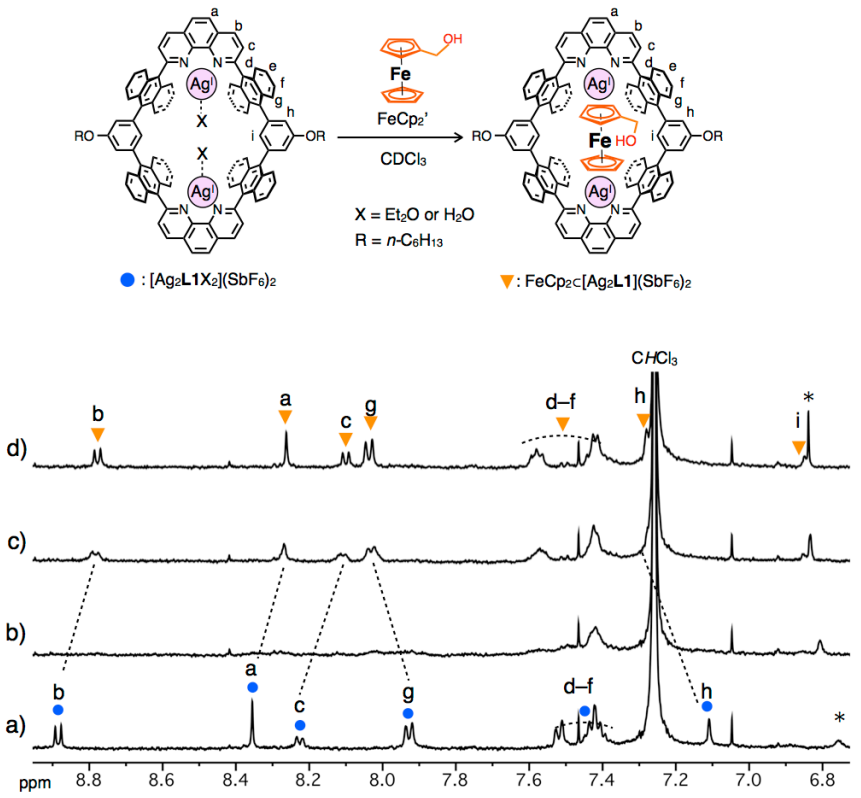

Figure 2–40. Partial ^{1}H NMR spectra of $[Ag_2\mathbf{L1}X_2](SbF_6)_2$ (60 μM) in the presence of a) 0.0, b) 0.5, c) 1.0 and d) 2.0 eq of $FeCp_2$' (500 MHz, $CDCl_3$, 300 K). An asterisk represents the signal of *p*-dimethoxybenzene used as the internal standard.

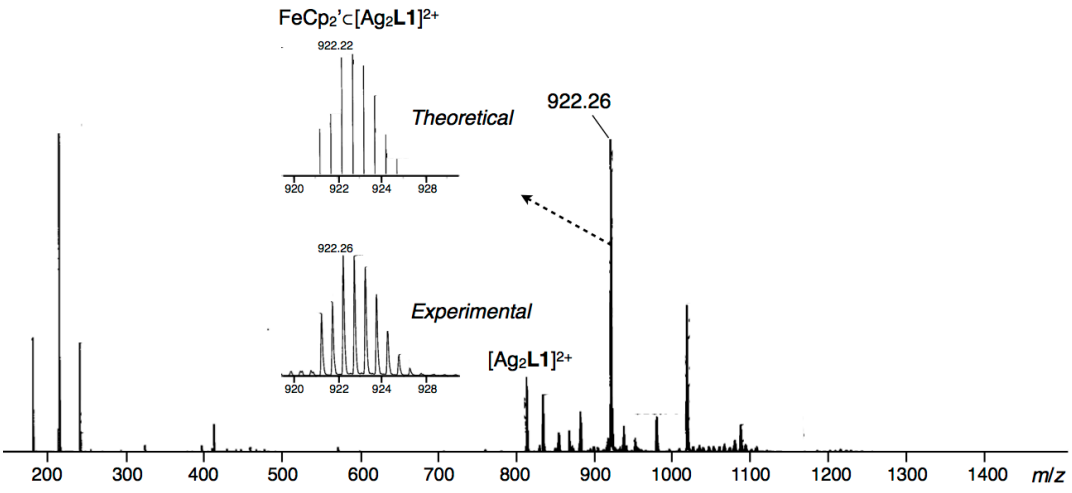

Figure 2–41. ESI-TOF mass spectrum of the mixture of $[Ag_2\mathbf{L1}X_2](SbF_6)_2$ and $FeCp_2$' (2.0 eq) in $CDCl_3$.

The molecular structure of $FeCp_2'\subset[Ag_2\mathbf{L1}](SbF_6)_2$ was determined by single crystal X-ray analysis. Upon *n*-pentane vapor diffusion into a mixture of $[Ag_2\mathbf{L1}X_2](SbF_6)_2$ and 20 eq of $FeCp_2$' in $CHCl_3$, yellow block crystals suitable for single crystal X-ray analysis were obtained.

In the resulting crystal structure, one molecule of $FeCp_2$' was included within the nano-space of the dinuclear Ag(I)-macrocycle in a substitutionary disordering manner (Figure 2–42). Ag(I) ions within the nano-space are crystallographycally equivalent and form a distorted tetrahedral coordination geometry with two N-atoms of phenanthroline and two C-atoms of $FeCp_2$' (Ag–N1 2.29(1) Å; Ag–N2 2.29(1) Å; Ag–C2P 2.49(2) Å; Ag–C3P 2.52(3) Å, Figure 2–42c). The distance between two Ag(I) ions within the nano-space is 9.27(0) Å, which is approximately identical to those of the original dinuclear Ag(I)-macrocycle (Ag–Ag distances of $[Ag_2\mathbf{L1}X_2](SbF_6)_2$: 9.433(1)–9.181(1) Å). Each Ag(I) ion forms an η^2-type Ag–π interaction with a π-plane of each Cp ring with a hydroxymethyl moiety of disordering $FeCp_2$'. Distinct from the case of the pCp inclusion complex (pCp⊂$[Ag_2\mathbf{L1}](SbF_6)_2$), Ag–π interactions are not detected in another π-plane of $FeCp_2$'; the Ag–π distance is about 3.3 Å, which is longer than the sum of the van der Waals radii of Ag and C atoms. According to previously reported Ag–π complexes of ferrocene derivatives,[10] Ag–π interactions with the Cp rings of $FeCp_2$ derivatives appear to be weaker than those of the ordinal aromatic hydrocarbons based on their longer Ag–C bond length. Such a week affinity between Ag(I) and Cp rings may possibly give rise to the difference in the multiplicity of Ag–π interactions in the case of $FeCp_2$'⊂$[Ag_2\mathbf{L1}](SbF_6)_2$ in the crystalline state. However, considering that the position of the π-planes of $FeCp_2$', which are close to Ag(I) ions, and high symmetrical ^{1}H NMR signals of the inclusion complex of pristine $FeCp_2$ in $CDCl_3$ observed at low temperature (220 K) (Figure 2–36c on page 51), Ag–π interaction should be formed at both sides of the aromatic rings of $FeCp_2$ derivatives in solution, leading to guest binding. Besides the Ag–π interaction, $FeCp_2$' within the nano-space formed multipoint CH–π interactions with anthracene walls (C–π distance: ca. 3.1 Å), which was also supposed to contribute to the stabilization of the host-guest complex (Figure 2–42a).

In the case of the inclusion complex of pristine $FeCp_2$, yellow brock crystals suitable for single crystal X-ray analysis were obtained in the same way as $FeCp_2$', although the $FeCp_2$ within the nano-space could not be assigned probably due to severe disordering of the included molecule. However, similar ^{1}H NMR shifts observed in the titration experiment between $[Ag_2\mathbf{L1}X_2](SbF_6)_2$ and $FeCp_2$ or $FeCp_2$' (Figure 2–35 and Figure 2–40) suggest that Ag–π interactions between π-planes of $FeCp_2$ and Ag(I) centers of $[Ag_2\mathbf{L1}]^{2+}$ work as a driving force to form host-guest complex.

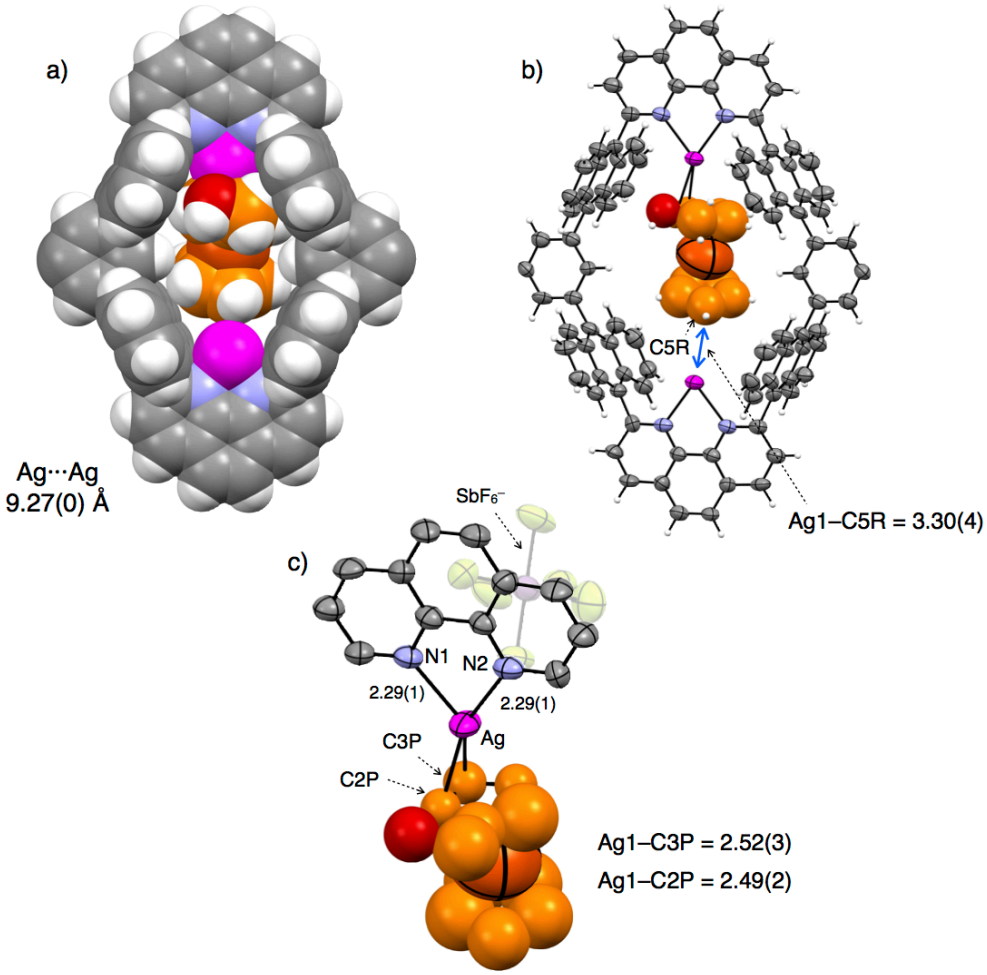

Figure 2–42. Crystal structures of $FeCp_2$'⊂$[Ag_2$**L1**$](SbF_6)_2$. a) Space filling model, b) ORTEP view (50% probability level), and c) ORTEP view of a partial structure (one of the disordering pattern of $FeCp_2$' (occupancy: 50%), some parts of solvent, side-alkyl chains, counter anions, and H-atoms are omitted for clarity). (Ag: magenta, C: grey, C of $FeCp_2$': orange, F: yellow, H: white, N: blue, O: red, Sb: pink).

Redox reactivity of Ag–π complex of ferrocene within dinuclear Ag(I)-macrocycle

The resulting Ag–π complex of $FeCp_2$ ($FeCp_2$⊂$[Ag_2$**L1**$](SbF_6)_2$) exhibited the following two types of specific redox reactivities.

Firstly, the oxidation states of Ag(I) ions were found to be stabilized by the electron donation effect of the phenanthrolines of macrocyclic ligand **L1**. Originally, the synthesis of Ag–π complex of $FeCp_2$ was thought to be difficult, because the combination of Ag(I) and $FeCp_2$ normally causes an irreversible redox reaction (Ag^+/Ag: 0.65 V vs Fc in CH_2Cl_2), that is reduction of Ag(I) to form insoluble Ag(0).[11] Indeed, upon mixing $AgSbF_6$ and $FeCp_2$ in $CDCl_3$/$(CD_3)_2CO$, a dark green precipitate was rapidly formed due to a redox reaction between solvated Ag(I) and $FeCp_2$ to form insoluble Ag(0) and a ferrocenium salt (Figure 2–43a). On the other hand, when $FeCp_2$ was added to a solution of $[Ag_2$**L1**$X_2](SbF_6)_2$, neither color changes nor

precipitation were observed (Figure 2–43b). This means no redox reactions took place between added $FeCp_2$ and Ag(I) bound to the macrocyclic skeleton, which was also supported by the diamagnetic behavior of a mixture of Ag(I)-macrocycle and $FeCp_2$ in the ^1H NMR measurement (Figure 2–35 on page 51). Indeed, the cyclic voltammograms of $AgSbF_6$ in CH_2Cl_2 containing 0.1 M $TBAPF_6$ showed one set of irreversible reduction and oxidation current peaks around 0.30 and 0.65 V (vs Ag^+/Ag), respectively, which can be assigned as reduction of solvated Ag(I) ions and subsequent oxidation of Ag(0) absorbed on the surface of electrode (Figure 2–43c, red). On the other hand, in the case of $[Ag_2\mathbf{L1}X_2](SbF_6)_2$, the cyclic voltammograms under the same condition showed no prominent current peak as the reduction potential of Ag(I) was shifted to a more negative region (Figure 2–43c, blue). This suggests that Ag(I) ions arranged within inner surface of **L1** are stabilized due to the coordination by the phenanthrolines as an effective electron donor.[12] These results suggest that macrocyclic ligand **L1** can work as an effective template to prepare a stable Ag–π complex of $FeCp_2$.

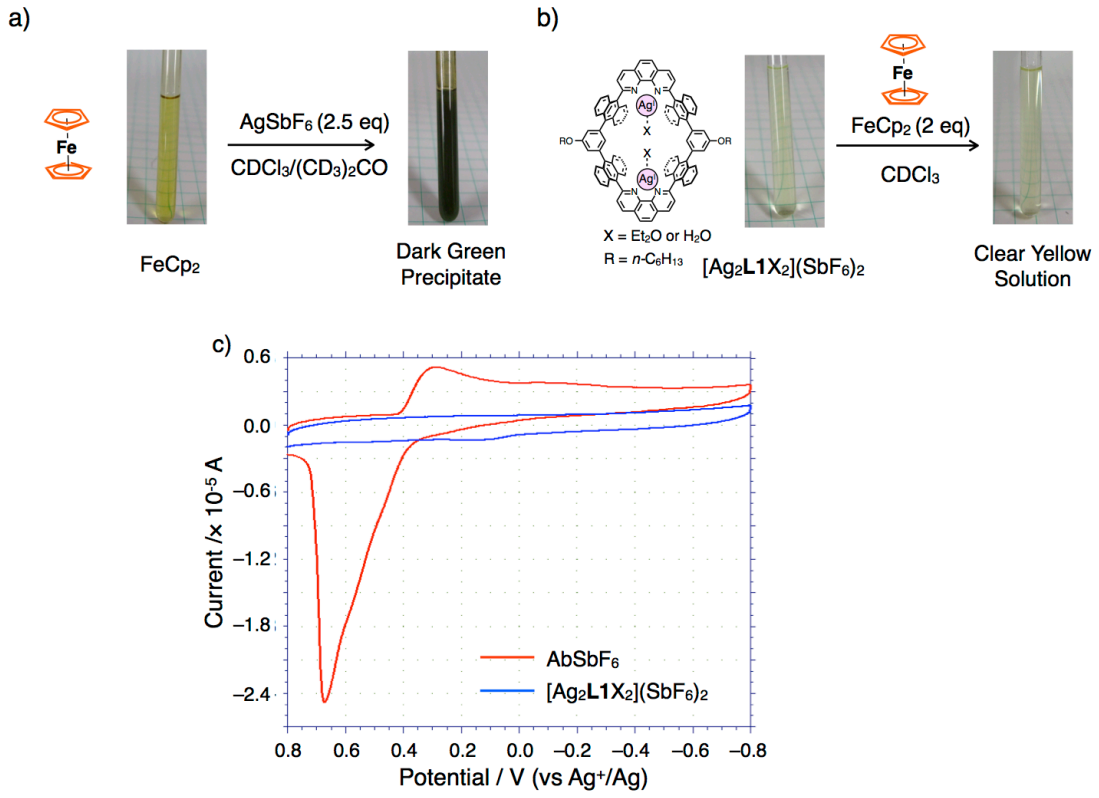

Figure 2–43. Appearances of a) a solution of $FeCp_2$ in $CDCl_3/(CD_3)_2CO$ before and after addition of $AgSbF_6$, b) a solution of $[Ag_2\mathbf{L1}X_2](SbF_6)_2$ in $CDCl_3$ before and after addition of $FeCp_2$, c) cyclic voltammograms of solutions of $AgSbF_6$ (430 μM) and $[Ag_2\mathbf{L1}X_2](SbF_6)_2$ (430 μM) in CH_2Cl_2 containing 0.1 M $TBAPF_6$ at 291 K. Scan late: 100 mVs^{-1}.

Secondly, the oxidation state of $FeCp_2$ included within the nano-space of Ag(I)-macrocycle was affected by the cationic character of Ag(I) ions, as observed in the cyclic voltammetry (Figure 2–44). When 15 eq of isolated crystals of $[Ag_2\mathbf{L1}X_2](SbF_6)_2$ were dissolved in a solution of $FeCp_2$ in CH_2Cl_2 containing 0.1 M $TBAPF_6$ at 291 K, a substantial decrease in the redox current peaks was observed, suggesting decrease in the diffusivity and in the rate of heterogeneous electron transfer reaction of $FeCp_2$ upon host-guest complexation. Besides, the reversible redox current peaks of $FeCp_2$ showed a significant anodic shift (ca. +70 mV). This means that the reduced form of $FeCp_2$ in the dinuclear Ag(I)-macrocycle was stabilized by the cationic character of the neighboring Ag(I) ions.[13] These results suggest that the nano-space of the dinuclear Ag(I)-macrocycle have potential to modify reactivity or electronic properties of aromatic guest molecules.

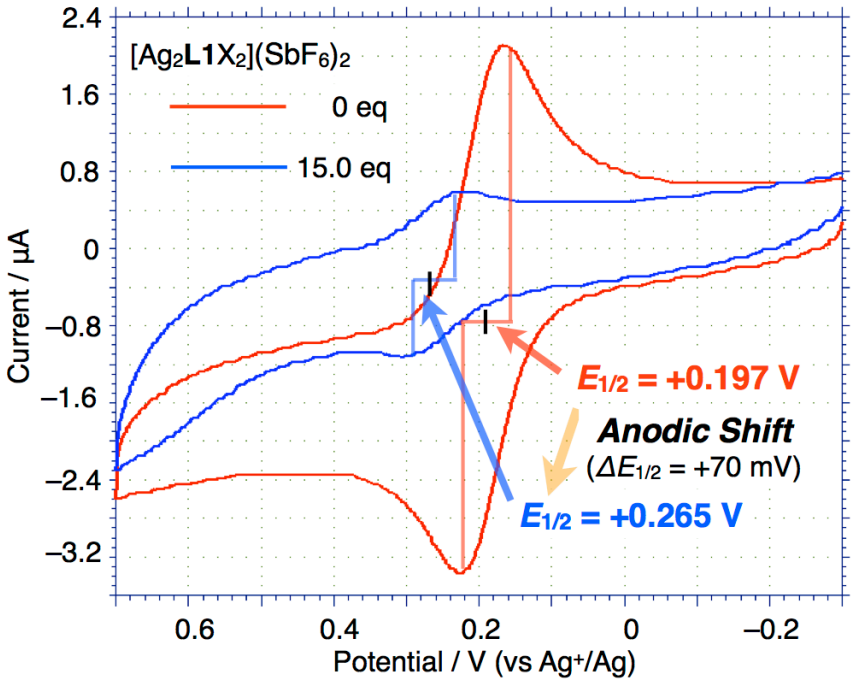

Figure 2–44. Cyclic voltammograms of mixtures of $FeCp_2$ (200 μM) and different amounts of $[Ag_2\mathbf{L1}X_2](SbF_6)_2$ in CH_2Cl_2 containing 0.1 M $TBAPF_6$ at 291 K. Scan rate; 50 mVs^{-1}.

2–4. Conclusion

In order to develop novel motifs of host compounds to include aromatic guest molecules, a dinuclear Ag(I)-macrocycle $[Ag_2\mathbf{L1}X_2](SbF_6)_2$ possessing two Ag(I) ions on its framework has been newly prepared, and its host-guest complexation behaviors with aromatic guest molecules were investigated (Figure 2–45). $[Ag_2\mathbf{L1}X_2](SbF_6)_2$ provides a nano-space arranged with coordinatively labile sites of two Ag(I) ions. Taking advantage of Ag–π interaction as a driving force, $[Ag_2\mathbf{L1}X_2](SbF_6)_2$ and its $CF_3SO_3^-$ salt can include several kinds of aromatic molecules like *p*-xylene, anthracene, [2.2]paracyclophane (pCp), and ferrocene ($FeCp_2$) derivatives in solution and/or in the solid state. In particular, the affinities of $[Ag_2\mathbf{L1}X_2](SbF_6)_2$ to aromatic molecules like anthracene, pCp, and $FeCp_2$ derivatives are so strong that the binding constants of the host-guest complexations are as large as $K_a = 10^4$–10^9 M^{-1} in $CDCl_3$ at 300 K. In these cases, guest molecules can create Ag–π interactions at both sides of Ag(I) ions on the nano-space in a multipoint manner. Multipoint Ag–π interactions lead to such strong host-guest interactions as revealed by comparisons of crystal structures of the resulting complexes and control experiments using model compounds. Moreover, electrochemical measurements revealed that the redox reactivity of included $FeCp_2$ within the nano-space of $[Ag_2\mathbf{L1}]^{2+}$ was markedly changed due to the cationic character of the neighboring Ag(I) ions.

In this work, I found that multipoint Ag–π interactions within the nano-space of a dinuclear Ag(I)-macrocycle work as useful driving forces for binding aromatic guest molecules. Moreover, the dinuclear Ag(I)-macrocycle has great potential to modify electronic properties and reactivity of included aromatic molecules. Such metallo-macrocycles would provide novel functions such as guest separation and activation taking advantage of specific coordination properties of well-arranged *non*-Werner type coordination centers.

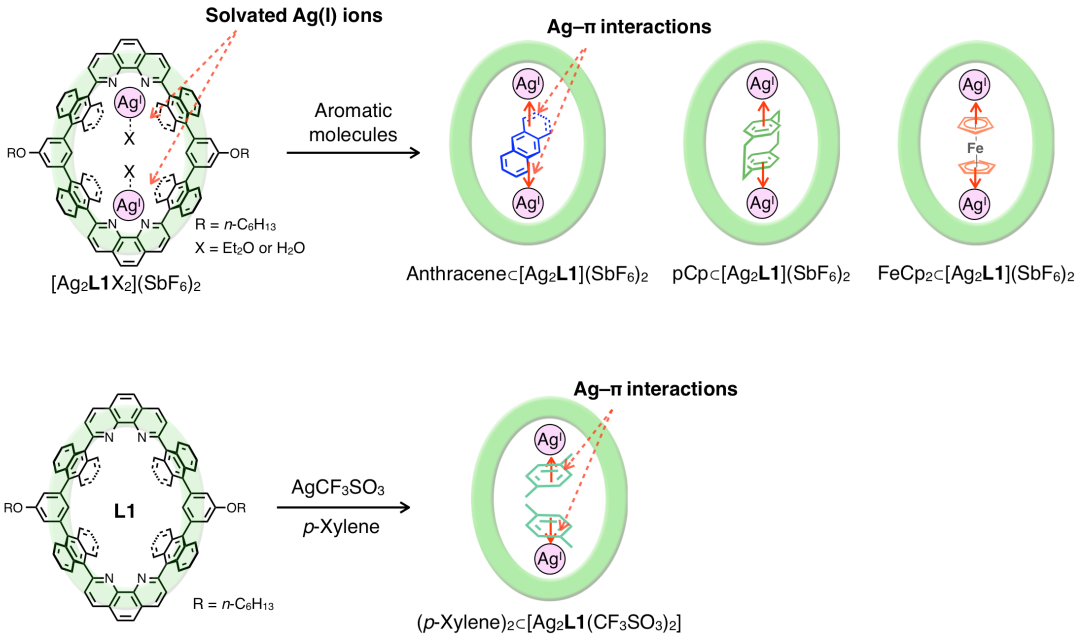

Figure 2–45. Host-guest complexation between a dinuclear Ag(I)-macrocycle $[Ag_2\mathbf{L1}X_2](SbF_6)_2$ or its $CF_3SO_3^-$ salt with aromatic molecules via Ag–π interactions.

2–5. Experimental

Materials and methods

All solvents, organic, and inorganic reagents are commercially available, and were used without further purification. $Pd(PPh_3)_4$ was synthesized according to the literature.[14] Silica gel column chromatography was performed using Merck Silica Gel 60 (230–400 mesh). 9,10-Bis(4,4,5,5-tetramethyl-1,3,2-dioxaborolan-2-yl)anthracene (**3**),[15] 2,9-Dichloro-1,10-phenanthroline (**4**),[6a] and 1,3-dibromo-5-(hexyloxy)benzene (**5**)[6a] were synthesized according to previously reported procedures.

NMR spectroscopic measurements were performed using Bruker DRX-500 (500 MHz for ^1H), Bruker AVANCE 500 (500 MHz for ^1H; 126 MHz for ^{13}C), and JEOL AL-400 (400 MHz for ^1H) spectrometers. NMR spectra were calibrated as below; tetramethylsilane ($Si(CH_3)_4$) = 0 ppm for ^1H, $CDCl_3$ = 77.16 ppm for ^{13}C. *p*-Dimethoxybenzene was added as the internal standard for the calibration of the concentration of samples. ESI-TOF mass spectra were recorded on a Micromass LCT spectrometer. Melting points were measured using a Yanaco MP-500D apparatus. GPC was performed on a recycling preparative HPLC (Japan Analytical Industry; LC-928) with a JAIGEL-2H-40 column. Single-crystal X-ray crystallographic analyses were performed using a Rigaku RAXIS-RAPID imaging plate diffractometer with MoKα radiation, and the obtained data were analyzed using a CrystalStructure crystallographic software package except for refinement, which were performed using SHELXL-97 and SHELXL-2013 programs.[16] Electrochemical measurements were recorded with an ALS 630A electrochemical analyzer (BAS. Co., Ltd.). The working electrode was a 3 mm glassy carbon electrode; a platinum wire served as the auxiliary electrode, and the reference electrode was an Ag^+/Ag electrode (a silver wire immersed in 0.1 M $TBAClO_4$/0.01 M $AgNO_3$ in CH_3CN). The solution was deoxygenated with pure nitrogen prior to the electrochemical measurements.

Synthesis of macrocyclic ligand L1

Scheme 2–4. Synthetic route for macrocyclic ligand **L1**

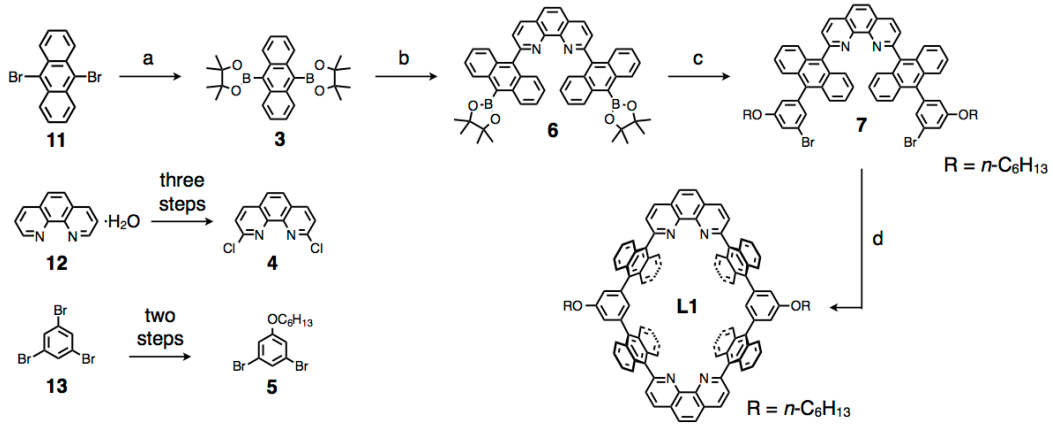

Reagents and conditions: (a) (i) *n*-BuLi, THF, –78 °C, (ii) $B(OEt)_3$, THF, –78 °C, (iii) HCl aq., rt, (iv) pinacol, Na_2SO_4, CH_3COOH, THF, rt (40%); (b) **4**, $Pd(PPh_3)_4$, K_3PO_4, DMF, 100 °C (33%); (c) **5**, $Pd(PPh_3)_4$, K_3PO_4, DMF, 100 °C (45%); (d) **6**, $Pd(PPh_3)_4$, K_3PO_4, DMF, 100 °C (5%).

9,10-Bis(4,4,5,5-tetramethyl-1,3,2-dioxaborolan-2-yl)anthracene (3): Compound **3** was synthesized by a modified procedure of the literature.[15] 9,10-Dibromoanthracene (**11**) (7.52 g, 22.4 mmol, 1.0 eq) was placed in a three-neck flask (500 mL) and dried under reduced pressure. The inner gas was replaced by argon, and anhydrous THF (300 mL) was added to the flask. After cooling down to –78 °C, a solution of *n*-BuLi in *n*-hexane (1.6 M, 45 mL, 72 mmol, 3.2 eq) was added dropwise to the mixture over 30 min. The reaction mixture was stirred for 2 h, to which was added $B(OEt)_3$ (12.5 mL, 74 mmol, 3.3 eq) dropwise over 10 min, and further stirred for 19 h. The mixture was quenched with 2.0 M HCl aq. (150 mL), stirred for 4 h at room temperature, and extracted with diethyl ether (150 mL × 3). The combined organic layer was dried over Na_2SO_4 and evaporated under reduced pressure to yield a yellow oil. To the mixture was added CH_2Cl_2 (300 mL), and the resulting colorless precipitate was collected by filtration, washed by CH_2Cl_2, and dried under reduced pressure to afford a colorless solid (2.42 g). From the filtrate left for half a day, colorless precipitate (656 mg) was further obtained. The combined boronic acid was used for the next reaction without further purification. The boronic acid (3.08 g, 11.5 mmol, 1.0 eq, calculated as a pure compound), pinacol (4.31 g, 36.5 mmol, 3.2 eq), and Na_2SO_4 (4.10 g, 28.9 mmol, 2.5 eq) were placed in a flask. To the mixture were added anhydrous THF (50 mL) and a catalytic amount of CH_3COOH (0.3 mL). After stirring the reaction mixture at room temperature for 2 days, the mixture was filtered to obtain a pale yellow solution. After evaporation under reduced pressure, the residue was dissolved in CH_2Cl_2 (200

mL), and filtered off the resulting insoluble matter. The filtrate was evaporated under reduced pressure to obtain a colorless solid (5.56 g). The solid was washed with hot *n*-hexane (50 mL), and then dried under reduced pressure to afford **3** as a colorless solid (3.86 g, 8.97 mmol, 40%).

^{1}H NMR (400 MHz, $CDCl_3$, 293 K): δ (ppm) = 8.33 (dd, J = 6.8, 3.3 Hz, 4H, Ar*H*), 7.44 (dd, J = 6.8, 3.3 Hz, 4H, Ar*H*), 1.58 (s, 24H, CH_3).

^{13}C NMR (126 MHz, $CDCl_3$, 300 K): δ (ppm) = 134.9, 128.8, 125.1, 84.5, 25.2 (the signal of the aromatic quaternary carbon next to the boron atom was not observed due to the quadrupole moment of boron).

M.p.: 325–328 °C

IR (ATR): R (cm^{-1}) = 2978, 2360, 2341, 1311, 1239, 1134, 979, 851, 756.

Compound 6: Compounds **3** (6.43 g, 15.0 mmol. 3.0 eq), **4** (1.23 g, 4.95 mmol, 1.0 eq), K_3PO_4 (3.76 g, 17.7 mmol, 3.5 eq), and $Pd(PPh_3)_4$ (573 mg, 0.50 mmol, 0.1 eq) were placed in a dried three-neck flask. The inner gas was replaced by argon. Anhydrous DMF (70 mL) was added to the mixture, which was degassed by a freeze-pump-thaw procedure. The mixture was stirred at 100 °C for 9.5 h. During the reaction, additional $Pd(PPh_3)_4$ was added to the reaction mixture several times (total amount of additional $Pd(PPh_3)_4$: 386 mg, 0.327 mmol, 0.062 eq). After cooling down to room temperature, water (150 mL) was added to the mixture, which was extracted with CH_2Cl_2 (ca. 100 mL × 5). The combined organic layer was dried over Na_2SO_4, and then evaporated under reduced pressure at 80 °C to obtain a yellowish brown solid (3.20 g). The crude product was purified by column chromatography (SiO_2, ϕ = 8.0 cm, h = 10.0 cm, $CHCl_3$), and GPC ($CHCl_3$) to afford **6** (1.27 g, 1.61 mmol, 33%) as a yellow solid.

^{1}H NMR (500 MHz, $CDCl_3$, 300 K): δ (ppm) = 8.46 (d, J = 8.5 Hz, 2H, Ar*H*), 8.35 (d, J = 9.0 Hz, 4H, Ar*H*), 8.06 (s, 2H, Ar*H*), 7.77 (d, J = 8.5 Hz, 4H, Ar*H*), 7.77 (d, J = 8.0 Hz, 2H, Ar*H*), 7.39–7.36 (m, 4H, Ar*H*), 7.26–7.23 (m, 4H, Ar*H*), 1.55 (s, 24H, CH_3).

^{13}C NMR (126 MHz, $CDCl_3$, 300 K): δ (ppm) = 159.1, 146.7, 138.0, 135.8, 135.5, 129.8, 128.4, 127.9, 127.2, 127.0, 126.8, 125.2, 125.0, 84.4, 25.2 (the signal of the aromatic quaternary carbon next to the boron atom was not observed due to the quadrupole moment of boron).

HRMS (ESI): calcd. for $[C_{52}H_{46}B_2N_2O_4 + H]^+$: m/z = 785.3739, found m/z = 785.3735.

M.p.: 370–371 °C

IR (ATR): R (cm^{-1}) = 2976, 2359, 2342, 1310, 1238, 1136, 978, 849, 789.

Compound 7: Compounds **5** (5.76 g 17.1 mmol, 5.1 eq), **6** (2.61 g, 3.33 mmol, 1.0 eq), K_3PO_4 (4.22 g, 19.9 mmol, 6.0 eq), and $Pd(PPh_3)_4$ (569 mg, 0.49 mmol, 0.15 eq) were placed in a dried three-neck flask. The inner gas was replaced by argon. Anhydrous DMF (100 mL) was added to

the mixture, which was then degassed by a freeze-pump-thaw procedure. The mixture was stirred at 100 °C for 32 h. During the reaction, $Pd(PPh_3)_4$ was added several times (total amount of additional $Pd(PPh_3)_4$: 449 mg, 0.39 mmol, 0.11 eq). After cooling down to room temperature, water (300 mL) was added to the mixture, which was extracted with CH_2Cl_2 (ca. 200 mL × 4). The combined organic layer was dried over Na_2SO_4, and then evaporated under reduced pressure at 80 °C to obtain a yellowish brown solid (8.92 g). The crude product was purified by column chromatography (SiO_2, ϕ = 10.0 cm, h = 10.0 cm, $CHCl_3$/*n*-hexane = 9/10) to afford **7** (1.57 g, 1.51 mmol, 45%) as a yellowish solid.

^{1}H NMR (500 MHz, $CDCl_3$, 300 K): δ (ppm) = 8.54 (d, J = 8.0 Hz, 2H, Ar*H*), 8.11 (s, 2H, Ar*H*), 7.92 (d, 2H, Ar*H*), 7.79–7.77 (m, 4H, Ar*H*), 7.62–7.60 (m, 4H, Ar*H*), 7.26–7.28 (m, 8H, Ar*H*), 7.20–7.21 (m, 3H, Ar*H*), 7.02 (s, 1H, Ar*H*), 6.94 (s, 1H, Ar*H*), 6.77 (s, 1H, Ar*H*), 3.99–3.91 (m, 4H, CH_2), 1.82–1.71 (m, 4H, CH_2), 1.46–1.40 (m, 4H, CH_2), 1.34–1.29 (m, 8H, CH_2), 0.91–0.86 (m, 6H, CH_3).

^{13}C NMR (126 MHz, $CDCl_3$, 300 K): δ (ppm) = 159.9, 158.8, 146.8, 142.0, 136.4, 136.3, 136.0, 130.0, 129.7, 128.0, 127.1, 126.9, 126.6, 126.4, 125.3, 125.2, 117.1, 117.0, 116.3, 68.5, 31.6, 29.2, 29.1, 25.7, 22.6, 22.6, 14.0 (The resulting ^{1}H and ^{13}C NMR signals were assigned as a mixture of three conformational isomers **7a**–**c** shown in Figure 2–46).

HRMS (ESI): calcd. for $[C_{64}H_{54}N_2O_2 + H]^+$: m/z = 1414.2620, found: m/z = 1414.2581.

M.p.: 160–166 °C

IR (ATR): ν (cm^{-1}) = 2926, 2359, 2342, 1586, 1559, 1425, 1308, 1254, 1028, 844, 771, 762.

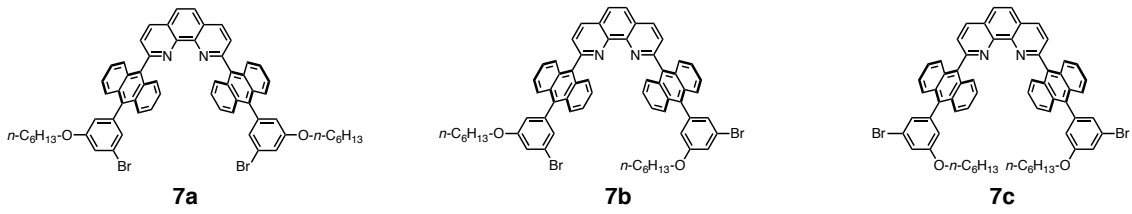

Figure 2–46. Possible structures of the conformational isomers **7a**–**c**. The interconversion rate was slower than the NMR timescale at 300 K due to the steric repulsion.

Macrocyclic ligand L1: Compounds **6** (1.01 g, 1.28 mmol, 1.0 eq), **7** (1.34 g, 1.28 mmol. 1.0 eq), K_3PO_4 (1.92 g, 9.04 mmol, 7.0 eq), and $Pd(PPh_3)_4$ (154.5 mg, 0.13 mmol, 0.1 eq) were placed in a dried two-neck flask. The inner gas was replaced by argon. Anhydrous DMF (130 mL) was added to the mixture, which was then degassed by a freeze-pump-thaw procedure. The mixture was stirred at 100 °C for 24 h. During the reaction, $Pd(PPh_3)_4$ (80.3 mg, 0.07 mmol, 0.05 eq) was added. After cooling down to room temperature, water (300 mL) was added to the mixture, which was extracted with $CHCl_3$ (ca. 300 mL × 4). The combined organic layer was

dried over Na_2SO_4, and then evaporated under reduced pressure at 80 °C to obtain a yellowish brown solid (2.31 g). The crude product was purified by column chromatography (SiO_2, ϕ = 6.0 cm, h = 5.5 cm, toluene/THF = 40/0–40/1) and a subsequent washing of the solid with $CHCl_3$ to afford **L1** as a yellowish solid (92.9 mg, 65.7 μmol, 5.1%).

^{1}H NMR (500 MHz, $CDCl_3$, 300 K): δ (ppm) = 8.52 (d, J = 8.0 Hz, 4H, Ar*H*), 8.09 (s, 4H, Ar*H*), 7.91 (d, J = 8.0 Hz, 4H, Ar*H*), 7.81 (d, J = 8.5 Hz, 8H, Ar*H*), 7.66 (d, J = 9.0 Hz, 8H, Ar*H*), 7.28–7.31 (m, 8H, Ar*H*), 7.20–7.23 (m, 8H, Ar*H*), 7.16 (d, J = 1.0 Hz, 4H, Ar*H*), 6.71 (t, J = 1.0 Hz, 2H, Ar*H*), 4.04 (t, J = 7.3 Hz, 4H, CH_2), 1.82 (tt, J = 7.3, 7.3 Hz, 4H, CH_2), 1.45 (m, 4H, CH_2), 1.34–1.29 (m, 8H, CH_2), 0.87 (t, J = 7.3 Hz, 6H, CH_3).

HRMS (ESI) mass: calcd. for $[C_{104}H_{76}N_4O_2 + H]^+$: m/z = 1414.6079, found: m/z = 1414.5923.

M.p.: > 370 °C (decomp.)

IR (ATR): ν (cm^{-1}) = 3062, 2930, 2857, 2359, 1581, 1131, 847, 763, 751, 670, 620.

Due to the low solubility of **L1** in general organic solvents, it was difficult to detect clear ^{13}C NMR signals.

Synthesis of dinuclear Ag(I)-macrocycle, $[Ag_2L1X_2](SbF_6)_2$ (X = Et_2O or H_2O)

Macrocyclic ligand **L1** (2.45 mg, 1.73 μmol, 1.0 eq) placed in a test tube was suspended in $CHCl_3$ (4.0 mL). A solution of $AgSbF_6$ in acetone (80 mM, 86 μL, 6.9 μmol, 4.0 eq) was added to the suspension. The resulting clear yellow solution was immediately concentrated to about 1 mL by evaporation under reduced pressure. Yellow plate crystals suitable for single-crystal XRD measurement were obtained by recrystallization from the solution by vapor diffusion of diethyl ether under a dark condition for 2 days at room temperature. To isolate the title complex as a solid, the crystals were collected by centrifugation, and then washed by diethyl ether (ca. 0.5 mL × 2). After being kept in the dark for several hours, $[Ag_2\mathbf{L1}X_2](SbF_6)_2\cdot(Sol.)_n$ (X = Et_2O or H_2O, Sol. = solvent) (2.90 mg, 1.08 μmol, 63%) was obtained as a yellow solid.

NOTE: The isolation yield of the product was calculated to be 63% based on the integral ratio of the ^{1}H NMR signals in the presence of *p*-dimethoxybenzene as the internal standard. The resulting composition can be described as $[Ag_2\mathbf{L1}(Et_2O)_2][Ag_2\mathbf{L1}(H_2O)_2](SbF_6)_4\cdot(acetone)_{3.4}\cdot(CHCl_3)_m\cdot(Et_2O)_{1.4}\cdot(H_2O)_n$.

^{1}H NMR (500 MHz, $CDCl_3$, 300 K): δ (ppm) = 8.89 (d, J = 8.0 Hz, 4H, Ar*H*), 8.36 (s, 4H, Ar*H*), 8.25 (d, J = 8.5 Hz, 4H, Ar*H*), 7.92 (d, J = 9.0 Hz, 8H, Ar*H*), 7.51 (d, J = 9.0 Hz, 8H, Ar*H*), 7.48–7.45 (m, 8H, Ar*H*), 7.42–7.39 (m, 8H, Ar*H*), 7.09 (s, 4H, Ar*H*), 6.85 (s, 2H, Ar*H*), 4.01 (t, J = 6.8 Hz, 4H, CH_2), 1.79 (tt, J = 7.0, 7.0 Hz, 4H, CH_2), 1.44 (m, 4H, CH_2), 1.34–1.27 (m, 8H,

CH_2), 0.86 (t, J = 7.5 Hz, 6H, CH_3).

ESI-TOF mass: calcd. for $[Ag_2C_{104}H_{72}N_4O_2]^{2+}$: m/z = 814.20, found m/z = 814.19.

Crystal data of $[Ag_2L1(Et_2O)_2][Ag_2L1(H_2O)_2](SbF_6)_4\cdot(CHCl_3)_{8.28}\cdot(H_2O)_{6.7}$

Crystal data for $C_{224.28}H_{180.28}Ag_4Cl_{24.85}F_{24}N_8O_{14.7}Sb_4$: F_w = 5478.22, crystal dimensions 0.1 × 0.1 × 0.1 mm, triclinic, space group P–1, a = 12.4086(6), b = 22.2413(9), c = 23.737(1) Å, α = 92.379(1), β = 90.228(1), γ = 105.396(1)°, V = 6309.7(5) Å^3, Z = 1, ρ_{calcd} = 1.442 gcm^{-3}, μ = 1.0588 mm^{-1}, T = 113 K, λ (MoKα) = 0.71075 Å, $2\theta_{max}$ = 50.7°, 50534/22741 reflection collected/unique (R_{int} = 0.0657), R_1 = 0.0797 ($I > 2\sigma(I)$), wR_2 = 0.2675 (for all data), GOF = 1.112, largest diff. peak and hole 1.73/–1.69 eÅ^{-3}. The contribution of solvent electron density was removed by the SQUEEZE function.[17] CCDC deposit number 1026266.

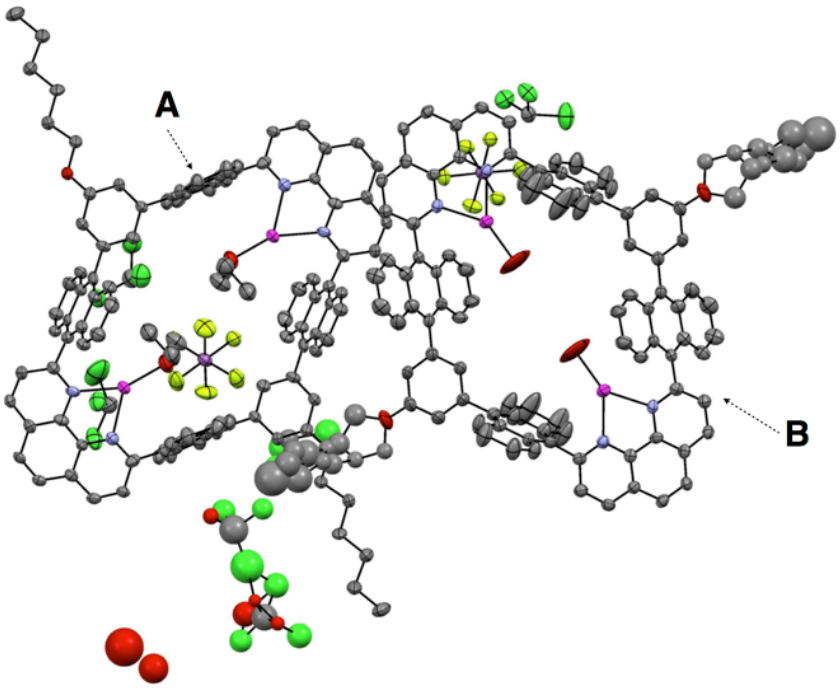

Figure 2–47. ORTEP view (50% probability level) of $[Ag_2\mathbf{L1}X_2](SbF_6)_2\cdot(Sol.)_n$. **A** and **B** represent $[Ag_2\mathbf{L1}(Et_2O)_2]^{2+}$ and $[Ag_2\mathbf{L1}(H_2O)_2]^{2+}$, respectively. Hydrogen atoms are omitted for clarity. (Ag: magenta, C: grey, Cl: pale green, F: yellow, N: pale blue, O: red, Sb: pink)

Investigation of the complexation behavior between L1 and $AgSbF_6$ in $CDCl_3$ at 300 K

To a solution of $[Ag_2\mathbf{L1}X_2](SbF_6)_2\cdot(Sol.)_n$ in $CDCl_3$ (30 μM, 450 μL, 0.014 μmol, 1.0 eq) was added a solution of **L1** in $CDCl_3$ (80 μM).

Complexation of $[Ag_2L1X_2](SbF_6)_2$ and anthracene

^{1}H NMR titration experiment at 300 K

To a solution of $[Ag_2\mathbf{L1}X_2](SbF_6)_2\cdot(Sol.)_n$ in $CDCl_3$ (107 μM, 475 μL, 0.051 μmol, 1.0 eq) was added a solution of anthracene in $CDCl_3$ (20 mM). Curve fitting of the obtained data determined a stability constant K_a(Anthracene) = [Anthracene⊂$[Ag_2\mathbf{L1}]^{2+}$]/([Anthracene][$[Ag_2\mathbf{L1}X_2]^{2+}$]) to be (3.0 ± 0.4) × 10^4 M^{-1} in $CDCl_3$ at 300 K.

^{1}H NMR titration experiment at 220 K

To a solution of $[Ag_2\mathbf{L1}X_2](SbF_6)_2\cdot(Sol.)_n$ in $CDCl_3$ (65 μM, 450 μL, 0.029 μmol, 1.0 eq) was added a solution of anthracene in $CDCl_3$ (20 mM).

Crystallization of Anthracene⊂$[Ag_2L1(CH_2Cl_2)_2](SbF_6)_2$

To a suspension of **L1** (230 μM, 450 μL, 0.10 μmol, 1.0 eq) in $CHCl_3$ was added a solution of $AgSbF_6$ (200 mM, 2.1 μL, 0.4 μmol, 4.0 eq) in acetone and a solution of anthracene (200 mM, 5.2 μL, 1.0 μmol, 10 eq) to obtain a clear yellow solution. The solvent was once removed by evaporation under reduced pressure. Then a resulting solid was dissolved in CH_2Cl_2 (250 μL). Yellow brock crystals suitable for single crystals XRD measurement were obtained after *n*-pentane vapor diffusion in the dark over about 10 days.

Crystal data of Anthracene⊂$[Ag_2L1(CH_2Cl_2)_2](SbF_6)_2\cdot(C_5H_{12})_2\cdot(CH_2Cl_2)_2$

Crystal data of $C_{132}H_{118}Ag_2Cl_8F_{12}N_4O_2Sb_2$: F_w = 2763.25, crystal dimensions 0.30 × 0.30 × 0.10 mm, monoclinic, space group $P2_1/c$, a = 18.8596(8), b = 13.4589(6), c = 23.9721(11) Å, β = 99.0960(13)°, V = 6008.3(5) $Å^3$, Z = 2, ρ_{calcd} = 1.527, μ = 1.0146 mm^{-1}, T = 93 K, λ(MoKα) = 0.71075 Å, $2\theta_{max}$ = 55.0°, 58014/13762 reflection collected/unique (R_{int} = 0.0601), R_1 = 0.0836 ($I > 2\sigma(I)$), wR_2 = 0.2595 (for all data), GOF = 1.060 largest diff. peak and hole 2.69/–1.72 $eÅ^{-3}$.

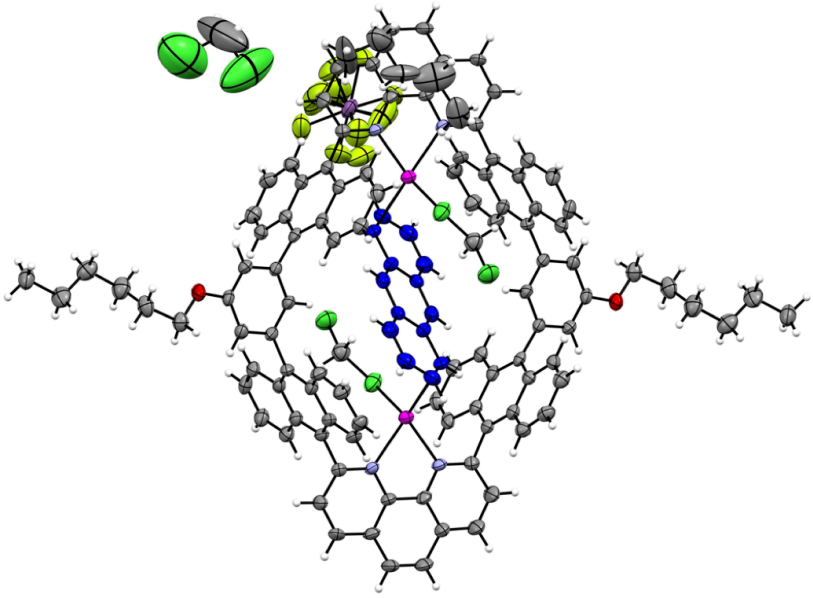

Figure 2–48. ORTEP view (50% probability level) of Anthracene⊂[Ag_2**L1**(CH_2Cl_2)$_2$](SbF_6)$_2$·(C_5H_{12})$_2$·(CH_2Cl_2)$_2$. (Ag: magenta, C: grey, C of anthracene: blue, Cl: pale green F: yellow, H: white, N: blue, O: red, Sb: pink)

Complexation of [Ag_2L1X_2](SbF_6)$_2$ and naphthalene

^{1}H NMR titration experiment

To a solution of [Ag_2**L1**X_2](SbF_6)$_2$·(Sol.)$_n$ in $CDCl_3$ (107 μM, 475 μL, 0.051 μmol, 1.0 eq) was added a solution of naphthalene in $CDCl_3$ (20 mM).

Complexation of [Ag_2L1X_2](SbF_6)$_2$ and *p*-xylene

^{1}H NMR titration experiment

To a solution of [Ag_2**L1**X_2](SbF_6)$_2$·(Sol.)$_n$ in $CDCl_3$ (107 μM, 475 μL, 0.051 μmol, 1.0 eq) was added a solution of *p*-xylene in $CDCl_3$ (9.7 mM).

Crystallization of (*p*-Xylene)$_2$⊂[Ag_2L1(CF_3SO_3)$_2$]

Macrocyclic ligand **L1** (0.85 mg, 0.60 μmol, 1.0 eq) placed in a test tube was suspended in CH_2Cl_2/*p*-xylene = 4/1 (1.25 mL). A solution of $AgCF_3SO_3$ in *p*-xylene (40 mM, 300 μL, 12 μmol, 20 eq) was added to the suspension. The resulting clear yellow solution was kept in the dark for a week at room temperature, and then yellow block crystals suitable for single-crystal

XRD were obtained. To isolate the title complex as a solid, the crystals were collected by centrifugation, and then washed with diethyl ether (ca. 0.5 mL × 4). After being kept in the dark for 5 h, (*p*-Xylene)$_2$⊂[Ag$_2$**L1**(CF$_3$SO$_3$)$_2$]·(Sol.)$_n$ (0.90 mg, 0.45 μmol, 75%) was obtained as a yellow solid.

NOTE: The isolation yield of the product was calculated to be 75% based on the resulting composition, (*p*-Xylene)$_2$⊂[Ag$_2$**L1**(CF$_3$SO$_3$)$_2$]·(Et$_2$O), which was estimated from the integral ratio of the ^{1}H NMR signals.

^{1}H NMR (500 MHz, CDCl$_3$, 300 K): δ (ppm) = 8.90 (d, J = 8.0 Hz, 4H, Ar*H*), 8.38 (s, 4H, Ar*H*), 8.25 (d, J = 8.0 Hz, 4H, Ar*H*), 7.95 (d, J = 8.5 Hz, 8H, Ar*H*), 7.50 (d, J = 8.0 Hz, 8H, Ar*H*), 7.40–7.34 (m, 16H, Ar*H*), 7.17 (s, 2H, Ar*H*), 7.11 (s, 4H, Ar*H*), 7.07 (s, 8H, Ar*H*), 4.02 (t, J = 6.8 Hz, 4H, C*H*$_2$), 2.31 (s, 6H, C*H*$_3$), 1.80 (m, 4H, C*H*$_2$), 1.47–1.42 (m, 4H, C*H*$_2$), 1.32–1.30 (m, 8H, C*H*$_2$), 0.86 (m, 6H, C*H*$_3$).

Crystal data of (*p*-Xylene)$_2$⊂[Ag$_2$L1(CF$_3$SO$_3$)$_2$]·(*p*-Xylene)$_{1.05}$

Crystal data for C$_{130.39}$H$_{106.49}$Ag$_2$F$_6$N$_4$O$_8$S$_2$: F_w = 2251.31, crystal dimensions 0.1 × 0.1 × 0.1 mm, monoclinic, space group $C2/c$, a = 29.873(2), b = 36.531(2), c = 24.340(1) Å, β = 120.035(1)°, V = 22996(2) Å^3, Z = 8, ρ_{calcd} = 1.300 gcm^{-3}, μ = 0.4442 mm^{-1}, T = 93 K, λ(MoKα) = 0.71075 Å, 2θ_{max} = 48.2°, 69119/17265 reflection collected/unique (R_{int} = 0.1105), R_1 = 0.1276 ($I > 2\sigma(I)$), wR_2 = 0.3917 (for all data), GOF = 1.217, largest diff. peak and hole 1.45/–0.71 e/Å^{-3}. CCDC deposit number 1026267.

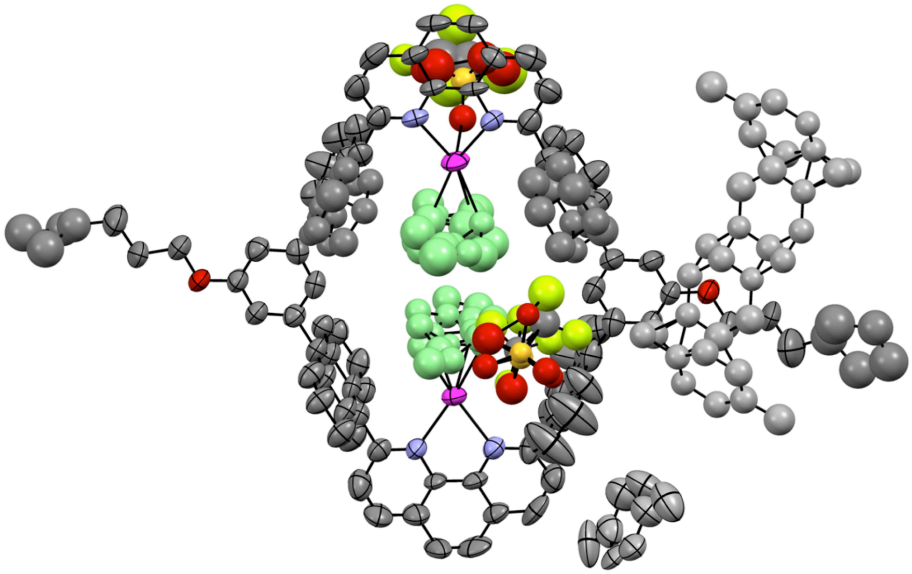

Figure 2–49. ORTEP view (50% probability level) of (*p*-Xylene)$_2$⊂[Ag$_2$**L1**(CF$_3$SO$_3$)$_2$]·(*p*-Xylene)$_{1.05}$. Hydrogen atoms are omitted for clarity. (Ag: magenta, C: grey, C of *p*-xylene within [Ag$_2$**L1**]$^{2+}$: light green, C of *p*-xylene out of [Ag$_2$**L1**]$^{2+}$: light grey, F: yellow, N: pale blue, O: red, S: orange)

Complexation of $[Ag_2L1X_2](SbF_6)_2$ and pCp

^{1}H NMR titration experiment

To a solution of $[Ag_2\mathbf{L1}X_2](SbF_6)_2\cdot(Sol.)_n$ in $CDCl_3$ (107 μM, 475 μL, 0.051 μmol, 1.0 eq) was added a solution of pCp in $CDCl_3$ (10.3 mM). *p*-Dimethoxybenzene (0.025 μmol) was used as an internal standard.

Titration experiment using UV-Vis spectroscopy

To a solution of $[Ag_2\mathbf{L1}X_2](SbF_6)_2\cdot(Sol.)_n$ in $CHCl_3$ (50 μM, 300 μL, 0.015 μmol, 1.0 eq) was added a solution of pCp in $CHCl_3$ (7.5 mM).

Crystallization of pCp⊂$[Ag_2L1](SbF_6)_2$

Macrocyclic ligand **L1** (1.87 mg, 1.32 μmol, 1.0 eq) placed in a test tube was suspended in $CHCl_3$ (3.5 mL). A solution of $AgSbF_6$ in acetone (80 mM, 66.0 μL, 5.28 μmol, 4.0 eq) and a solution of pCp in $CHCl_3$ (40 mM, 34.0 μL, 1.36 μmol, 1.0 eq) were added to the suspension sequentially to obtain a clear yellow solution, which was concentrated to about 1 mL by evaporation under reduced pressure. Yellow plate crystals suitable for single-crystal XRD measurement were obtained by recrystallization from the solution by vapor diffusion of diethyl ether in the dark for 4 days at room temperature. To isolate the title complex as a solid, the crystals were collected by centrifugation, and then washed by diethyl ether (ca. 0.5 mL × 3). After being kept under vacuum in the dark for 2 h, pCp⊂$[Ag_2\mathbf{L1}](SbF_6)_2\cdot(Sol.)_n$ (2.48 mg, 0.933 μmol, 71%) was obtained as a yellow solid.

NOTE: The isolation yield of the product was calculated to be 71% based on the integral ratio of the ^{1}H NMR signals in the presence of *p*-dimethoxybenzene as an internal standard. The resulting composition can be described as pCp⊂$[Ag_2\mathbf{L1}](SbF_6)_2\cdot(acetone)_{0.1}\cdot(CHCl_3)_m\cdot(Et_2O)_{0.2}\cdot(H_2O)_n$.

^{1}H NMR (500 MHz, $CDCl_3$, 293 K): δ (ppm) = 8.75 (d, J = 8.5 Hz, 4H, Ar*H*), 8.25 (s, 4H, Ar*H*), 8.08 (d, J = 9.0 Hz, 8H, Ar*H*), 7.97 (d, J = 8.5 Hz, 4H, Ar*H*), 7.55–7.52 (m, 8H, Ar*H*), 7.45–7.42 (m, 8H, Ar*H*), 7.41 (d, J = 1.0 Hz, 4H, Ar*H*), 7.37 (d, J = 9.0 Hz, 8H, Ar*H*), 6.96 (t, J = 1.0 Hz, 2H, Ar*H*), 4.20 (t, J = 6.8 Hz, 4H, C*H*$_2$), 3.81 (s, 8H, Ar*H*), 1.93 (tt, J = 7.3, 7.3 Hz, 4H, C*H*$_2$), 1.60–1.48 (m, 4H, C*H*$_2$), 1.43–1.35 (m, 8H, C*H*$_2$), 1.17 (s, 8H, C*H*$_2$), 0.92 (t, J = 7.0 Hz, 6H, C*H*$_3$).

ESI-TOF mass: calcd. for $[Ag_2C_{120}H_{88}N_4O_2]^{2+}$: m/z = 918.77, found m/z = 918.80.

Crystal data for pCp⊂[Ag_2L1]$(SbF_6)_2$·$(CHCl_3)_2$·$(C_4H_{10}O)_2$

Crystal data for $C_{130}H_{114}Ag_2Cl_6F_{12}N_4O_4Sb_2$: F_w = 2696.28, crystal dimensions 0.1 × 0.1 × 0.1 mm, monoclinic, space group $P2_1/c$, a = 17.7926(4), b = 13.3933(3), c = 24.5823(6) Å, β = 99.1138(2)°, V = 5784.0(3) $Å^3$, Z = 2, ρ_{calcd} = 1.548 gcm^{-3}, μ = 1.0085 mm^{-1}, T = 96 K, λ(MoKα) = 0.71075 Å, $2\theta_{max}$ = 55.0°, 93506/13256 reflection collected/unique (R_{int} = 0.0719), R_1 = 0.0812 ($I > 2\sigma(I)$), wR_2 = 0.2368 (for all data), GOF = 1.020, largest diff. peak and hole 1.11/–1.83 $eÅ^{-3}$. CCDC deposit number 1026281.

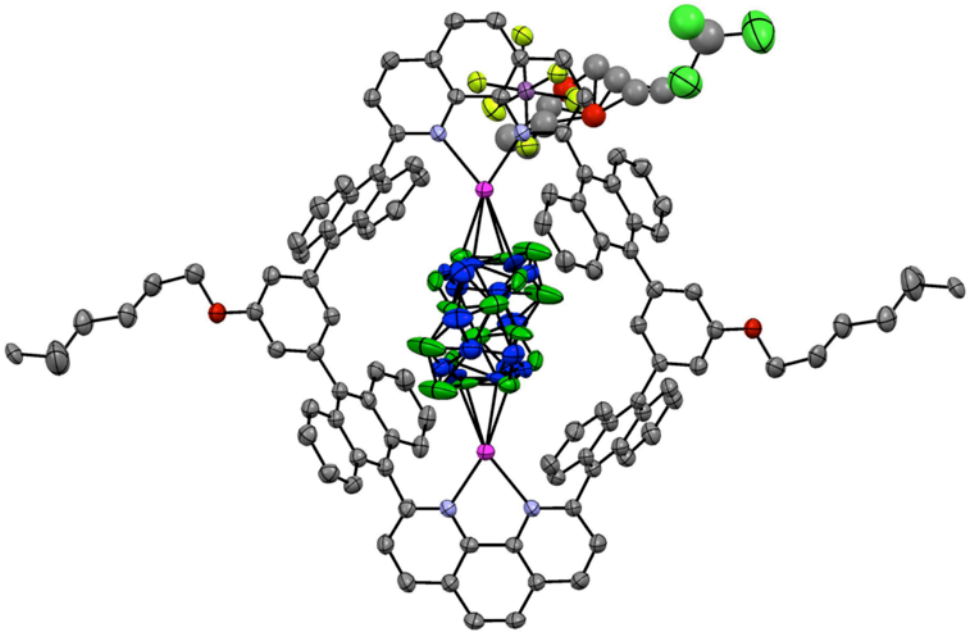

Figure 2–50. ORTEP view (50% probability level) of pCp⊂[Ag_2**L1**]$(SbF_6)_2$·$(CHCl_3)_2$·$(C_4H_{10}O)_2$. Hydrogen atoms are omitted for clarity. (Ag: magenta, C: grey, C of pCp: green and blue, Cl: pale green, F: yellow, N: pale blue, O: red, Sb: pink)

Estimation of the binding constant between [Ag_2L1X_2]$(SbF_6)_2$ and pCp at 300 K in $CDCl_3$

To a solution of pCp⊂[Ag_2**L1**]$(SbF_6)_2$·$(Sol.)_n$ in $CDCl_3$ (475 μL, 115 μM, 0.055 μmol, 1.0 eq) was added a solution of $FeCp_2$ in $CDCl_3$ (20 mM). *p*-Dimethoxybenzene (0.025 μmol) was used as the internal standard.

The binding constants for guest inclusion of the dinuclear Ag(I)-macrocycle $[Ag_2\mathbf{L1}X_2]^{2+}$ with pCp (K_a(pCp)) and $FeCp_2$ ($K_a(FeCp_2)$), and the equilibrium constant of the guest exchange reaction (K_{ex}) were defined as shown below.

$$[Ag_2\mathbf{L1}X_2]^{2+} + pCp \overset{K_a(pCp)}{\rightleftharpoons} pCp\subset[Ag_2\mathbf{L1}]^{2+}$$

$$[Ag_2\mathbf{L1}X_2]^{2+} + FeCp_2 \overset{K_a(FeCp_2)}{\rightleftharpoons} FeCp_2\subset[Ag_2\mathbf{L1}]^{2+}$$

$$pCp\subset[Ag_2\mathbf{L1}]^{2+} + FeCp_2 \overset{K_{ex}}{\rightleftharpoons} FeCp_2\subset[Ag_2\mathbf{L1}]^{2+} + pCp$$

$$K_a(pCp) = \frac{[pCp\subset[Ag_2\mathbf{L1}]^{2+}]}{[[Ag_2\mathbf{L1}X_2]^{2+}]\ [pCp]}\ M^{-1}$$

$$K_a(FeCp_2) = \frac{[FeCp_2\subset[Ag_2\mathbf{L1}]^{2+}]}{[[Ag_2\mathbf{L1}X_2]^{2+}]\ [FeCp_2]} = (6.2 \pm 0.9) \times 10^4\ M^{-1}$$

$$K_{ex} = \frac{[FeCp_2\subset[Ag_2\mathbf{L1}]^{2+}]\ [pCp]}{[pCp\subset[Ag_2\mathbf{L1}]^{2+}]\ [FeCp_2]}$$

$$= \frac{[[Ag_2\mathbf{L1}X_2]^{2+}]\ [pCp]}{[pCp\subset[Ag_2\mathbf{L1}]^{2+}]} \cdot \frac{[FeCp_2\subset[Ag_2\mathbf{L1}]^{2+}]}{[[Ag_2\mathbf{L1}X_2]^{2+}]\ [FeCp_2]}$$

$$= \frac{K_a(FeCp_2)}{K_a(pCp)}$$

When an excess $FeCp_2$ (25 eq) was added to a solution of $pCp\subset[Ag_2\mathbf{L1}](SbF_6)_2$ in $CDCl_3$, no guest exchange reactions between $pCp\subset[Ag_2\mathbf{L1}]^{2+}$ and $FeCp_2$ were observed (Figure 2–26). Then, assuming that less than 1% of pCp was replaced by $FeCp_2$ under this condition, the concentration of each guest or complex was described as shown below. (NOTE: As the total volume of the solution was increased from 475 μL to 542 μL due to the addition of a solution of $FeCp_2$ to $CDCl_3$, the total concentration of $pCp\subset[Ag_2\mathbf{L1}]^{2+}$ decreased from 115 μM to 100.7 μM.)

$$[pCp\subset[Ag_2\mathbf{L1}]^{2+}] > 99.7\ \mu M \qquad [pCp] < 1.0\ \mu M$$

$$[FeCp_2\subset[Ag_2\mathbf{L1}]^{2+}] < 1.0\ \mu M \qquad [FeCp_2] > 2.53\ mM$$

In this case,

$$K_{ex} < 4 \times 10^{-6}$$

Then

$$K_a(pCp) = \frac{K_a(FeCp_2)}{K_{ex}} > 10^9\ M^{-1}$$

Control Experiments

Complexation of dinuclear metallo-macrocycles $[M_2L1X_m]^{n+}$ (M = Cu(I), Hg(II), or Zn(II), X = anion or solvent) and pCp

To a solution of **L1** in $CDCl_3$ (70 μM, 450 μL, 0.032 μmol, 1.0 eq) was added a solution of metal salt ($Cu(CH_3CN)_4BF_4$, $Hg(CF_3SO_3)_2$, or $Zn(CF_3SO_3)_2$) in $(CD_3)_2CO$ (20 mM, 6.0 μL, 0.12 μmol, 3.8 eq). To the mixture was added a solution of pCp in $CDCl_3$ (20 mM).

Complexation of macrocyclic ligand L1 and pCp

To a solution of **L1** in $CDCl_3$ (125 μM, 450 μL, 0.056 μmol, 1.0 eq) was added a solution of pCp in $CDCl_3$ (20 mM).

Complexation of dinuclear Ag(I)-macrocycle $[Ag_2L1X_m]^{n+}$ (X = anion or solvent) with pCp

To a solution of **L1** in $CDCl_3$ (70 μM, 450 μL, 0.032 μmol, 1.0 eq) was added a solution of Ag(I) salt ($AgSbF_6$, $AgBF_4$, or $AgCF_3SO_3$) in $(CD_3)_2CO$ (20 mM, 6.0 μL, 0.12 μmol, 3.8 eq). To the mixture was added a solution of pCp in $CDCl_3$ (20 mM).

Complexation of $[AgL2(Et_2O)]SbF_6$ and pCp

^{1}H NMR titration experiment

To a solution of $[Ag\mathbf{L2}(Et_2O)]SbF_6$ in $CDCl_3/(CD_3)_2CO$ = 80/1 (185 μM, 532 μL, 0.10 μmol, 1.0 eq) was added a solution of pCp in $CDCl_3$ (8.4 mM). *p*-Dimethoxybenzene (0.025 μmol) was used as the internal standard. Curve fitting of the obtained data determined a stability constant $K'_{a1}(pCp) = [pCp\subset[Ag\mathbf{L2}]^+]/([pCp][[Ag\mathbf{L2}(Et_2O)]^+])$ and $K'_{a2}(pCp) = [pCp\subset[Ag\mathbf{L2}]_2^{2+}]/([[Ag\mathbf{L2}(Et_2O)]^+][pCp\subset[Ag\mathbf{L2}]^+])$ to be $(3.0 \pm 0.4) \times 10^4$ M^{-1} and $(1.0 \pm 0.1) \times 10^3$ M^{-1} in $CDCl_3$ at 300 K, respectively.

Crystallization of $pCp\subset[AgL2]_2(SbF_6)_2$

To a solution of **L2** in $CDCl_3$ (350 μL, 450 μL, 0.158 μmol, 1.0 eq) was added a solution of $AgSbF_6$ in CD_3CN (40 mM, 5.9 μL 0.24 μmol, 1.5 eq). The solvent was once evaporated to yield a pale yellow solid. The resulting solid was dissolved in $CDCl_3$ (450 μL) to obtain a clear yellow solution. To the solution was added a solution of pCp in $CDCl_3$ (40 mM, 8.0 μL, 0.32 μmol, 2.0 eq). Yellow block crystals suitable for single-crystal XRD measurement were obtained by recrystallization from the solution by slow evaporation of the solvent under a dark

condition for several weeks.

Crystal data of pCp⊂[AgL2]$_2$(SbF$_6$)$_2$

Crystal data for $C_{48}H_{32}AgF_6N_2Sb$: F_w = 980.40, crystal dimensions 0.20 × 0.20 × 0.20 mm, triclinic, space group *P*–1, a = 12.2864(3), b = 12.6957(3), c = 12.8907(4) Å, α = 86.4763(8), β = 88.5529(9), γ = 71.3157(7)°, V = 1901.14(9) Å^3, Z = 2, ρ_{calcd} = 1.713 gcm^{-3}, μ = 1.2914 mm^{-1}, T = 93 K, λ(MoKα) = 0.71075 Å, 2θ_{max} = 55.0°, 18470/8492 reflection collected/unique (R_{int} = 0.0222), R_1 = 0.0290 ($I > 2\sigma(I)$), wR_2 = 0.0763 (for all data), GOF = 1.080, largest diff. peak and hole 1.64/–0.91 eÅ^{-3}. CCDC deposit number 1026269.

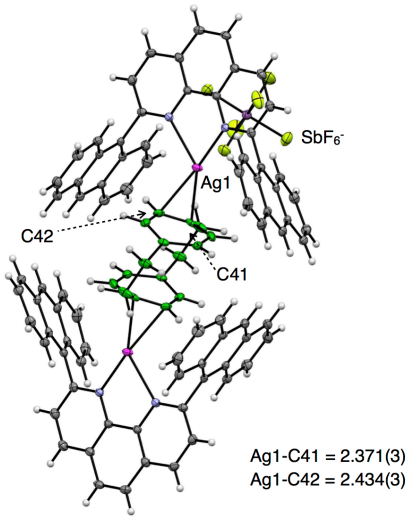

Figure 2–51. ORTEP view (50% probability level) of pCp⊂[Ag**L2**]$_2$(SbF$_6$)$_2$. (Ag: magenta, C: grey, C of pCp: green, F: yellow, N: pale blue, Sb: pink)

Complexation of [Ag$_2$L1X$_2$](SbF$_6$)$_2$ and FeCp$_2$

^{1}H NMR titration experiment at 300 K

To a solution of [Ag$_2$**L1**X$_2$](SbF$_6$)$_2$·(Sol.)$_n$ in $CDCl_3$ (107 μM, 500 μL, 0.037 μmol, 1.0 eq) was added a solution of $FeCp_2$ in $CDCl_3$ (20 mM). Curve fitting of the obtained data determined a stability constant $K_a(FeCp_2)$ = [$FeCp_2$⊂[Ag$_2$**L1**]$^{2+}$]/([$FeCp_2$][[Ag$_2$**L1**X$_2$]$^{2+}$]) to be (6.2 ± 0.9) × 10^4 M^{-1} in $CDCl_3$ at 300 K.

^{1}H NMR titration experiment at 220 K

To a solution of [Ag$_2$**L1**X$_2$](SbF$_6$)$_2$·(Sol.)$_n$ in $CDCl_3$ (80 μM, 500 μL, 0.037 μmol, 1.0 eq) added a solution of $FeCp_2$ in $CDCl_3$ (20 mM).

Complexation of $[Ag_2L1X_2](SbF_6)_2$ with $FeCp_2$'

^{1}H NMR titration experiment

To a solution of $[Ag_2\mathbf{L1}X_2](SbF_6)_2\cdot(Sol.)_n$ in $CDCl_3$ (60 μM, 475 μL, 0.028 μmol, 1.0 eq) was added a solution of $FeCp_2$' in $CDCl_3$ (20 mM). *p*-Dimethoxybenzene (0.025 μmol) was added as the internal standard.

Crystallization of $FeCp_2'\subset[Ag_2L1]_2(SbF_6)_2$

To a solution of $[Ag_2\mathbf{L1}X_2](SbF_6)_2\cdot(Sol.)_n$ (80 μM, 450 μL, 0.036 μmol, 1.0 eq) in $CDCl_3$ was added a solution of $FeCp_2$' (100 mM, 7.2 μL, 20 eq) in $CHCl_3$. Yellow brock crystals suitable for single crystal XRD measurement was obtained after *n*-pentane vapor diffusion in the dark for several days.

Crystal data of $FeCp_2'\subset[Ag_2L1]_2(SbF_6)_2\cdot(CHCl_3)_4$

Crystal data for $C_{119}H_{92}Ag_2Cl_{12}F_{12}FeN_4O_3SbF_2$: F_w = 2794.56, crystal dimensions 0.10 × 0.10 × 0.10 mm, monoclinic, space group $P2_1/c$, a = 19.048(3), b = 13.318(2), c = 22.871(4) Å, β = 96.000(2)°, V = 5770.3(16) Å^3, Z = 2, ρ_{calcd} = 1.608 gcm^{-3}, μ = 1.2665 mm^{-1}, T = 109 K, λ(MoKα) = 0.71075 Å, $2\theta_{max}$ = 48.0°, 39847/9046 reflection collected/unique (R_{int} = 0.1104), R_1 = 0.0788 ($I > 2\sigma(I)$), wR_2 = 0.2410 (for all data), GOF = 1.053 largest diff. peak and hole 1.13/–1.16 eÅ^{-3}.

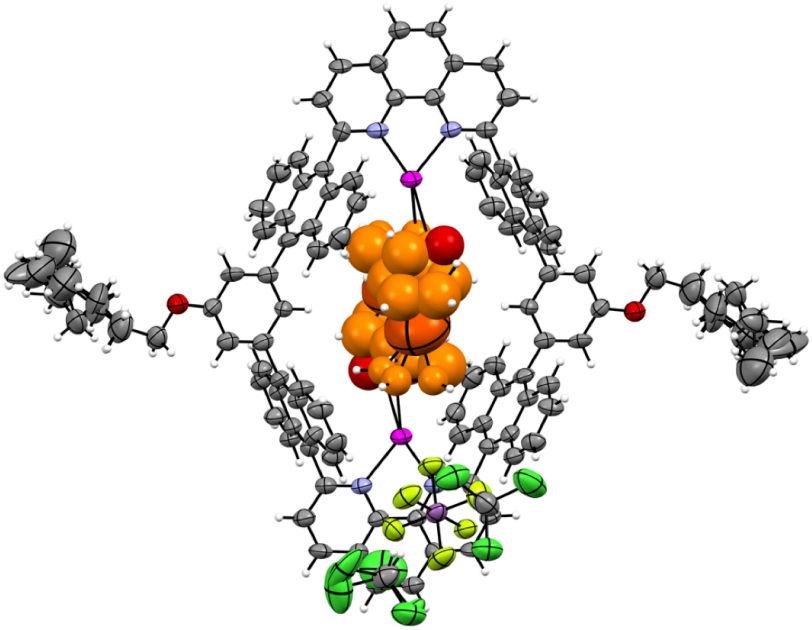

Figure 2–52. ORTEP view (50% probability level) of $FeCp_2'\subset[Ag_2\mathbf{L1}](SbF_6)_2\cdot(CHCl_3)_4$. (Ag: magenta, C: grey, C of $FeCp_2$': orange, Cl: pale green, F: yellow, Fe: red, N: pale blue, O: red, Sb: pink)

Electrochemical measurements

Electrochemical measurement of $[Ag_2L1X_2](SbF_6)_2$

A solution of $[Ag_2\mathbf{L1}X_2](SbF_6)_2 \cdot (Sol.)_n$ in CH_2Cl_2 containing 0.1 M $TBAPF_6$ (0.8 mL, 430 μM, 0.34 μmol, 1.0 eq) was prepared in a CV cell. The sample solutions were deoxygenated with pure nitrogen prior to electrochemical measurements. Electrochemical measurement was conducted under a dark condition at 291 K. The working electrode was a 3 mm glassy carbon electrode; a platinum wire served as the auxiliary electrode, and the reference electrode was as Ag^+/Ag electrode (a silver wire immersed in 0.1 M $TBAClO_4$/0.01 M $AgNO_3$ in CH_3CN).

Electrochemical measurement of $AgSbF_6$

A solution of $AgSbF_6$ in CH_2Cl_2 containing 0.1 M $TBAPF_6$ (2.0 mL, 430 μM, 0.86 μmol, 1.0 eq) was prepared in a CV cell. The sample solutions were deoxygenated with pure nitrogen prior to electrochemical measurements. Electrochemical measurement was conducted under a dark condition at 291 K. The working electrode was a 3 mm glassy carbon electrode; a platinum wire served as the auxiliary electrode, and the reference electrode was as Ag^+/Ag electrode (a silver wire immersed in 0.1 M $TBAClO_4$/0.01 M $AgNO_3$ in CH_3CN).

Electrochemical measurement of the mixture of $[Ag_2L1X_2](SbF_6)_2$ and $FeCp_2$

The equipment used for the electrochemical measurements is drawn in Figure 2–53b. A solution of $FeCp_2$ in CH_2Cl_2 containing 0.1 M $TBAPF_6$ (0.25 mL, 200 μM, 0.05 μmol, 1.0 eq) was prepared in a sample holder with a diameter of 9 mm. A working electrode (3 mm glassy carbon electrode) and an auxiliary electrode (platinum wire) were immersed in this solution. Then, the sample holder and a reference electrode (Ag^+/Ag electrode (a silver wire immersed in 0.1 M $TBAClO_4$/0.01 M $AgNO_3$ in CH_3CN) were immersed in CH_2Cl_2 containing 0.1 M $TBAPF_6$ (9.0 mL). The sample solutions were deoxygenated with pure nitrogen prior to electrochemical measurements. To the sample solution was added $[Ag_2\mathbf{L1}X_2](SbF_6)_2 \cdot (Sol.)_n$. Electrochemical measurement was conducted under a dark condition.

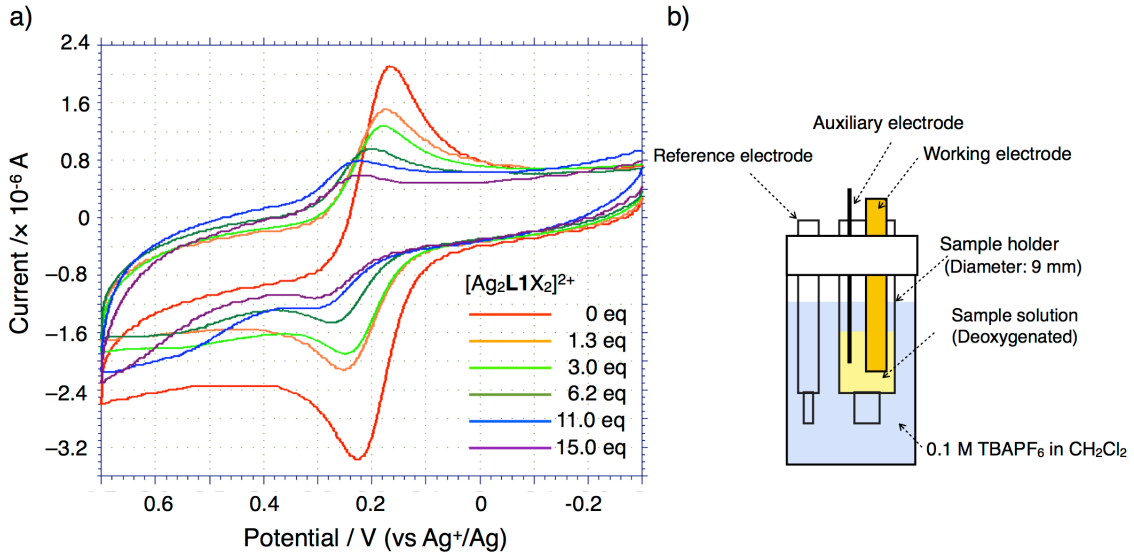

Figure 2–53. a) Cyclic voltammograms of mixtures of $FeCp_2$ (200 μM) and different amounts of $[Ag_2\mathbf{L1}X_2](SbF_6)_2{\cdot}(Sol.)_n$ in CH_2Cl_2 containing 0.1 M $TBAPF_6$ at 291 K and b) an equipment used for the measurement. Scan rate; 50 mVs^{-1}.

2–5. References

[1] a) Watson, M. D.; Fechtenkötter, A.; Müllen, K. *Chem. Rev.* **2001**, *101*, 1267–1300. b) Hunter, C. A.; Lawson, K. R.; Perkins, J.; Urch, C. *J. Chem. Soc., Perkin Trans. 2*, **2001**, 651–669. c) Meyer, E. A.; Castellano, R. K.; Diederich, F. *Angew. Chem Int. Ed.* **2003**, *42*, 1210–1250.

[2] a) Kaanumalle, L. S.; Gibb, C. L. D.; Gibb, B. C.; Ramamurthy, V. *J. Am. Chem. Soc.* **2005**, *127*, 3674–3675. b) Kaanumalle, L. S.; Ramamurthy, V. *Chem. Commun.* **2007**, 1062–1064. c) Barnes, J. C.; Jurícek, M.; Strutt, N. L.; Frasconi, M.; Sampath, S.; Giesener, M. A.; McGrier, P. L.; Bruns, C. J.; Stern, C. L.; Sarjeant, A. A.; Stoddart, J. F. *J. Am. Chem. Soc.* **2013**, *135*, 183–192. d) Spenst, P.; Würthner, F. *Angew. Chem. Int. Ed.* **2015**, *54*, 10165–10168.

[3] a) Anderson, S.; Anderson, H. L.; Bashall, A.; McPartlin, M.; Sanders, J. K. M. *Angew. Chem. Int. Ed*. **1995**, *34*, 1096–1099. b) Amendola, V.; Fabbrizzi, L.; Mangano, C.; Pallavicini, P.; Poggi, A.; Taglietti, A. *Coord. Chem. Rev*. **2001**, *219–221*, 821–837. c) Fabbrizzi, L.; Foti, F.; Patroni, S.; Pallavicini, P.; Taglietti, A. *Angew. Chem. Int. Ed.* **2004**, *43*, 5073–5077. d) Yanagisawa, M.; Tashiro, K.; Yamasaki, M.; Aida, T. *J. Am. Chem. Soc.* **2007**, *129*, 11912–11913. e) Devoille, A. M. J.; Richardson, P.; Bill, N. L.; Sessler, J. L.; Love, J. B. *Inorg. Chem.* **2011**, *50*, 3116–3126.

[4] a) Muetterties, E. L.; Bleeke, J. R.; Wucherer, E. J. *Chem. Rev.* **1982**, *82*, 499–525. b) Fagan, P. J.; Ward, M. D.; Calabrese, J. C. *J. Am. Chem. Soc.* **1989**, *111*, 1698–1719. c) *Modern Arene Chemistry*; Astruc, D., Eds.; WILEY-VCH Verlag GmbH & Co. KGaA: Weinheim, 2002. d) Murahashi, T.; Fujimoto, M.; Oka, M.; Hashimoto, Y.; Umemura, T.; Tatsumi, Y.; Nakao, Y.; Ikeda, A.; Sasaki, S. Kurosawa, H. *Science* **2006**, *313*, 1104–1107.

[5] a) Griffith, E. A. H.; Amma, E. L. *J. Am. Chem. Soc.* **1974**, *96*, 5407–5413. b) Dias, H. V. R.; Wang, Z.; Jin, W. *Inorg. Chem.* **1997**, *36*, 6205–6215. c) Munakata, M.; Wu, L. P.; Ning, G. L. *Coord. Chem. Rev.* **2000**, *198*, 171–203. d) Lindeman, S. V.; Rathore, R.; Kochi, J. K. *Inorg. Chem.* **2000**, *39*, 5707–5716. e) Maier, J. M.; Jungwun Hwang, P. L.; Smith, M. D.; Shimizu, K. D. *J. Am. Chem. Soc.* **2015**, *137*, 8014–8017.

[6] a) Kuritani, M.; Tashiro, S.; Shionoya, M. *Inorg. Chem.* **2012**, *51*, 1508–1515. b) Kuritani, M.; Tashiro, S.; Shionoya, M. *Chem. Asian J.* **2013**, *8*, 1368–1371.

[7] a) Ke, C.; Destecroix, H.; Crump, M. P.; Davis, A. P. *Nat. Chem.* **2012**, *4*, 718–723. b) Hagiwara, K.; Sei, Y.; Akita, M.; Yoshizawa, M. *Chem. Commun*. **2012**, *48*, 7678–7680. c) Yoshizawa, M.; Klosterman, J. K. *Chem. Soc. Rev.* **2014**, *43*, 1885–1898.

[8] a) Gimeno, M. C.; Laguna, A. In *Comprehensive Coordination Chemistry II*; Fenton, D. E., Eds.; Elsevier: Amsterdam, 2003; Vol. 6, 911–1145. b) Hiraoka, S.; Motoo, S.; Shionoya, M. *J. Am. Chem. Soc.* **2004**, *126*, 1214–1218. c) Hiraoka, S.; Harano, K.; Motoo, S.; Shionoya, M. *Angew. Chem. Int. Ed.* **2005**, *44*, 2727–2731. d) Nakamura, T.; Ube, H.; Shionoya, M. *Angew. Chem. Int. Ed*. **2013**, *52*, 12096–12100.

[9] *Modern Cyclophane Chemistry*; Gleiter, R., Hopf, H., Eds.; WILEY-VCH Verlag GmbH & Co. KGaA: Weinheim, 2004.

[10] a) Crespo, O.; Gimeno, M. C.; Jones, P. G.; Laguna, A.; Sarroca, C. *Chem. Commun.* **1998**, 1481–1482. b) Tsupreva, V. N.; Titov, A. A.; Filippov, O. A.; Bilyachenko, A. N.; Smol'yakov, A. F.; Dolgushin, F. M.; Agapkin, D. V.; Godovikov, I. A.; Epstein, L. M.; Shubina, E. S. *Inorg. Chem.* **2011**, *50*, 3325–3331.

[11] Connelly, N. G.; Geiger, W. E. *Chem. Rev.* **1996**, *96*, 877–910.

[12] Leschke, M.; Lang, H.; Holze, R. *Electrochimica Acta* **2003**, *48*, 919–924.

[13] a) Matsue, T.; Evans, D. H.; Osa, T.; Kobayashi, N. *J. Am. Chem. Soc.* **1985**, *107*, 3411–3417. b) Sun, W.; Kusukawa, T.; Fujita, M. *J. Am. Chem. Soc.* **2002**, *124*, 11570–11571. c) Clever, G. H.; Tashiro, S; Shionoya, M. *Angew. Chem. Int. Ed*. **2009**, *48*, 7010 –7012.

[14] Coulson, D. R. *Inorg. Synth.* **1972**, *13*, 121–124.

[15] Kim, S.; Yang, B.; Ma, Y.; Lee, J.; Park, J. *J. Mater. Chem.* **2008**, *18*, 3376–3384.

[16] a) Sheldrick, G. M. *SHELXL-97*, *Program for refinement of crystal structures*, (University of Göttingen, Göttingen, Germany, 1997). b) Sheldrick, G. M. *SHELXL- 2013*, *Program for refinement of crystal structures*, (University of Göttingen, Göttingen, Germany, 2013).

[17] Spek, A. L. *PLATON*, *A Multipurpose Crystallographic Tool*, (Utrecht University, The Netherlands, 2001).

Chapter 3.

Host-Guest Interaction via Metal-to-Metal Dative Bonding between Mononuclear Ag(I)-Half-Macrocycle and Ruthenocene

3–1. Introduction

As described in Chapter 1, metal ions are widely used as structural motifs of molecular metallo-hosts.[1] In particular, coordination bonding and electrostatic interactions are essential driving forces between transition metal centers and coordinating guest species for guest binding. Metal–metal bonding works as a unique attractive force[2] which provides electronically-coupled supramolecular interactions with unique structures as described in the section 1–4. In this chapter, I describe an alternative host-guest complexation using metal–metal bonding as a driving force for guest binding.

Metallocenes with group 8 metals such as ferrocene ruthenocene, and osmocene have been widely investigated as important building brocks to create functional molecular and supramoleular architectures owing to their chemical versatility, redox reactivity, unique five-hold symmetrical sandwich-shaped structures, and low rotational barrier around Cp–metal bonds.[3,4] Taking advantage of their unique structural characteristics, various kinds of functional molecular architectures have been reported, from molecular machines,[4a,c] foldamers,[4b,e] macrocycles,[4d,f] and supramolecular assemblies.[4g,h] For instance, Aida and co-workers reported a scissor-like molecule possessing a metallocene moiety as a pivot part, which exhibits an open-close motion supported by a free rotational motion around Cp–Fe bonds (Figure 3–1a).[4a] Hirao and co-workers developed metallocene-bearing dipeptides, which enabled unique turn-like structures based on the flexible conformation of Cp–Fe bonds (Figure 3–1b).[4b] Kandel and co-workers recently reported hydrogen bonded two dimensional quasicrystals using ferrocene derivatives with carboxylic groups, which utilize the five-hold symmetrical structure of metallocenes (Figure 3–1c).[4g]

In the light of these examples, investigation of a method to immobilize metallocenes using a non-covalent interaction would help further development of metallocene based molecular architectures. As receptors of metallocenes, several kinds of host molecules like organic macrocycles and molecular capsules or cages have been investigated, which utilize hydrophobic effect or other intermolecular interactions between hosts and functional groups of metallocenes as driving forces (Figure 3–2).[5] However, host molecules which can bind pristine metallocenes in organic solvents have not been extensively studied.

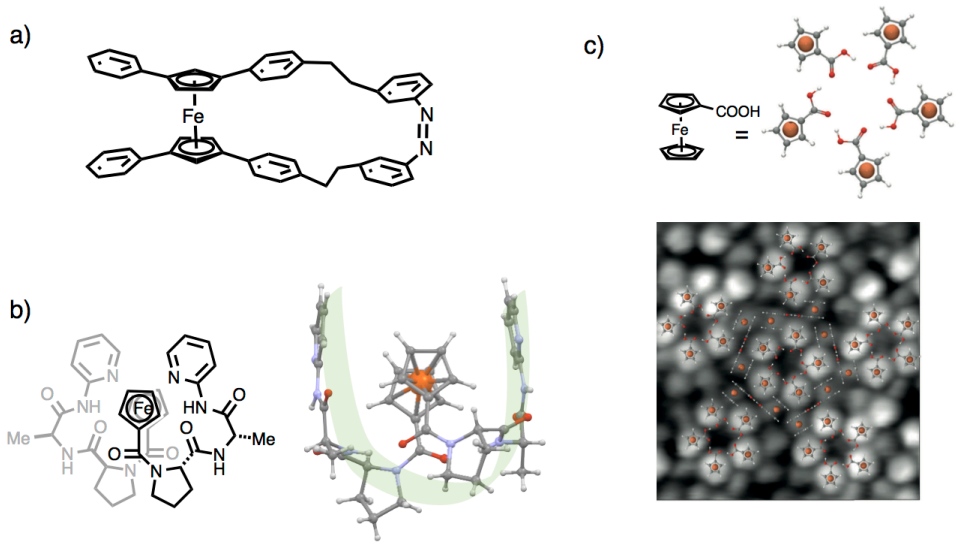

Figure 3–1. Representative examples of molecular or supramolecular architectures containing metallocene moieties. a) Molecular structure of a scissor-like molecule possessing a metallocene moiety as a pivot part,[4a] b) molecular structure and crystal structure of a metallocene-bearing dipeptide,[4b] c) hydrogen bonded two dimensional quasicrystal using ferrocene derivatives with carboxylic groups.[4g] Upper: a plausible structure of hydrogen bonded ferrocene pentamer, Bottom: a scanning tunneling microscope image of resulting quasicrystal. Figure 3–1c is reproduced with permission from *Nature* **2014**, *507*, 86–89,[4g] Copyright 2014 Nature Publishing Group.

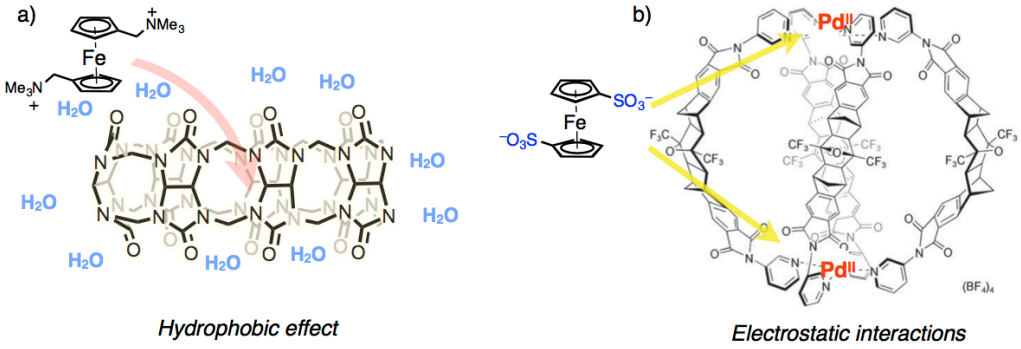

Figure 3–2. Inclusion of metallocene derivatives within a) an organic macrocycle using hydrophobic effect,[5c] b) a self-assembled metallo-cage using electrostatic interactions.[5d] Figure 3–2b is reproduced with permission from *Angew. Chem. Int. Ed.* **2009**, *48*, 7010–7012,[5d] Copyright 2009 Wiely-VCH Verlag GmbH.

With a view to developing novel motifs for metallocene binding, I focused on the Lewis basic character of metallocenes. As described in Chapter 1, metal atoms of group 8 metallocenes work as Lewis bases because of the electron donating effects of occupied e_{2g} orbitals.[6,7] In particular, ferrocenophane, ruthenocene, osmocene, and their derivatives are known to coordinate to several transition metal ions via metal-to-metal dative bonding because of the sterically accessible character of metal centers. Based on this, in this work, I investigated

host-guest complexation behaviors between metallo-host and pristine metallocene using metal-to-metal dative bonding as a driving force (Figure 3–3).

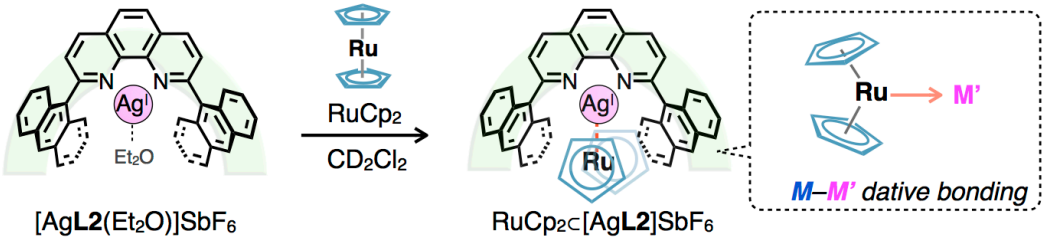

Figure 3–3. Schematic drawing of ruthenocene binding by mononuclear Ag(I)-half-macrocycle [Ag**L2**(Et_2O)]SbF_6 via metal-to-metal dative bonding.

In this chapter, I describe the synthesis and guest binding behaviors of a mononuclear Ag(I)-half-macrocycle [Ag**L2**(Et_2O)]SbF_6 which has a half structure of the dinuclear Ag(I)-macrocycle [Ag_2**L1**X_2]$(SbF_6)_2$ (X = Et_2O or H_2O) described in the previous chapter (Figure 3–3). The anthracene-based nano-space of [Ag**L2**(Et_2O)]SbF_6 equipped with coordinatively labile sites of Ag(I) ion works as strong binding sites for pristine ruthenocene utilizing a Ru–Ag type metal-to-metal dative bonding as characterized by NMR spectroscopy, ESI-TOF mass spectrometry, and single crystal X-ray analysis.

3–2. Design and Synthesis of a Mononuclear Ag(I)-Half-Macrocycle

As a host molecule, a mononuclear Ag(I)-half-macrocycle [Ag**L2**(Et_2O)]SbF_6 was selected which has a fragment structure of the dinuclear Ag(I)-macrocycle [Ag_2**L1**X_2]$(SbF_6)_2$ (X = Et_2O or H_2O) described in the previous chapter (Scheme 3–1). [Ag**L2**(Et_2O)]SbF_6 has an anthracene based nano-space equipped with a solvated Ag(I) ion which is suitable to bind a guest molecule using coordination bonding at the Ag(I) center with the aid of non-covalent interaction with anthracene walls.

[Ag**L2**(Et_2O)]SbF_6 was prepared and isolated in 71% by complexation between already reported phenanthroline-based ligand **L2** and $AgSbF_6$ in $CHCl_3$/acetone, and subsequent crystallization by Et_2O vapor diffusion in the dark (Scheme 3–1).[8] The obtained complex was characterized by single crystal X-ray analysis, NMR spectroscopy, and ESI-TOF mass spectrometry (Figure 3–4–8).

Scheme 3–1. Synthesis of [Ag**L2**(Et_2O)]SbF_6.

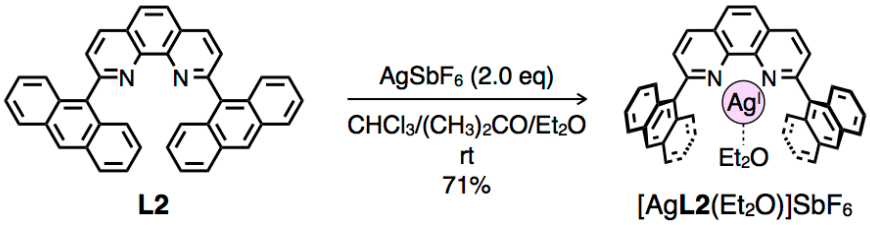

In the crystal structure, one Ag(I) ion is bound by two N-atoms of the phenanthroline of **L2** and one O-atom of solvent (Et_2O) in a trigonal planar coordination geometry (Figure 3–4). Two anthracenes are standing orthogonally to the π-plane of phenanthroline; the dihedral angles between the phenanthroline and adjacent anthracenes were evaluated to be around 75–79º in the crystal to provide an anthracene-based nano-space with solvated Ag(I) ion.

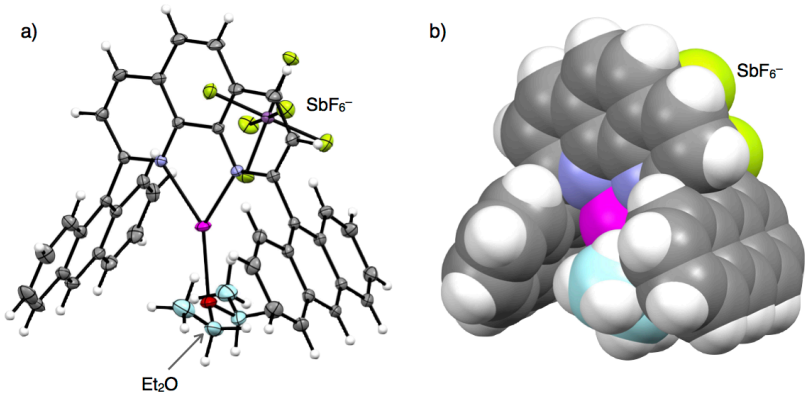

Figure 3–4. Crystal structures of [Ag**L2**(Et_2O)]SbF_6. a) ORTEP view (50% probability level) and b) space filling model. (Ag: magenta, C: grey, C of Et_2O: light blue, F: yellow, H: white, N: blue, O: red, Sb: pink)

The ^{1}H NMR spectrum of the resulting complex showed phenanthroline's signals, which were about 0.2 ppm downfield shifted from the original ligand **L2** because of the effect of the coordination of Ag(I) ions (Figure 3–5). [Ag**L2**(Et_2O)]SbF_6 showed broad signals in the aromatic region, probably due to the fast exchange of the coordinating solvent.

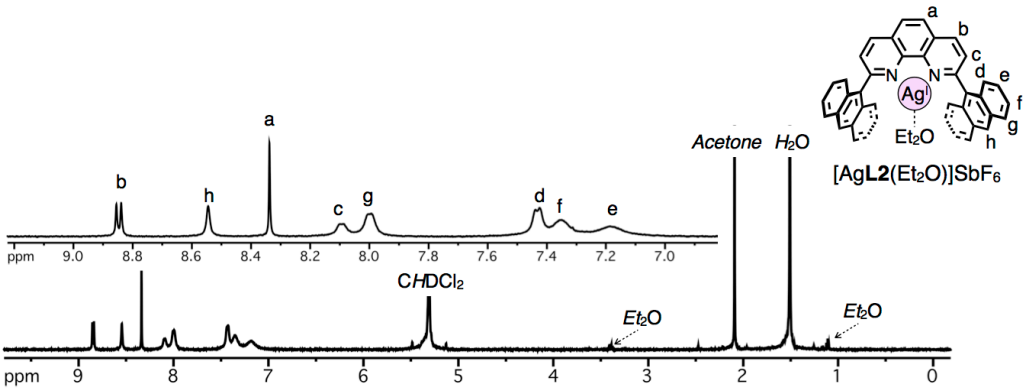

Figure 3–5. ^{1}H NMR spectra of [Ag**L2**(Et_2O)]SbF_6 (500 MHz, CD_2Cl_2, 300 K). Acetone was included during the processes of crystallization.

In solution, the Ag(I) complex of **L2** possibly exists as an equilibrium mixture of *metal free ligand* **L2**, *1:2 complex* [Ag$\mathbf{L2}_2$]$^+$, and *1:1 complex* [Ag**L2**(Et_2O)]$^+$ (Figure 3–6). However, ^{1}H NMR spectrum of [Ag**L2**(Et_2O)]SbF_6 isolated by above-mentioned crystallization (Figure 3–5 and 3–6e) can be assigned as that of a 1:1 complex, and the existence of metal free ligand **L2** and a 1:2 complex [Ag$\mathbf{L2}_2$]$^+$ are almost ignorable in CD_2Cl_2 at 300 K, as was proved by following ^{1}H NMR spectra of a mixture of isolated 1:1 complex [Ag**L2**(Et_2O)]SbF_6 and different amounts of $AgSbF_6$ or **L2** in CD_2Cl_2 (Figure 3–6). With an increase in the amount of Ag(I) for **L2**, aromatic signals of **L2** firstly upfield shifted (0–0.5 eq), and then downfield shifted (0.50–1 eq), which indicates that **L2** existed in equilibrium among **L2**, [Ag$\mathbf{L2}_2$]$^+$ and [Ag**L2**(Et_2O)]$^+$ in the presence of less than 1 eq of Ag(I) in CD_2Cl_2 at 300 K (*see spectral changes from Figure 3–6a to Figure 3–6d*). On the other hand, the chemical shifts of the signals of an isolated sample of [Ag**L2**(Et_2O)]SbF_6 (Figure 3–6e) were almost identical to those of mixtures of isolated [Ag**L2**(Et_2O)]SbF_6 and additional amounts of $AgSbF_6$ (Figure 3–6f,g). This indicates that the shifts of the signals were almost converged in the presence of more than 1 eq of Ag(I) ions. Above-mentioned results suggest that an isolated sample of [Ag**L2**(Et_2O)]SbF_6 exists mainly as a 1:1 complex, and the existence of 1:2 complex [Ag$\mathbf{L2}_2$]$^+$ or metal-free ligand **L2** is ignorable in CD_2Cl_2 at 300 K under this concentration condition (ca. 1 mM).

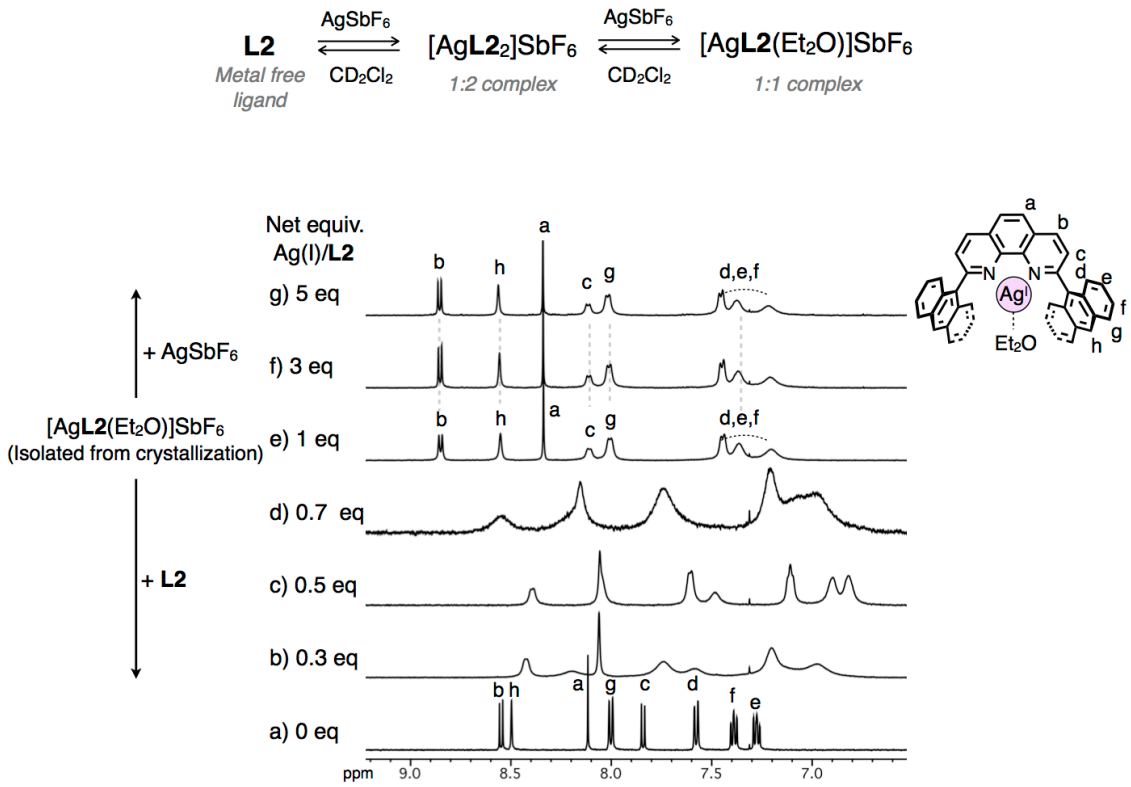

Figure 3–6. a) Partial ^{1}H NMR spectra of a) **L2** and b–g) mixtures of [Ag**L2**(Et_2O)]SbF_6 and different amounts of **L2** or $AgSbF_6$ (500 MHz, CD_2Cl_2, 300 K). b) [[Ag**L2**(Et_2O)]SbF_6]$_0$ = 0.40 mM, [**L2**]$_0$ = 1.1 mM, [$AgSbF_6$]$_0$ = 0 mM, c) [[Ag**L2**(Et_2O)]SbF_6]$_0$ = 0.43 mM, [**L2**]$_0$ = 0.44 mM, [$AgSbF_6$]$_0$ = 0 mM, d) [[Ag**L2**(Et_2O)]SbF_6]$_0$ = 0.44 mM, [**L2**]$_0$ = 0.22 mM, [$AgSbF_6$]$_0$ = 0 mM, e) [[Ag**L2**(Et_2O)]SbF_6]$_0$ = 0.90 mM, [**L2**]$_0$ = 0 mM, [$AgSbF_6$]$_0$ = 0 mM, f) [[Ag**L2**(Et_2O)]SbF_6]$_0$ = 0.90 mM, [**L2**]$_0$ = 0 mM, [$AgSbF_6$]$_0$ = 1.8 mM, g) [[Ag**L2**(Et_2O)]SbF_6]$_0$ = 0.90 mM, [**L2**]$_0$ = 0 mM, [$AgSbF_6$]$_0$ = 3.5 mM. [[Ag**L2**(Et_2O)]SbF_6]$_0$, [**L2**]$_0$, and [$AgSbF_6$]$_0$ indicate the initial concentration of each substance, respectively. The net equivalence of Ag(I)/**L2** was calculated as follows:

Ag(I)/**L2** = ([[Ag**L2**(Et_2O)]SbF_6]$_0$ + [$AgSbF_6$]$_0$)/([[Ag**L2**(Et_2O)]SbF_6]$_0$ + [**L2**]$_0$)

^{1}H NMR spectrum of the isolated [Ag**L2**(Et_2O)]SbF_6 in CD_2Cl_2 at lower temperature (210 K) showed broad and complicated signals which were distinct from those at 300 K (Figure 3–7). Notably, under a more diluted condition (0.2 mM), the broadening was not so remarkable. These results suggest a possibility of some kinds of intermolecular aggregation among [Ag**L2**(Et_2O)]$^+$ in CD_2Cl_2 at low temperatures.

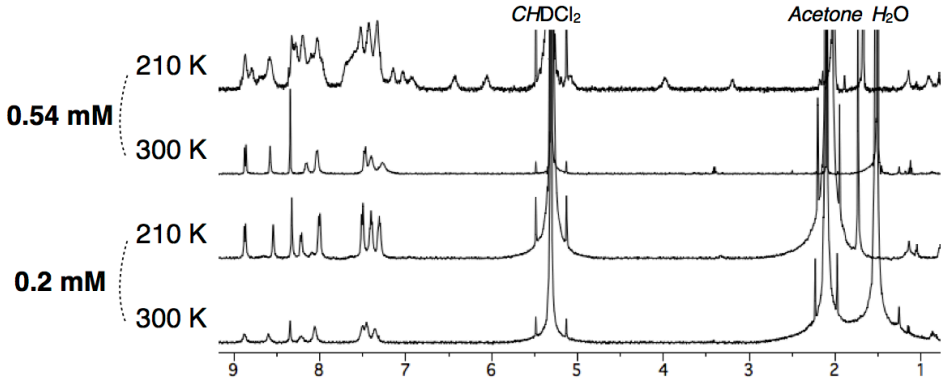

Figure 3–7. ^{1}H NMR spectrum of [Ag**L2**(Et_2O)]SbF_6 measured at different concentrations and temperatures (500 MHz, CD_2Cl_2, 300–220 K).

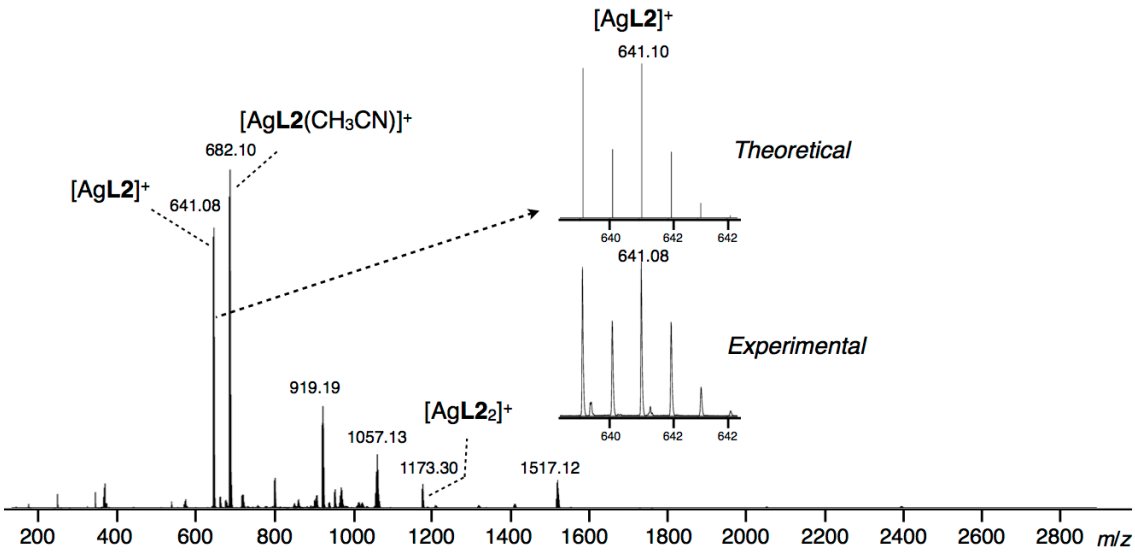

Figure 3–8. ESI-TOF mass spectrum of [Ag**L2**(Et_2O)]SbF_6 in CH_2Cl_2. CH_3CN was contaminated during the measurement.

3–3. Binding of an Organometallic Molecule via Metal-to-Metal Dative Bonding

The nano-space of the mononuclear Ag(I)-half-macrocycle [Ag**L2**(Et_2O)]SbF_6 will be suitable to bind guest molecules using coordination bonding at Ag(I) center with the aid of intermolecular interaction with anthracene walls as driving forces. In this section, I found that [Ag**L2**(Et_2O)]SbF_6 can bind one molecule of ruthenocene ($RuCp_2$) as a pristine organometallic molecule using Ru–Ag type metal-to-metal dative bonding as the main driving force, which was characterized by NMR, ESI-TOF mass and single crystal X-ray analyses.

3–3–1. Binding of ruthenocene by a mononuclear Ag(I)-half-macrocycle

The binding behavior of $RuCp_2$ to [Ag**L2**(Et_2O)]SbF_6 was investigated by ^{1}H NMR titration experiment (Figure 3–9). Upon adding $RuCp_2$ to a solution of [Ag**L2**(Et_2O)]SbF_6 in CD_2Cl_2 at 300 K, signals in the aromatic region showed downfield shift, which indicated that [Ag**L2**(Et_2O)]SbF_6 reacted with $RuCp_2$ to form $RuCp_2$⊂[Ag**L2**]SbF_6. A sharp singlet appeared at 3.26 ppm (H_A in Figure 3–9b) was assigned as the signal of $RuCp_2$ bound to the Ag(I) center of [Ag**L2**(Et_2O)]SbF_6, which was significantly downfield shifted ($\Delta\delta$ = –1.3 ppm) due to the strong shielding effect from the neighboring anthracene walls. In the presence of more than 1.0 eq of $RuCp_2$ (Figure 3–9d), the signals in the aromatic region hardly changed, and signals of both bound and free $RuCp_2$ were observed separately but broadened due to the reversible host-guest binding. The formation of a 1:1 host-guest complex was eventually indicated by ^{1}H NMR spectroscopy at 210 K (Figure 3–10). With increasing amounts of $RuCp_2$, the broad signal was gradually replaced by a new set of sharp signals which can be assigned as C_{2v}-symmetrical host-guest complex, $RuCp_2$⊂[Ag**L2**]SbF_6 (Figure 3–10a–c). The changes in the signals in the aromatic region were converged in the presence of 1.0 eq of $RuCp_2$ (Figure 3–10c). Notably, the ^{1}H NMR signals of bound (H_A) and free $RuCp_2$ were vividly observed as a separate and sharp singlet at 210 K because of the reduced exchange reaction between bound and free $RuCp_2$ (Figure 3–10d). The integral ratio of the signals of bound $RuCp_2$ (H_A) and mononuclear Ag(I)-half-macrocycle ($H_{a–h}$) in the Figure 3–10d clearly suggested the formation of a 1:1 host-guest complex, $RuCp_2$⊂[Ag**L2**]SbF_6.

The formation of a 1:1 host-guest complex was also supported by ESI-TOF mass spectrum of the isolated complex of $RuCp_2$⊂[Ag**L2**]SbF_6 (Figure 3–11).

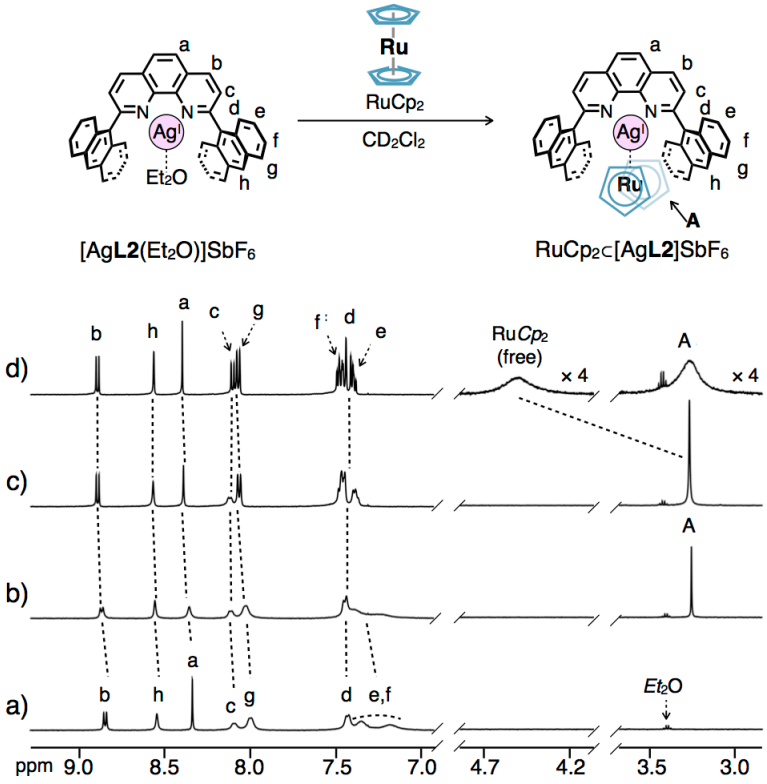

Figure 3–9. Partial ^{1}H NMR spectra of [Ag**L2**(Et_2O)]SbF_6 (1.1 mM) in the presence of a) 0.0, b) 0.5, c) 1.0, and d) 1.5 eq of $RuCp_2$ (500 MHz, CD_2Cl_2, 300 K).

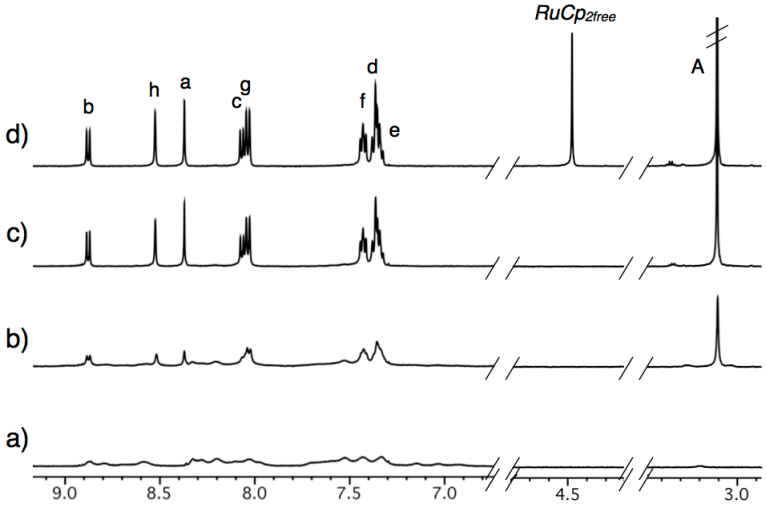

Figure 3–10. Partial ^{1}H NMR spectra of [Ag**L2**(Et_2O)]SbF_6 (0.54 mM) in the presence of a) 0.0, b) 0.5, c) 1.0, and d) 1.5 eq of $RuCp_2$ (500 MHz, CD_2Cl_2, 210 K).

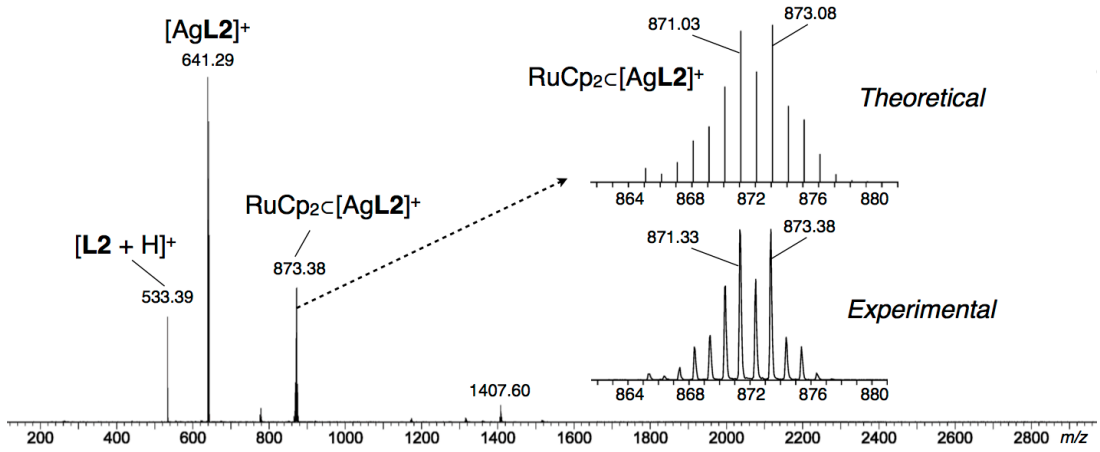

Figure 3–11. ESI-TOF mass spectrum of $RuCp_2⊂[Ag\mathbf{L2}]SbF_6$ in CH_2Cl_2.

The molecular structure of the host-guest complex, $RuCp_2⊂[Ag\mathbf{L2}]SbF_6$, was finally determined by single-crystal X-ray analysis (Figure 3–12). Yellow single crystals of $RuCp_2⊂[Ag\mathbf{L2}]SbF_6·CHCl_3$ were obtained in 43% by standing a mixture of **L2**, 1.6 eq of $AgSbF_6$, and 2.2 eq of $RuCp_2$ in $CHCl_3$/acetone in the dark for a week. In the resulting crystal structure, one molecule of $RuCp_2$ is bound by the Ag(I) center of mononuclear Ag(I)-half-macorocycle $[Ag\mathbf{L2}]^+$ through Ru–Ag dative bonding (Figure 3–12a). The Ag(I) ion formed a trigonal planar coordination geometry with two N-atoms of phenanthroline and one Ru-atom of $RuCp_2$ (Ag–N1 2.338(4) Å; Ag–N2 2.340(4) Å; Ag–Ru 2.782(0) Å; N1–Ag–N2 72.19(9)°; N1–Ag–N2 142.95(6)°; N2–Ag–Ru 144.33(6)°) (Figure 3–12a). The Ru–Ag distance is 2.782(0) Å, which is shorter than the sum of the covalent radii of Ag and Ru (2.91 Å)[9] and in the range of Ru–Ag bond length already reported by Cambridge Crystallographic Database.[10] The distances between Ru and π-planes of Cp were estimated to be ca. 1.83 Å, which are almost identical to that of the original $RuCp_2$ (1.831 Å).[11] Two Cp rings are in an eclipse configuration, though they are no longer parallel and significantly tilted at an angle of ca. 15°. Such a bent structure of metallocene is known to be typical to metal-to-metal dative bonded complexes of metallocenes.[6] In such a bent structure, the occupied d-orbitals (e_{2g}) of the metal center of the metallocene are supposed to project towards the open side, which enables an effective orbital interaction with Lewis acidic transition metals.[7] Beside Ru–Ag interaction, $RuCp_2$ forms CH–π interaction with π-surfaces of the anthracene walls, which might stabilize the host-guest complex (C–π distance: 3.4–3.6 Å, Figure 3–12b,c).

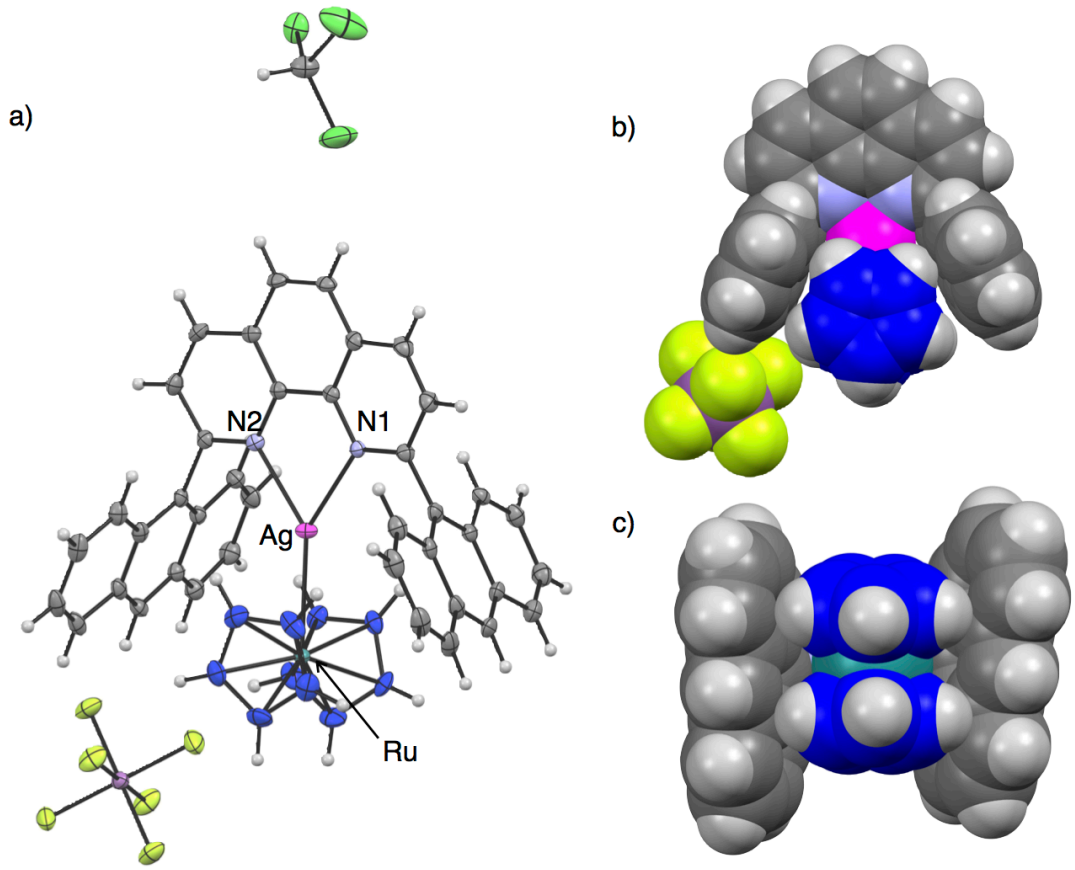

Figure 3–12. Crystal structure of $RuCp_2 \subset [Ag\mathbf{L2}]SbF_6$. a) ORTEP view (50% probability level) of $[Ag\mathbf{L2}(RuCp_2)]SbF_6 \cdot CHCl_3$ and space filling models of $[Ag\mathbf{L2}(RuCp_2)]SbF_6 \cdot CHCl_3$ from b) a front and c) a bottom views. (Ag: magenta, C: grey, C of $RuCp_2$: blue, Cl: pale green, F: yellow, H: white, N: pale blue, O: red, Ru: green, Sb: pink)

The ^{1}H NMR spectrum of the isolated single crystal showed identical signal patterns as that of aforementioned titration experiment, which indicated that the composition of the host-guest complex in solution was the same as that in the crystalline state (Figure 3–13). In the crystal structure, the $RuCp_2$ moiety has a C_{2v}-symmetrical structure due to the desymmetrization by the Ru–Ag bond and the resulting tilting of the structure (Figure 3–12). In contrast, the bound $RuCp_2$ showed only one singlet in the ^{1}H NMR spectrum at 210 K (Figure 3–10d), which corresponds to a D_{5h}-symmetrical structure like the original form of $RuCp_2$. This suggests that the two Cp rings of bound to $RuCp_2$ can rotate quickly around the Cp–Ru bonds in solution at 210 K.

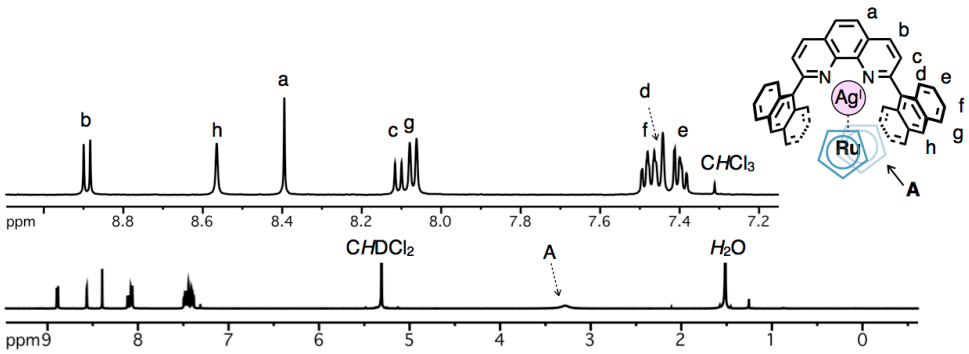

Figure 3–13. ^{1}H NMR spectra of $RuCp_2$⊂[Ag**L2**]SbF_6 isolated as single crystals (500 MHz, CD_2Cl_2, 300 K).

The host-guest complexation behavior between [Ag**L2**(Et_2O)]SbF_6 and $RuCp_2$ was also studied by titration experiments using UV-Vis spectroscopy (Figure 3–14). Upon adding $RuCp_2$ to the solution of [Ag**L2**(Et_2O)]SbF_6 (10 μM) in $CHCl_3$, the spectrum of [Ag**L2**(Et_2O)]SbF_6 slightly changed. The absorption change converged in the presence of less than 5.0 eq of $RuCp_2$. Although the dissociation of Ag(I) ions from [Ag**L2**(Et_2O)]SbF_6 was not ignorable in such a diluted condition which prevents quantitative analyses of the host-guest binding behavior, it should be noted that the slight change in the absorption of [Ag**L2**(Et_2O)]SbF_6 suggests existence of no remarkable charge transfer interaction between Ag(I) center and $RuCp_2$.

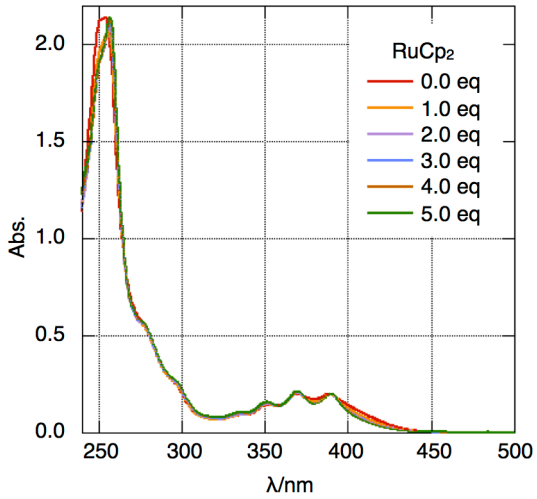

Figure 3–14. a) UV-Vis spectra of the mixtures of [Ag**L2**(Et_2O)]SbF_6 and different amounts of $RuCp_2$ ([[Ag**L2**(Et_2O)]SbF_6] = 10 μM, l = 1.0 cm, 293 K in $CHCl_3$).

3–3–2. The stability of Ru–Ag bonded complex

From the NMR titration experiment mentioned above (Figure 3–9), the binding constant of the host-guest complexation K_a = ([$RuCp_2$⊂[Ag**L2**]$^+$]/([[Ag**L2**(Et_2O)]$^+$][$RuCp_2$]) was estimated to be over 10^4 M^{-1} in CD_2Cl_2 at 300 K. Compared with already reported examples, this value is

one of the largest value to bind non-substituted metallocene in non-polar organic solvents.[12] This indicates a significant availability of metal-to-metal dative bonding to immobilize $RuCp_2$ as a pristine Lewis basic metallocene. To my knowledge, $RuCp_2 \subset [Ag\mathbf{L2}]SbF_6$ is the first well characterized Ru–Ag bonded complex between Ag(I) and $RuCp_2$ derivatives. According to the example reported by Sano and co-workers, a reaction between $RuCp_2$ and solvated Ag(I) yielded unidentified insoluble matter.[6g] Indeed, upon mixing equimolar amounts of $RuCp_2$ and Ag(I) in $CDCl_3/(CD_3)_2CO$ = 90/1, a colorless precipitate was immediately formed with a broadening of the signal of $RuCp_2$ in the ^1H NMR spectrum (Figure 3–15). In contrast, the Ru–Ag bonded host-guest complex $RuCp_2 \subset [Ag\mathbf{L2}]SbF_6$ was stable under this condition as shown in the ^1H NMR spectrum in the dark for several days (Figure 3–9).

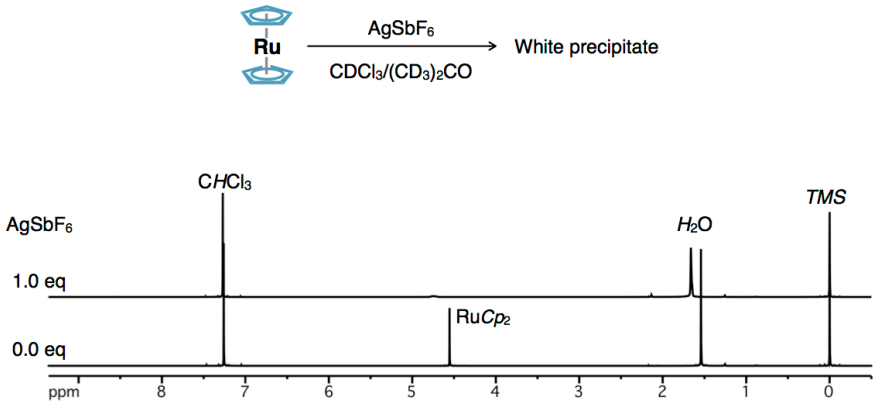

Figure 3–15. ^1H NMR spectra of mixtures of $RuCp_2$ (110 μM) and different amounts of $AgSbF_6$ (500 MHz, $CDCl_3/(CD_3)_2CO$ = 90/0–1, 300 K).

It should be noted that metal–metal bonded complexes of pristine ferrocene ($FeCp_2$) are less common than those of $RuCp_2$ and osmocene because of the larger steric hindrance of Cp rings in its Fe(II) center. Actually, the reaction between $FeCp_2$ and $[Ag\mathbf{L2}(Et_2O)]SbF_6$ in CD_2Cl_2 at 300 K resulted in shift and broadening of the ^1H NMR signals of the host and $FeCp_2$ (Figure 3–16) which are quite distinctive to the case of the complexation with $RuCp_2$ (Figure 3–9). This result possibly suggests occurrences of different types of reactions, such as complexation between $FeCp_2$ and $[Ag\mathbf{L2}(Et_2O)]SbF_6$ at the π-surfaces of Cp rings through Ag–π interaction or redox reaction between $FeCp_2$ and Ag(I) center, which probably reflect the weaker coordination property of the metal center of $FeCp_2$ than that of $RuCp_2$.

Alternative metallo-hosts with different metal centers ($[M\mathbf{L2}X_m]^{n+}$ (M = Zn(II) or Cu(I), X = anion or solvent)) or organic ligand **L2** itself did not show any significant interaction with $RuCp_2$ in $CDCl_3/(CD_3)_2CO$ (Figure 3–17–18). These results suggest that Ru–Ag dative bonding

plays a central role in the binding of $RuCp_2$ with $[Ag\mathbf{L2}(Et_2O)]^+$, whereas CH–π interactions between $RuCp_2$ and the anthracene walls are supportive.

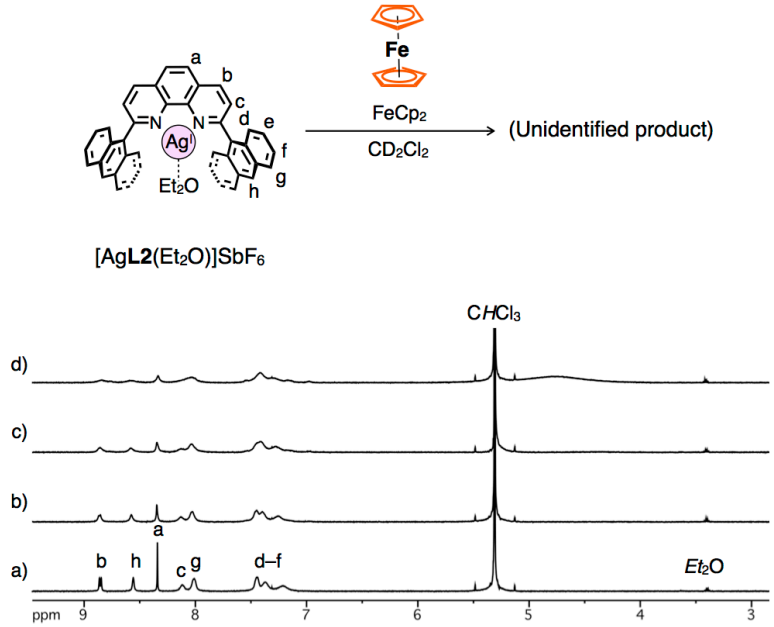

Figure 3–16. Partial ^{1}H NMR spectra of $[Ag\mathbf{L2}(Et_2O)]SbF_6$ (0.8 mM) in the presence of a) 0.0, b) 1.0, c) 2.0, and d) 4.0 eq of $FeCp_2$ (500 MHz, CD_2Cl_2, 300 K).

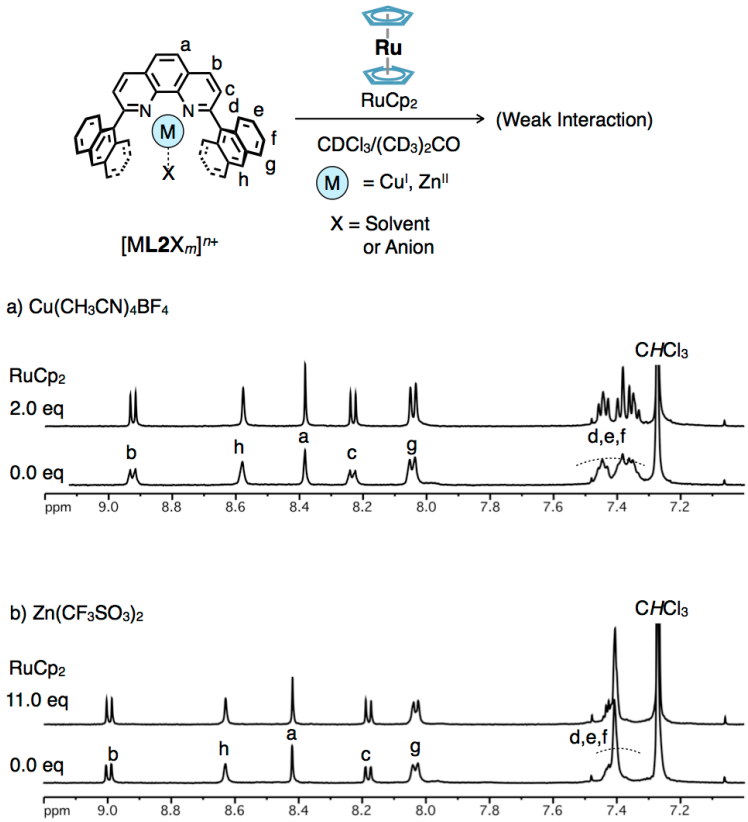

Figure 3–17. Partial ^{1}H NMR spectra of mixtures of **L2**, metal sources (2.0 eq), and different amounts of $RuCp_2$. Metal sources: a) $Cu(CH_3CN)_4BF_4$, (500 MHz, $CDCl_3/(CD_3)_2CO$ = 66/1, 300 K, [**L2**] = 770 μM), b) $Zn(CF_3SO_3)_2$, (500 MHz, $CDCl_3/(CD_3)_2CO$ = 80/1 [**L2**] = 590 μM).

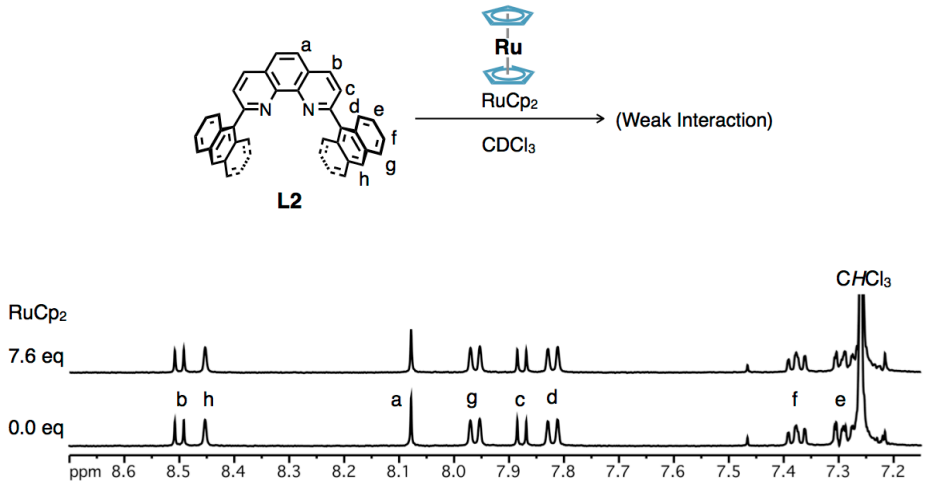

Figure 3–18. Partial ^{1}H NMR spectra of mixtures of **L2** (290 μM) and different amounts of $RuCp_2$ (500 MHz, $CDCl_3$, 300 K).

Above mentioned results lead to a conclusion that the nano-space of [Ag**L2**(Et_2O)]SbF_6 with a coordinatively labile site of solvated Ag(I) centers provides an excellent binding site for $RuCp_2$ as a pristine metallocene with a Lewis basic metal center through Ru–Ag type metal-to-metal dative bonding as a *non*-Werner-type coordination. It should be noted that the reaction between $RuCp_2$ and a dinuclear Ag(I)-macrocycle [Ag_2**L1**X_2]$(SbF_6)_2$ (X = H_2O or Et_2O) in $CDCl_3$ at 300 K resulted in substantial shifts of the ^{1}H NMR signals of the host. Although, the identification of the resulting complex is unsuccessful, this result possibly suggests potential applicability of the metal–metal bonded host-guest complexation behavior of [Ag**L2**(Et_2O)]SbF_6 and $RuCp_2$ to the macrocyclic structure.

3–4. Conclusion

In order to create a novel motif of non-covalently bind metallocenes, a host-guest complexation using metal–metal interaction as a driving force was investigated. As a metallo-host, a mononuclear Ag(I)-half-macrocycle [Ag**L2**(Et_2O)]SbF_6 possessing a nano-space with a solvated Ag(I) ion as Lewis acidic metal center was prepared (Scheme 3–2). [Ag**L2**(Et_2O)]SbF_6 can bind one molecule of Lewis basic metallocene $RuCp_2$ through Ru–Ag type metal-to-metal dative bonding as revealed by NMR, ESI-TOF mass, and single crystal X-ray analyses. The stability constant of this host-guest complexation was estimated to be as large as more than 10^4 M^{-1} in CD_2Cl_2 at 300 K. This value is comparable to those of already reported examples of non-substituted metallocene recognition in non-polar solvents. Notably, this is the first well characterized Ru–Ag bonded complex between Ag(I) and $RuCp_2$ derivatives.

Thus a proper combination of Lewis acidic and basic metal centers would enable construction of host-guest complexes based on metal–metal interactions with certain stability and structural and electronic properties which are specific to the coupled metal atoms.

Scheme 3–2. Formation of a host-guest complex $RuCp_2$⊂[Ag**L2**]SbF_6.

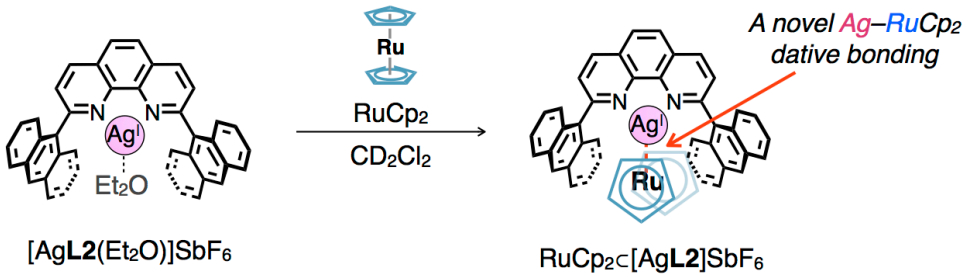

$$K_a = \frac{[\text{Guest}\subset\text{Host}]}{[\text{Host}]\,[\text{Guest}]} > 10^4\ M^{-1}\ (\text{in } CD_2Cl_2 \text{ at } 300\ K)$$

3–5. Experimental

Materials and methods

All solvents, organic and inorganic reagents are commercially available, and were used without further purification. $Pd(PPh_3)_4$,[13a] 2,9-Dichloro-1,10-phenanthroline (**4**),[13b] and anthracen-9-ylboronic acid (**11**)[13c] were synthesized according to previously reported procedures.

NMR spectroscopic measurements were performed using Bruker AVANCE 500 (500 MHz for ^1H, 126 MHz for ^{13}C). NMR spectra were calibrated as below; tetramethylsilane ($Si(CH_3)_4$) = 0 ppm or $CHDCl_2$ = 5.31 ppm for ^1H, CD_2Cl_2 = 53.8 ppm for ^{13}C. *p*-Dimethoxybenzene was used as the internal standard for the calibration of the concentration of samples. ESI-TOF mass spectra were recorded on a Micromass LCT spectrometer. Single-crystal X-ray crystallographic analysis were performed using a Rigaku RAXIS-RAPID imaging plate diffractometer with MoKα radiation, and the obtained data were analyzed using a CrystalStructure crystallographic software package except for refinement, which were performed using SHELXL-97 and SHELXL-2013 programs.[14]

Synthesis of half-macrocyclic ligand L2

Scheme 3–3. Synthetic route for half-macrocyclic ligand **L2**.

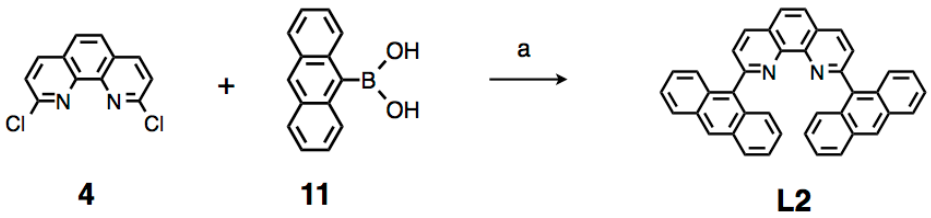

Reagents and conditions: (a) $Pd(PPh_3)_4$, K_3PO_4, DMF, 100 °C (39%).

Compound **4** (330 mg, 1.33 mmol, 1.0 eq), anthracen-9-ylboronic acid (**11**) (730 mg, 3.29 mmol. 2.5 eq), K_3PO_4 (2.06 g, 9.69 mmol, 7.2 eq), and $Pd(PPh_3)_4$ (126 mg, 0.11 mmol, 0.08 eq) were placed in a dried three-neck flask. The inner gas was replaced by argon. Anhydrous DMF (20 mL) was added to the mixture, which was then degassed by a freeze-pump-thaw procedure. The mixture was stirred at 100 °C for 10 h. After cooling down to room temperature, water (200 mL) was added to the mixture, which was extracted with CH_2Cl_2 (ca. 300 mL × 4). The

combined organic layer was dried over Na_2SO_4, and then evaporated under reduced pressure at 80 °C to obtain a yellowish brown solid (0.957 g). The crude product was purified by column chromatography (SiO_2, ϕ = 2.0 cm, h = 2.0 cm, $CHCl_3$), followed by washing the resulting solid with CH_2Cl_2/*n*-hexane = 1/1 to afford **L2** (272 mg, 0.51 mmol, 39%) as a yellow solid.

^{1}H NMR (500 MHz, $CDCl_3$, 300 K): δ (ppm) = 8.49 (d, J = 8.0 Hz, 2H, Ar*H*), 8.45 (s, 2H, Ar*H*), 8.07 (s, 2H, Ar*H*), 7.96 (d, J = 8.5 Hz, 4H, Ar*H*), 7.87 (d, J = 8.0 Hz, 2H, Ar*H*), 7.82 (d, J = 9.0 Hz, 4H, Ar*H*), 7.39–7.36 (m, 4H, Ar*H*), 7.31–7.26 (m, 4H, Ar*H*).

^{13}C NMR (126 MHz, $CDCl_3$, 300 K): δ (ppm) = 158.7, 146.7, 135.9, 135.6, 131.4, 130.4, 128.3, 127.9, 127.7, 127.2, 126.8, 126.4, 125.5, 124.9.

ESI-TOF mass: calcd. for $[C_{40}H_{24}N_2 + H]^+$: m/z = 533.25, found m/z = 533.20.

IR(ATR): ν (cm^{-1}) = 3044, 2360, 1490, 1194, 912, 887, 863, 847, 799, 727, 615.

M.p.: > 450 °C (decomp.)

Synthesis of mononuclear Ag(I)-half-macrocycle [AgL2(Et_2O)]SbF_6

Compound **L2** (18.8 mg, 35.5 μmol, 1.0 eq) placed in a test tube was dissolved in $CHCl_3$ (2.0 mL). A solution of $AgSbF_6$ in acetone (80 mM, 890 μL, 71.2 μmol, 2.0 eq) was added to the solution. The resulting clear yellow solution was immediately concentrated to a volume of about 1.5 mL by evaporation under reduced pressure, and the resulting yellow clear solution was filtered. Yellow needle crystals suitable for single-crystal XRD measurement were obtained by recrystallization from the solution by vapor diffusion of diethyl ether in the dark for 2 days at room temperature. To isolate the title complex as a solid, the crystals were collected by decantation, and then washed with diethyl ether (ca. 0.5 mL × 4). After being kept in the dark for several days, [Ag**L2**(Et_2O)]SbF_6 was obtained as a yellow solid (24.1 mg, 25.4 μmol, 71.4%).^{1}H NMR (500 MHz, CD_2Cl_2, 300 K): δ (ppm) = 8.84 (d, J = 8.0 Hz, 2H, Ar*H*), 8.55 (s, 2H, Ar*H*), 8.34 (s, 2H, Ar*H*), 8.13–7.95 (br, 6H, Ar*H*), 7.49–7.09 (br, 12H, Ar*H*).

^{13}C NMR (126 MHz, CD_2Cl_2, 300 K): δ (ppm) = 158.3, 142.7, 140.0, 134.0, 131.3, 130.3, 130.0, 129.4, 129.2, 128.8, 128.0, 125.6, 124.0 (only 13 signals of the ^{13}C of **L2** frame were observed probably due to the broadening and overlapping of the signals).

IR (ATR): ν (cm^{-1}) = 1686, 1584, 1497, 1443, 1407, 1357, 1234, 1198, 1147, 890, 873, 845, 790, 753, 735, 654, 629.

ESI-TOF MS: calcd. for $[AgC_{40}H_{24}N_2]^+$: m/z = 641.08, found m/z = 641.10.

Elemental analysis: calcd. for $C_{44}H_{34}AgF_6N_2OSb$ ([Ag**L2**(Et_2O)]SbF_6): C, 55.61; H, 3.61; N, 2.95. Found: C, 55.48; H, 3.87; N, 2.73.

Crystal data of [AgL2(Et$_2$O)]SbF$_6$

Crystal data for $C_{44}H_{34}AgF_6N_2OSb$: F_w = 950.37, crystal dimensions 0.40 × 0.20 × 0.20 mm, triclinic, space group *P*–1, *a* = 11.8793(3), *b* = 12.7449(4), *c* = 13.1635(4) Å, α = 90.923(1), β = 94.7179(9), γ = 100.3499(9)°, *V* = 1952.9(1) Å^3, *Z* = 2, ρ_{calcd} = 1.616 gcm^{-3}, μ = 1.2559 mm^{-1}, *T* = 98 K, λ(MoKα) = 0.71075 Å, $2\theta_{max}$ = 54.9°, 18871/8762 reflection collected/unique (R_{int} = 0.0149), R_1 = 0.0196 ($I > 2\sigma(I)$), wR_2 = 0.0757 (for all data), GOF = 1.150, largest diff. peak and hole 0.50/–0.61 eÅ^{-3}. CCDC deposit number 1026280.

Investigation of the complexation behavior between L2 and AgSbF$_6$ in CD$_2$Cl$_2$ at 300 K

Reaction of [AgL2(Et$_2$O)]SbF$_6$ and AgSbF$_6$ in CD$_2$Cl$_2$

To a solution of [Ag**L2**(Et$_2$O)]SbF$_6$ in CD$_2$Cl$_2$ (0.90 mM, 450 μL, 0.41 μmol, 1.0 eq) was added a solution of AgSbF$_6$ in CD$_2$Cl$_2$ (200 mM).

Reaction of [AgL2(Et$_2$O)]SbF$_6$ and L2 in CD$_2$Cl$_2$

To a solution of [Ag**L2**(Et$_2$O)]SbF$_6$ in CD$_2$Cl$_2$ (0.45 mM, 400 μL, 0.18 μmol, 1.0 eq) was added a solution of **L2** in CD$_2$Cl$_2$ (12.0 mM).

Complexation of [AgL2(Et$_2$O)]SbF$_6$ and RuCp$_2$

^{1}H NMR titration experiment at 300 K

To a solution of [Ag**L2**(Et$_2$O)]SbF$_6$ in CD$_2$Cl$_2$ (1.1 mM, 450 μL, 0.49 μmol, 1.0 eq) was added a solution of RuCp$_2$ in CD$_2$Cl$_2$ (150 mM).

Estimation of the stability constant K_a

The stability constant for RuCp$_2$ binding (K_a) was defined as shown below.

$$K_a = \frac{[RuCp_2 \subset [Ag\mathbf{L2}]^+]}{[[Ag\mathbf{L2}(Et_2O)]^+]\,[RuCp_2]}$$

When 0.3 eq of RuCp$_2$ was added to a solution of [Ag**L2**(Et$_2$O)]SbF$_6$ (1.1 mM) in CD$_2$Cl$_2$, no signals corresponding to free RuCp$_2$ were observed, which indicates quantitative binding of RuCp$_2$ by [Ag**L2**(Et$_2$O)]$^+$ (Figure 3–9b). Then, assuming that less than 97% of RuCp$_2$ was bound by [Ag**L2**(Et$_2$O)]$^+$ under this condition, the concentrations of the guest or complexes can

be estimated as shown below.

$$[RuCp_2 \subset [Ag\mathbf{L2}]^+] > 0.32\ mM$$

$$[RuCp_2] < 10\ \mu M$$

$$[[Ag\mathbf{L2}(Et_2O)]^+] < 0.78\ mM$$

Here, K_a can be estimated as below.

$$K_a = \frac{[RuCp_2 \subset [Ag\mathbf{L2}]^+]}{[[Ag\mathbf{L2}(Et_2O)]^+][RuCp_2]}$$

$$> 4.1 \times 10^4\ M^{-1} \quad (\text{at } 300\ K \text{ in } CD_2Cl_2)$$

^{1}H NMR titration experiment at 210 K

To a solution of [Ag**L2**(Et_2O)]SbF_6 in CD_2Cl_2 (0.54 mM, 500 μL, 0.27 μmol, 1.0 eq) was added a solution of $RuCp_2$ in CD_2Cl_2 (50 mM).

Titration experiment using UV-Vis spectroscopy

To a solution of [Ag**L2**(Et_2O)]SbF_6 in $CHCl_3$ (10 μM, 3.5 mL, 0.035 μmol, 1.0 eq) was added a solution of $RuCp_2$ in $CHCl_3$ (17.5 mM).

Crystallization of $RuCp_2 \subset [AgL2]SbF_6$

Compound **L2** (5.93 mg, 11.3 μmol, 1.0 eq) placed in a test tube was dissolved in $CHCl_3$ (3.00 mL). A solution of $AgSbF_6$ in acetone (100 mM, 180 μL, 18.0 μmol, 1.6 eq) was added to the solution. The resulting clear yellow solution was immediately concentrated to a volume of about 1.5 mL by evaporation under reduced pressure. To the resulting solution was added $RuCp_2$ (5.74 mg, 24.8 μmol, 2.2 eq) to form a clear yellow solution with a colorless precipitate. The resulting precipitate was removed by filtration, and then, the resulting filtrate was left in the dark for a week to obtain yellow block crystals suitable for single-crystal XRD measurement. The crystals were collected by decantation, and then washed with diethyl ether (ca. 1 mL × 3). After being kept under vacuum, $RuCp_2 \subset [Ag\mathbf{L2}]SbF_6 \cdot CHCl_3 \cdot 3H_3O$ (5.66 mg, 4.42 μmol, 39.1%) was isolated as a pale orange crystalline solid.

^{1}H NMR (500 MHz, CD_2Cl_2, 300 K): δ (ppm) = 8.89 (d, J = 8.5 Hz, 2H, Ar*H*), 8.57 (s, 2H, Ar*H*), 8.40 (s, 2H, Ar*H*), 8.11 (d, J = 8.0 Hz, 2H, Ar*H*), 8.07 (d, J = 8.5 Hz, 4H, Ar*H*), 7.49–7.38 (m, 10H, Ar*H*), 3.26 (s, 10H, Ar*H*).

^{13}C NMR (126 MHz, CD_2Cl_2, 300 K): δ (ppm) = 159.8, 143.2, 140.0, 134.4, 131.6, 130.5, 129.4, 129.2, 129.2, 128.8, 128.2, 127.8, 126.4, 125.2, 68.8.

IR (ATR): ν (cm^{-1}) = 1199, 1145, 1099, 1010, 995, 900, 869, 837, 825, 792, 753, 737, 622, 613.

ESI-TOF mass: calcd. for $[AgC_{50}H_{34}N_2Ru]^+$: *m/z* = 873.08, found *m/z* = 873.38.

Elemental analysis: calcd. for $C_{51}H_{41}AgF_6N_2O_3RuSb$ ($RuCp_2 \subset [Ag\mathbf{L2}]SbF_6 \cdot CHCl_3 \cdot 3H_3O$): C, 47.82; H, 3.23; N, 2.19. Found: C, 47.88; H, 3.04; N, 2.09.

Crystal data of $RuCp_2 \subset [AgL2]SbF_6 \cdot CHCl_3$

Crystal data for $C_{51}H_{35}AgCl_3F_6N_2RuSb$, F_w = 1226.89, crystal dimensions 0.5 × 0.5 × 0.3 mm, monoclinic, space group $P2_1$ a = 9.1876(4), b = 23.1619(8), c = 10.8521(5) Å, β = 103.676(2)°, V = 2243.9(2) Å^3, Z = 2, ρ_{calcd} = 1.816 gcm^{-3}, μ = 1.603 mm^{-1}, T = 101 K, λ(MoKα) = 0.71075 Å, $2\theta_{max}$ = 54.9°, 22050/10076 reflection collected/unique (R_{int} = 0.0187), R_1 = 0 .0229 ($I > 2\sigma(I)$), wR_2 = 0.0606 (for all data), GOF = 1.048, largest diff. peak and hole 1.62 /-0.86 eÅ^{-3}, Flack parameter = 0.623(5). CCDC deposit number 1415267.

Control experiments

Complexation of $RuCp_2$ and $AgSbF_6$

To a solution of $RuCp_2$ in $CDCl_3$ (110 µM, 455 µL, 0.50 µmol, 1.0eq) was added a solution of $AgSbF_6$ in $(CD_3)_2CO$ (100 mM) to form a colorless precipitate. NOTE: As the solubility of the $AgSbF_6$ in $CDCl_3$ was low, $AgSbF_6$ was added as a solution in $(CD_3)_2CO$.

Complexation of $[AgL2(Et_2O)]SbF_6$ and $FeCp_2$

To a solution of $[Ag\mathbf{L2}(Et_2O)]SbF_6$ in CD_2Cl_2 (0.8 mM, 400 µL, 0.32 µmol, 1.0 eq) was added a solution of $FeCp_2$ in CD_2Cl_2 (110 mM).

Complexation of half-macrocyclic ligand L2 and $RuCp_2$

To a solution of **L2** in $CDCl_3$ (290 µM, 450 µL, 0.13 µmol, 1.0 eq) was added a solution of $RuCp_2$ in $CDCl_3$ (100 mM).

Complexation of metallo-half-macrocycles $[ML2X_m]^{n+}$ (M = Zn(II) or Cu(I), X = anion or solvent) and $RuCp_2$

· Mononuclear Cu(I)-half-macrocycle

To a solution of **L2** in $CDCl_3$ (770 µM, 450 µL, 0.35 µmol, 1.0 eq) was added a solution of $Cu(CH_3CN)_4BF_4$ in $(CD_3)_2CO$ (100 mM, 6.8 µL, 0.68 µmol, 1.9 eq). To the mixture was added a solution of $RuCp_2$ in $CDCl_3$ (100 mM). NOTE: as the solubility of the $Cu(CH_3CN)_4(BF_4)_2$ in

$CDCl_3$ was low, $Cu(CH_3CN)_4(BF_4)_2$ was added as a solution in $(CD_3)_2CO$.

· *Mononuclear Zn(II)-half-macrocycle*

To a solution of **L2** in $CDCl_3$ (590 μM, 450 μL, 0.26 μmol, 1.0 eq) was added a solution of $Zn(CF_3SO_3)_2$ in $(CD_3)_2CO$ (100 mM, 5.6 μL, 0.56 μmol, 2.2 eq). To the mixture was added a solution of $RuCp_2$ in $CDCl_3$ (100 mM). NOTE: as the solubility of the $Zn(CF_3SO_3)_2$ in $CDCl_3$ was low, $Zn(CF_3SO_3)_2$ was added as a solution in $(CD_3)_2CO$.

3–5. References

[1] a) Amendola, V.; Fabbrizzi, L.; Mangano, C.; Pallavicini, P.; Poggi, A.; Taglietti, A. *Coord. Chem. Rev.* **2001**, *219–221*, 821–837. b) Kersting, B.; Lehmann, U. *Adv. Inorg. Chem.* **2009**, *61*, 407–470. c) Amouri, H.; Desmarets, C.; Moussa, J. *Chem. Rev.* **2012**, *112*, 2015–2041. d) Gramage-Doria, R.; Armspach, D.; Matt, D. *Coord. Chem. Rev.* **2013**, *257*, 776–816. e) Durola, F.; Heitz, V.; Reviriego, F.; Roche, C.; Sauvage, J.-P.; Sour, A.; Trolez, Y.; *Acc. Chem. Res*. **2014**, *47*, 633–645. f) McConnell, A. J.; Wood, C. S.; Neelakandan, P. P.; Nitschke, J. R. *Chem. Rev.* **2015**, *115*, 7729–7793.

[2] a) Krogmann, K. *Angew. Chem. Int. Ed.* **1969**, *8*, 35–42. b) Pyykkö, P. *Chem. Rev.* **1997**, *97*, 597–636. c) Ito, T.; Kajiwara, T.; in *Metal Assembled Complexes*; Okawa, H.; Ito T. Eds.; Kagaku Dojin, Kyoto, **2003**, p.3–10 (Japanese). d) 佐々木陽一; 石谷治 編,「金属錯体の光化学」三共出版株式会社, 2007. e) Katz, M. J.; Sakai, K.; Leznoff, D. B. *Chem. Soc. Rev.* **2008**, *37*, 1884–1895. f) Sculfort, S.; Braunstein, P. *Chem. Soc. Rev.* **2011**, *40*, 2741–2760. g) Díez, Á.; Lalinde, E.; Moreno, M. T. *Coord. Chem. Rev.* **2011**, *255*, 2426–2447. h) Bauer, J.; Braunschweig, H.; Dewhurst, R. D. *Chem. Rev.* **2012**, *112*, 4329–4346. i) Krogman, J. P.; Thomas, C. M. *Chem. Commun*. **2014**, *50*, 5115–5127. j) Schmidbaur, H.; Schier, A. *Angew. Chem. Int. Ed.* **2015**, *54*, 746–784.

[3] a) Droege, M. W.; Harman, W. D.; Taube, H. *Inorg. Chem.* **1987**, *26*, 1309–1315. b) *Metallocenes*; Togni, A., Halterman, R. L., Eds.; WILEY-VCH Verlag GmbH & Co. KGaA: Weinheim, 1998. c) *Supramolecular Electrochemistry*; Kaifer, A., Gómez-Kaifer, M., Eds.; WILEY-VCH Verlag GmbH & Co. KGaA, 1999. d) Swarts, J. C.; Nafady, A.; Roudebush, J. H.; Trupia, S.; Geiger, W. E. *Inorg. Chem.* **2009**, *48*, 2156–2165. e) Russell, A. D.; Gilroy, J. B.; Lam, K.; Haddow, M. F.; Harvey, J. N.; Geiger, W. E.; Manners, I. *Chem. Eur. J.* **2012**, *18*, 8000–8003.

[4] a) Muraoka, T.; Kinbara, K.; Kobayashi, Y.; Aida, T. *J. Am. Chem. Soc.* **2003**, *125*, 5612–5613. b) Moriuchi, T.; Nagai, T.; Hirao, T. *Org. Lett.* **2006**, *8*, 31–34. c) Muraoka, T.; Kinbara, K.; Aida T., *Nature* **2006**, *440*, 512–515. d) Mizuta, T.; Aotani, T.; Imamura, Y.; Kubo, K.; Miyoshi, K. *Organometallics* **2008**, *27,* 2457–2463. e) Siebler, D.; Förster, C.; Heinze, K. *Dalton Trans.* **2011**, *40*, 3558–3575. f) Grocka, I.; Latos-Grażyński, L.; Stępień, M. *Angew. Chem. Int. Ed*. **2013**, *52*, 1044–1048. g) Wasio, N. A.; Quardokus, R. C.; Forrest, R. P.; Lent, C. S.; Corcelli, S. A.; Christie, J. A.; Henderson, K. W.; Kandel S. A. *Nature* **2014**, *507*, 86–89. h) Fukino, T.; Joo, H.; Hisada, Y.; Obana, M.; Yamagishi, H.; Hikima, T.; Takata, M.; Fujita, N.; Aida, T. *Science* **2014**, *344*, 499–504.

[5] a) Matsue, T.; Evans, D. H.; Osa, T.; Kobayashi, N. *J. Am. Chem. Soc.* **1985**, *107*, 3411–3417. b) Sun, W.; Kusukawa, T.; Fujita, M. *J. Am. Chem. Soc.* **2002**, *124*, 11570–11571. c) Rekharsky, M. V.; Mori, T.; Yang, C.; Ho Ko, Y.; Selvapalam, N.; Kim, H.; Sobransihgj, D.; Kaifer, A. E.;Liu, S. Isaacs, L.; Chen, W.; Moghaddam, S.; Gilson, M. K.; Kim, K.; Inoue, Y. *Proc. Natl. Acad. Sci.* **2007**, *104*, 20737–20742. d) Clever, G. H.; Tashiro, S; Shionoya, M. *Angew. Chem. Int. Ed*. **2009**, *48*, 7010 –7012.

[6] a) Rosenblum, M.; Santer, J. O.; Howells W. G., *J. Am. Chem. Soc.* **1963**, *85*, 1450–1458. b) Hendrickson, D. N.; Sohn, Y. S.; Morrison, W. H.; Gray, H. B. *Inorg. Chem.* **1972**, *11*, 808–811. c) Morrison, W. H.; Hendrickson, D. N. *Inorg. Chem.* **1972**, *11*, 2912–2917. d) Mann, K. R.; Morrison, W. H.; Hendrichson, D. N. *Inorg. Chem.* **1974**, *13*, 1180–1185. e) Akabori, S.; Sato, S.; Kawazoe, K.; Tamura, C.; Sato, M.; Habata, Y. *Chem. Lett.* **1987**, 1783–1786. f) Watanabe, M.; Masuda, Y.; Motoyama, I.; Sano, H. *Bull. Chem. Soc. Jpn.* **1988**, *61*, 827–833. g) Watanabe, M.; Sano, H. *Bull. Chem. Soc. Jpn.* **1990**, *63*, 1455–1461. h) Sato, S.; Sato, M.; Akabori, S. *Bull. Chem. Soc. Jpn.* **1989**, *62*, 532–538. i) Sato, S.; Habata, Y.; Sato, M.; Akabori, S. *Bull. Chem. Soc. Jpn.* **1989**, *62*, 3963–3967. j) Watanabe, M.; Nagasawa, A.; Sato, M.; Motoyama, I.; Takayama, T. *Bull. Chem. Soc. Jpn.* **1998**, *71*, 1071–1079. k) Enders, M.; Kohl, G.; Pritzkow, H. *Organometallics* **2002**, *21,* 1111–1117. l) Bianchini, C.; Meli, A.; Oberhauser, W.; Parisel, S.; Gusev, O. V.; Kal'sin, A. M.; Vologdin, N. V.; Dolgushin, F. M. *J. Mol. Catal. A* **2004**, *224*, 35–49. m) Metallinos, C.; Tremblay, D.; Barrett, F. B.; Taylor, N. J. *J. Organomet. Chem.* **2006**, *691*, 2044–2047. n) Green, A. G.; Kiesz, M. D.; Oria, J. V.; Elliott, A. G.; Buechler, A. K.; Hohenberger, J.; Meyer, K.; Zink, J. I.; Diaconescu, P. L. *Inorg. Chem.* **2013**, *52*, 5603−5610. o) Gramigna, K. M.; Oria, J. V.; Mandell, C. L.; Tiedemann, M. A.; Dougherty, W. G.; Piro, N. A.; Kassel, W. S.; Chan, B. C.; Diaconescu, P. L.; Nataro, C. *Organometallics* **2013**, *32*, 5966−5979.

[7] Green, J. C. *Chem. Soc. Rev.* **1998**, *27*, 263–271.

[8] Schmittel, M.; Michel, C.; Liu, S.-X.; Schildbach, D.; Fenske, D. *Eur. J. Inorg. Chem.* **2001**, 1155–1166.

[9] Cordero, B.; Gómez, V.; Platero-Prats, A. E.; Revés, M.; Echeverría, J.; Cremades, E.; Barragán, F.; Alvarez, S. *Dalton Trans.* **2008**, 2832–2838.

[10] Cambridge Crystallographic Database, release 2014.

[11] Hardgrove, G. L.; Templeton, D. H. *Acta Cryst.* **1959**, *12*, 28–32.

[12] a) Xia, W.; Hu, X.; Chen. Y.; Lin, C.; Wang, L. *Chem. Commun.* **2013**, *49*, 5085–5087. b) Omoto, K.; Tashiro, S.; Kuritani, M.; Shionoya, M. *J. Am. Chem. Soc.* **2014**, *136*, 17946−17949.

[13] a) Coulson, D. R. *Inorg. Synth.* **1972**, *13*, 121–124. b) Kuritani, M.; Tashiro, S.; Shionoya, M. *Inorg. Chem.* **2012**, *51*, 1508–1515. c) Nomura, H.; Kodama, H.; Ushikubo, T.; Shitagaki, S.; Kawakami, S.; Seo, S. *U. S. Pat. Appl. Publ.*, 20100244673, 30th Sep. **2010**.

[14] a) Sheldrick, G. M. *SHELXL-97*, *Program for refinement of crystal structures*, (University of Göttingen, Göttingen, Germany, 1997). b) Sheldrick, G. M. *SHELXL- 2013*, *Program for refinement of crystal structures*, (University of Göttingen, Göttingen, Germany, 2013).

Chapter 4.

Concluding Remarks

With a purpose to developing novel motifs for host-guest systems based on *non*-Werner type coordination, a dinuclear Ag(I)-macrocycle and a mononuclear Ag(I)-half-macrocycle which have anthracene-based nano-spaces equipped with coordinatively labile sites of Ag(I) ions have been designed and synthesized. In this research, their guest binding behaviors through *non*-Werner type coordination: Ag–π interactions and Ag–Ru type metal-to-metal dative bonding were investigated.

In **Chapter 2**, I described synthesis of a dinuclear Ag(I)-macrocycle $[Ag_2\mathbf{L1}X_2](SbF_6)_2$ (X = Et_2O or H_2O), which has four anthracenes and two Ag(I) ions on its covalently-linked cyclic skeleton. $[Ag_2\mathbf{L1}X_2](SbF_6)_2$ provides a confined nano-space arranged with coordinatively labile sites of two Ag(I) ions directing towards inside the nano-space. Utilizing Ag–π interaction as a driving force, $[Ag_2\mathbf{L1}X_2](SbF_6)_2$ and its $CF_3SO_3^-$ salt can bind several kinds of aromatic molecules like *p*-xylenes, anthracene, [2.2]paracyclophane (pCp), or ferrocene ($FeCp_2$) derivatives in solution and/or in the solid state as revealed by NMR, ESI-TOF mass and single crystal X-ray analyses (Figure 4–1). The affinities of $[Ag_2\mathbf{L1}X_2](SbF_6)_2$ towards anthracene, pCp, and $FeCp_2$ were particularly high so that the binding constants were estimated to be as large as $K_a = 10^4$–10^9 M^{-1} in $CDCl_3$ at 300 K (K_a = [Guest⊂Host]/([Guest][Host]) M^{-1}). In these cases, structures of the guest molecules are suitable to form Ag–π interactions at both sides of Ag(I) ions arranged on the nano-space as revealed by single crystal X-ray analyses. These results suggest that multiple Ag–π interactions work as driving force for such strong host-guest interactions. Moreover, electrochemical measurements revealed that the redox reactivity of included $FeCp_2$ within $[Ag_2\mathbf{L1}X_2](SbF_6)_2$ was markedly changed due to the cationic character of the neighboring Ag(I) ions.

In **Chapter 3**, host-guest interactions driven by metal-to-metal dative bonding was investigated using a mononuclear Ag(I)-half-macrocycle $[Ag\mathbf{L2}(Et_2O)]SbF_6$, which has a nano-space arranged with a solvated Ag(I) ion as a Lewis acidic metal center (Figure 4–2). NMR, ESI-TOF mass, and single crystal X-ray analyses revealed that $[Ag\mathbf{L2}(Et_2O)]SbF_6$ can bind one molecule of ruthenocene ($RuCp_2$) as a Lewis basic pristine metallocene through Ru–Ag type metal-to-metal dative bonding. The binding constant of the host-guest complexation (K_a = [Guest⊂Host]/([Guest][Host]) M^{-1}) was estimated to be over 10^4 M^{-1} in CD_2Cl_2 at 300 K, which is comparable to those of already reported examples of non-substituted metallocene recognition in non-polar solvents.

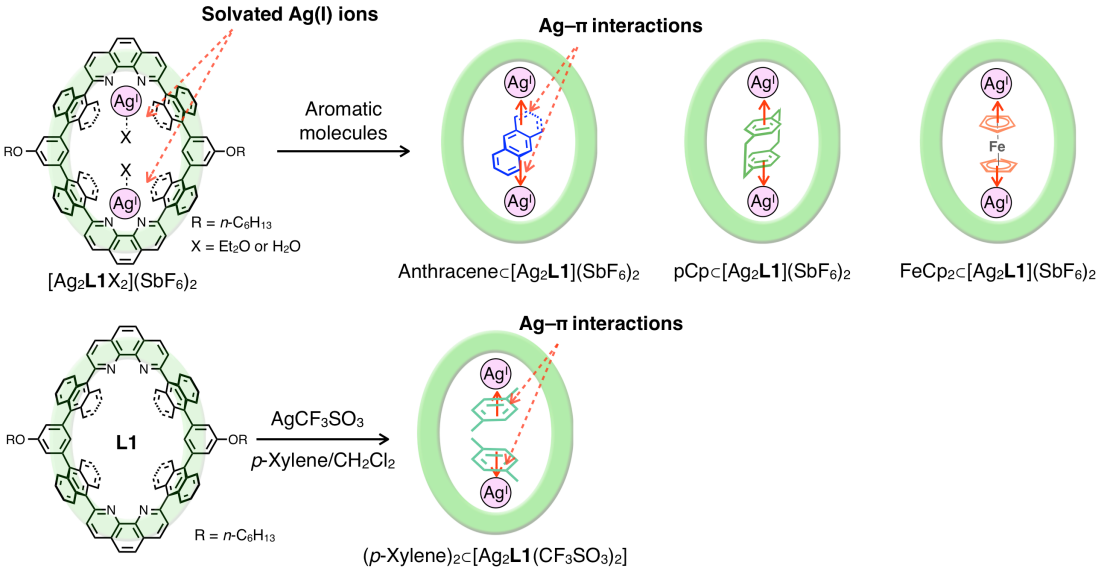

Figure 4–1. Host-guest complexation between a dinucear Ag(I)-macrocycle $[Ag_2\mathbf{L1}X_2](SbF_6)_2$ or its $CF_3SO_3^-$ salt with aromatic molecules via Ag–π interactions.

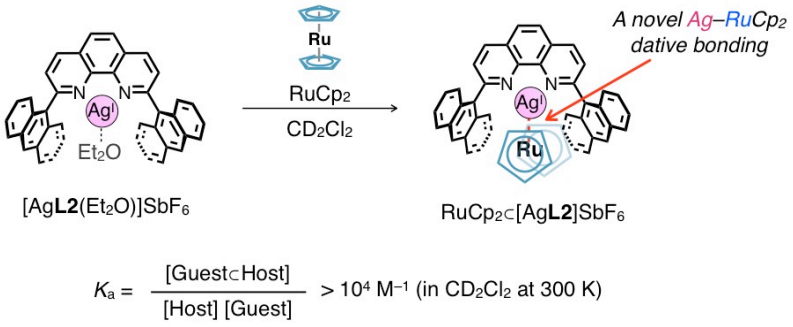

Figure 4–2. Host-guest complexation between a mononuclear Ag(I)-half-macrocycle $[Ag\mathbf{L2}(Et_2O)]SbF_6$ and ruthenocene via metal-to-metal dative bonding.

As described above, nano-spaces, in which coordinatively labile sites of *non*-Werner type coordination centers are arranged in a well-defined manner, possibly provide novel binding motifs for host-guest complexation utilizing metal–arene interactions and metal–metal interactions as driving forces. Such host-guest systems show promise in developing metal-based functions such as separation, accumulation, and activation of *pristine* aromatic molecules or organometallic molecules taking advantage of specific coordination properties of well-arranged *non*-Werner type coordination centers.

For instance, in the cases of the dinuclear Ag(I)-macrocycle described on Chapter 2, the mode of arrangement of Ag(I) ions and the structures of aromatic guest molecules strongly affect host-guest affinity. Therefore, we can develop these host-guest systems for size- and shape-selective recognition and separation of pristine aromatic hydrocarbons (Figure 4–3a). Besides, direct and multipoint bonding interactions with Ag(I) ions in the nano-spaces possibly

modify chemical/physical properties to included guest molecules based on integrated electron withdrawing effects of multi Ag(I) ions. This effect would be available for the activation of pristine aromatic molecules. Moreover, macrocycles with multi metal centers have potentials to accomodate multi guest molecules within their nano-space, which induce intermolecular interactions among included guest molecules to activate optical properties or multi molecular reaction specific to the nano-space (Figure 4–3b).

A metal–metal bonded complex of pristine ruthenocene described on Chapter 3 proposes a new method for supramolecular binding of metallocenes using non-covalent interactions at its metal centers. Such a structural motif would lead to further development of metallocene-based molecular architectures such as metallocene-based rotaxanes etc (Figure 4–3c).

Covalently-linked skeletons of the macrocycles are highly designable. Therefore, we can prepare nano-spaces with a variety of shape and arrangement modes of *non*-Werner type coordination centers (Figure 4–3d). By using such metallo-macrocycles as templates, we can prepare various kinds of *non*-Werner type complexes within their nano-spaces as guest-metal aggregates. For instance, template-directed preparation of hetero-metallic clusters based on metal-to-metal dative bonding (Figure 4–3e left) or discrete metal–arene aggregates with a specific number and configuration of metals is expected (Figure 4–3e right). As the nano-spaces of macrocycles are isolated from external environment and well-defined by their organic skeletons, complexes which cannot be prepared under ordinal conditions would be provided. Investigation of the resulting complex would give us valuable knowledge about *non*-Werner type complexes. Thus, this study will lead to development of host-guest chemistry and coordination chemistry.

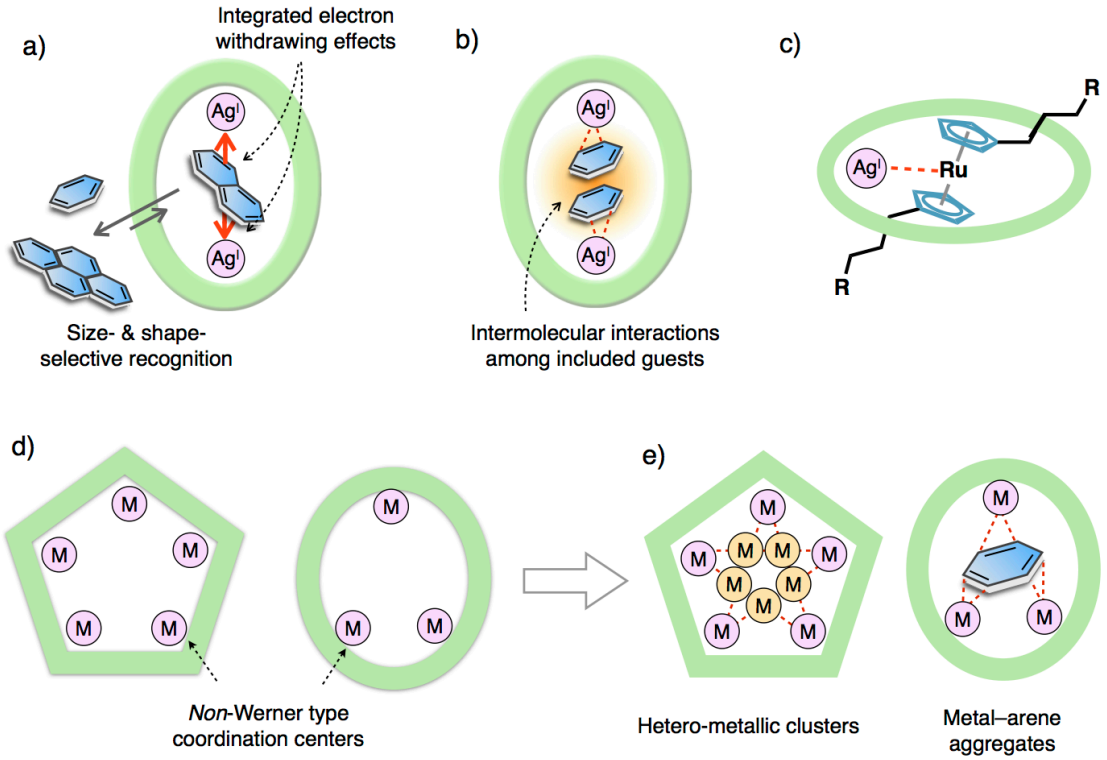

Figure 4–3. a) Size- and shape-selective recognition and isolation of pristine aromatic hydrocarbons and modification of their chemical/physical properties via multipoint Ag–π interactions, b) accumulation of multi guest molecules via Ag–π interactions and induction of specific intermolecular interactions among them. c) A metallocene-based rotaxane as an example of metallocene-based molecular architectures utilizing metal-to-metal dative bonding, and d) nano-spaces with a variety of shape and modes of arrangement of *non*-Werner type coordination centers, and e) template-directed syntheses of hetero-metallic clusters (left) and discrete metal–arene aggregates (right) within macrocycles.

A list of publications

[1] “Multipoint Recognition of Ditopic Aromatic Guest Molecules via Ag−π Interactions within a Dimetal Macrocycle” Kenichiro Omoto, Shohei Tashiro, Masumi Kuritani, and Mitsuhiko Shionoya, *J. Am. Chem. Soc.* **2014**, *136*, 17946–17949.

[2] “Host–Guest Interactions by Metal-to-Metal Dative Bonding: Recognition of Ruthenocene by a Metallo-Host” Kenichiro Omoto, Shohei Tashiro, and Mitsuhiko Shionoya, *Z. Anorg. Allg. Chem.* **2015**, *641*, 2056–2059.

Acknowledgement

This research was promoted under supervision of Professor Dr. Mitsuhiko Shionoya (The University of Tokyo). He has always given me generous guidance, reassuring encouragement, and innovative ideas. I cannot express my appreciation enough for his fruitful discussion and extraordinary care for my life as a researcher for six years. I would like to take this opportunity to express my utmost gratitude to him.

I deeply appreciate Associate Professor Dr. Shohei Tashiro (The University of Tokyo) for his kind teaching and critical suggestion about my research. His innovative, creative, and progressive ideas have always expanded my view of science.

I appreciate Assistant Professor Dr. Hitoshi Ube (The University of Tokyo) for his fruitful discussion and suggestion about chemistry.

I am thankful to Assistant Professor Dr. Yusuke Takezawa (The University of Tokyo) to give me useful suggestion about research and academic careers.

I appreciate Dr. Aiko Kamitsubo for elemental analyses for my compounds.

I gratefully acknowledge all the members of Shionoya laboratory to support every day of my research. In particular, I would like to express my appreciation to Dr. Masumi Kuritani for giving me fundamental of research skills, valuable advice, and knowledge about the chemistry of macrocycles. Also, I am grateful for Mr. Tatsuya Kamatsuka and Mr. Shun Shimizu, who enthusiastically study the related macrocycles.

I am thankful to Advanced Leading Graduate Course for Photon Science (ALPS) program for the financial support and giving me an opportunity to study abroad. I am also grateful for Professor Dr. Shin-ichi Ohokoshi (The University of Tokyo) to give me chance to discuss about my research as a vice supervisor. I would like to appreciate Professor Dr. F. Ekkehardt Hahn (Westfälische Wilhelms-Universität) for giving me a valuable experience to study in Germany for two and a half months.

Finally, I would like to express my sincerely appreciation to my family for giving me encouragement and support for a long time.